Measurement of invisible products from Muon Decay
Particle physics laboratory report

ELEONORA DIOCIAIUTI
CRISTINA MARTELLINI
GIULIO SETTANTA
VALENTINA VECCHIO

Universitá degli Studi Roma Tre
Febraury 8, 2016

Abstract

Muons compose the penetrating component of Cosmic Rays. At sea level, they constitute the largest part of Secondary Cosmic Rays, giving an average flux of $\approx 100\ m^{-2}s^{-1}sr^{-1}$. The aim of our experiment is to estimate, from muon decay, the mean lifetime and the mass of invisible products. Our experimental setup includes four detectors: three of them are plastic scintillators and compose the trigger system, while the last one is a liquid scintillator which measures the particles energy. All these scintillators are read by photomultipliers. Trigger and pulse thresholds are computed by logical and temporal modules in a VME crate. The Data Acquisition System has been verified to work properly. It is composed of two fADCs modules, one I/O Register, one Motorola computer and a Farm. The liquid scintillator has been calibrated in energy using both passing muons and ^{60}CO gamma source. Thanks to the charge-energy conversion factor we estimated electron energy spectrum. In particular we selected a sample of decay events by estimating muon mean lifetime $\tau_\mu = 2.19 \pm 0.34\ \mu s$; then we finally extrapolated an upper limit for invisible products mass $m_\nu < 5.99 \pm 0.73\ MeV/c^2$.

Contents

Introduction

The aim of our experiment is to estimate the invisible products mass from muon decay. The particles we used come from Cosmic Rays, briefly described in Section 1.1. Muon mean lifetime can be inferred from the decay distribution whilst neutrino mass from the endpoint of Michel Spectrum; a theoretical description of these quantities is shown in Section 1.2.1.
The experimental set up is made of four organic detectors: three of them are plastic scintillators and the fourth is a liquid one. Physics of scintillators is described in Section 2. All our scintillators are read by photomultipliers, a description of operations and characteristics is made in Section 3. Plastic scintillators are part of the trigger system whilst liquid scintillator, contained inside a tank 33 cm tall tank, is used to measure the energy released by particles. All the details concerning the trigger set up and working points of the plastic and liquid scintillators are reported in Sections 4 and 6.
The DAQ System, described in Section 5, consists of a farm plus four boards: a Motorola computer, an I/O Register and two fADCs. Except for the Farm, all modules are located inside a VME Crate. Motorola and Farm are connected by an Ethernet cable. Voltage signals are sent as input for the fADC, which digitizes it at a 250 MHz. The Motorola can manage the entire acquisition, by means of the Start and the Reset command via the I/O register. It controls also the temporary storage of data in in the fADC buffer and commands any data movement to the Farm. Thanks to the send, the receive and write code, data are storage in the Farm where we decode run files using a dedicated class. This same class has a special routine for Event Displaying.
Process followed in order to find the conversion factor using the ^{60}Co source is explained in Section 7.1. In the distribution of charge collected by the photomultiplier we find a γ emission region that we fitted with a gaussian. We compare the mean value of the gaussian distribution with the mean value of the two γ emission peak in order to define the conversion factor $C_{^{60}Co}$.
In Section 7.2 we reported how to estimate the conversion factor from Q to E, using passing muons through the energy released inside LS by them. We therefore found the collected charge inside the liquid scintillator and thanks to the evaluation of the muon's energy at the minimum of ionisation so to compare the two different values, we could evaluate the final C_μ factor with the relative uncertainty.
Muon mean lifetime measurement (Section 7.3) has been performed through the reconstruction of exponential decay distribution, from a sample of data acquired in TRG decay mode. We extrapolated the value from a fitting function that take in account both exponential decay shape and uniform distribution of background events. From lifetime value we made a first order estimate of Fermi Coupling Constant G_F.
An analysis of the electron spectrum from muon decays (Section 7.4) can be performed in order to estimate the mass of the invisible products. The spectrum is built in terms of the charge collected by the PMT for each event. A comparation between the Michel spectrum and the experimental endpoint obtained in this work is used to evaluate the neutrino mass, after converting the total charge into the electron energy.

1 Starting from the Theory

1.1 Cosmic Rays (Giulio)

The term *Cosmic Rays* refers to high-energy radiation coming from outside the earth. They are composed by charged nuclei: 90% of this flux consists of protons, 9% of alpha particles and the rest are heavier nuclei, mainly Iron. When these particles hit our atmosphere molecules, they can produce secondary interactions, that we see as a *cascade*. The study of Cosmic Rays gave us a lot of information about the environments where most energetic phenomena in our universe occur, about their composition and their acceleration mechanisms. Although since their discovery more than hundred years have passed, many questions still remain unsolved, about the issues described above. The scientific community still doesn't find a unique interpretation about the origin, the propagation and the spectrum of Cosmic Rays.
The first hints of the presence of a "cosmic" radiation come from Theodor Wulf, a German physicist and a jesuit priest, in 1910. With the auxilium of a self-built electrometer he compared the radiation measured at the bottom and at the top of the Eiffel Tower. The result was a decreasing ionization with increasing height, as expected, because of the natural radioactivity of the ground. But the degree of decrease was lower than the predicted value: there was an excess of ionization [1]. Nevertheless, his paper was not initially accepted. In the same period, underwater measurements by Domenico Pacini [2] showed the evidence that "in the hypothesis that the origin of penetrating radiations is in the soil [. . .] it is not possible to explain the results obtained". The final results came between 1912 and 1914 by Victor Hess [3] and Werner Kolhörster that revealed a significant increasing of radiation with an increasing altitude, by means of Wulf-electrometers on free balloon flights. The effect was measured by Hess up to a 5300m altitude (figure 1) and set the discovery of "a radiation of very great penetrating power that enters our atmosphere from above". For the discovery of cosmic radiation Hess was awarded with the Nobel Prize in 1936.
After the discovery in 1912, many efforts were devoted to cosmic rays investigation. First measurements were achieved using baloons or rockets, launched outside the earth's atmosphere. These experiments belong to the *direct measurements* class, because they are able to detect directly the cosmic ray flux. The opposite class is called *indirect measurements* and is composed by large ground-based detectors.
On the other side, cosmic radiation has been a very useful tool for the early Particle Physics, as a continuous source, before the construction of the first particle accelerators. For instance, it allowed the discovery of the positron, the muon and the π meson.

1.1.1 Primary spectrum

Cosmic Rays are believed to be generated in violent astrophysical environments, such as collapsing supernovae or Active Galactic Nuclei. They exhibit a very wide energy spectrum, running from 10^9 up to 10^{20} eV. This large range can't be interpreted in terms of a single acceleration mechanism, nor of a unique class of sources. At zero order, it consists

[1] T. Wulf. - *About the radiation of high penetration capacity contained in the atmosphere*, Physikalische Zeitschrift, 1910.
[2] D. Pacini. - *La radiazione penetrante alla superficie ed in seno alle acque.*, Il Nuovo Cimento, 1912.
[3] V. Hess. - *Nobel Prize in Physics*, 1936.

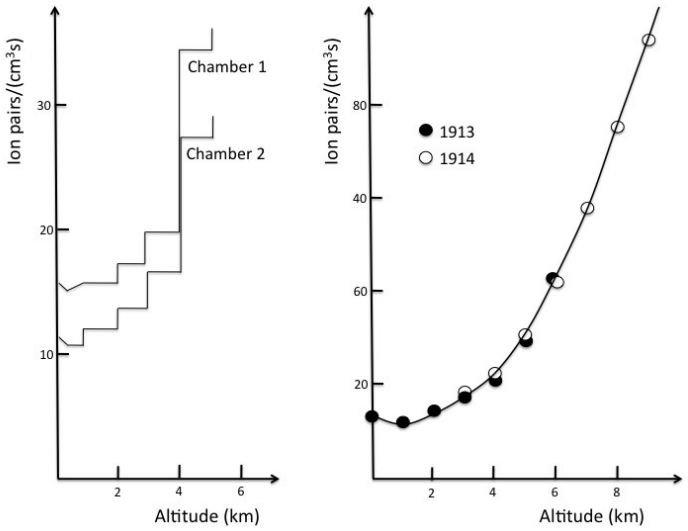

Figure 1: *Increase of ionization with altitude as measured by Hess (left) and Kolhörster (right).*

of a power-law spectrum $\propto E^{-\gamma}$, with two changing points in the slope (figure 2) [4].
The power-law spectrum reflects non-thermal processes at the origin. This means that cosmic particles are accelerated in high energy environments through relativistic mechanisms.
The spectral index is ≈ 2.7 until $\sim 10^{15}\ eV$, then it becomes larger (≈ 3). This first change is commonly called "knee" because of the steepening of the spectrum. It is presumably due to breakdown processes in the acceleration mechanisms at the production site. At $\sim 10^{18}\ eV$ there is a second change in the spectrum, for it becomes harder ($\gamma \approx 2.6$). It is called "ankle" and corresponds to the energy at which presumably the extragalactic component becomes dominant.
At higher energies a strong decrease of events is expected because of the GZK cutoff: $\sim 10^{20}\ eV$ is the energy threshold for the processes

$$p + \gamma_{cmb} \rightarrow e^+ e^- p$$

$$p + \gamma_{cmb} \rightarrow \pi^+ \pi^- p$$

assuming photons in the microwave spectrum. Then, protons over $\sim 10^{20}\ eV$ can interact with the Cosmic Microwave Background, losing a fraction of their energy. The GZK cutoff is actually confirmed by the Auger[5] and the Telescope Array experiments[6].
In 1947 E. Fermi developed the most famous acceleration model, in order to explain the relativistic spectrum observed. In his theory, cosmic rays reach their energy through many acceleration stages, interacting with shock waves. Such waves can be produced by supernovae explosions, that accelerate particles of the surrounding medium.
From the spectrum, one can see that the flux decreases rapidly with increasing energy. At 10 GeV is about 1 particle per $m^2\ s$, while at the knee energy is ~ 1 particle per ($m^2\ y$) and

[4] PDG 2014
[5] https://www.auger.org/
[6] http://www.telescopearray.org/

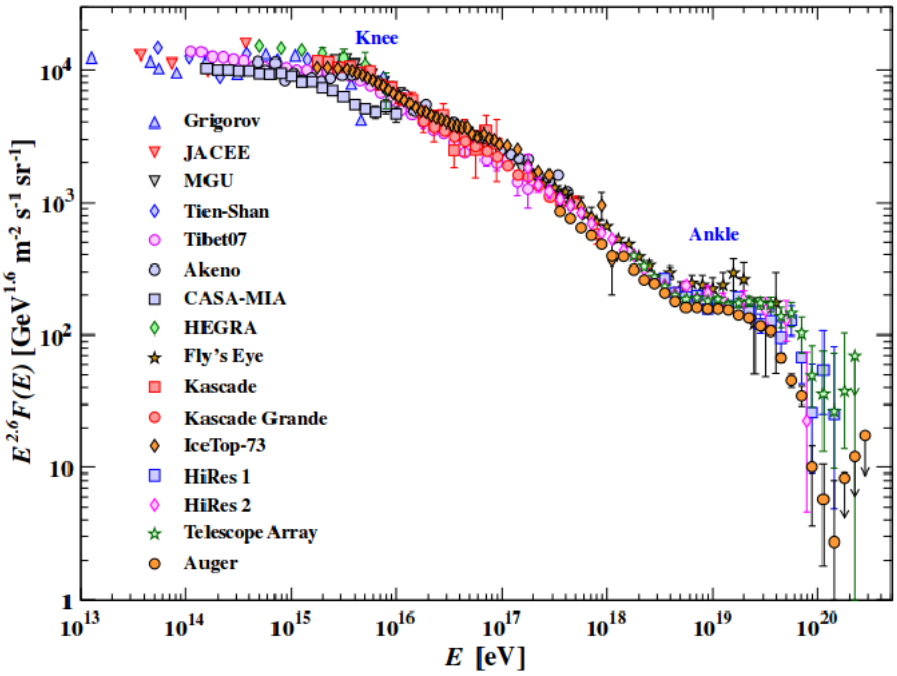

Figure 2: *Differential cosmic ray energy spectrum, as measured by various experiments.*

around the GZK cutoff is of the order 1 particle per (km^2 *century*). This implies that direct measurements outside the atmosphere are available only at low energies, because it's hard and really expensive to build satellites or balloons with large surface and they are also limited by their flight time. Recent experiments set the maximum energy for the primary flux measurement at $E \approx 100$ *TeV*. In order to investigate the higher-energy part of the spectrum, one needs large ground-based arrays (EAS - Extensive Air Shower arrays), that can detect the *secondary component* of the spectrum.

1.1.2 Air Showers

A high energy cosmic ray produces a cascade of particles when it enters inside the earth's atmosphere. The first interaction tipically happens with a nitrogen or an oxygen atom, and generates secondary particles, such as protons, neutrons and pions. These secondary particles then can interact with another atom, decay or be absorbed. The sum of all particles produced by a single cosmic ray is called an *air shower* (figure 3).

From the first interaction, different particles can be produced. Because of the different nature of secondary particles, an air shower exhibits three different components, electromagnetic, hadronic and muonic (neglecting neutrinos). It consists then of a heterogeneous thin disk of relativistic particles. Hadrons tipically compose the core, while feeding the electromagnetic part by decay of neutral pions and kaons. Lower energy charged pions and kaons decay to increase the muonic component. A fraction of the electrons comes also from muon decays.

To describe the developement of an air shower inside the atmosphere, a simple and in-

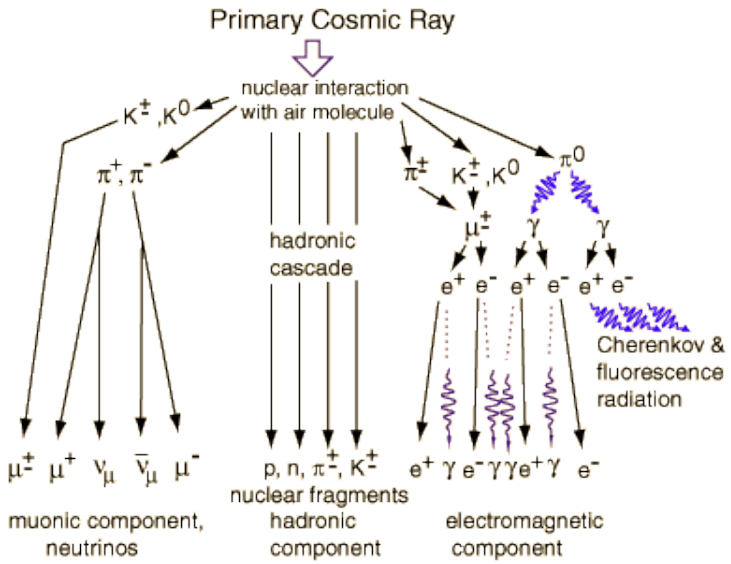

Figure 3: *Schematization of an air shower: the interaction of a cosmic ray in the atmosphere generates a cascade of secondary particles; a shower can be divided in the leptonic, the hadronic and the electromagnetic component.*

tuitive toy model can be used[7]: after a collision lenght λ a particle in the shower decays or interacts, producing two new particles, and at every branching the energy is splitted in two. The duplication process continues until the energy per particle goes under a critical energy E_c, then the shower starts to be absorbed by the atmosphere. The number of particles at the maximum is given by

$$N_{max} = E_0 / E_c$$

In conclusion, an air shower grows in its propagation inside the atmosphere until a maximum depth, then it is absorbed. This puts a lower limit in the energy spectrum for the air shower arrays, because low-energy showers stop before they reach the ground.

1.1.3 Penetrating component

During the shower development, as explained above, the total number of particles reaches a maximum and then starts to decrease, due to the atmosphere absorption. The probability of a single particle to be absorbed is not equal for all secondaries: depending of their nature, particles can penetrate different thicknesses before they stop, as shown in figure 4[8]:
The flux of electrons and pions rapidly decreases with depth, because they easily decay or interact. Beside them, from figure 4 one can see that there is a class of particles whose flux is just weakly dependent of the depth, the muons: they were discovered as a *penetrating component* in the cosmic ray flux. Muons are produced at tipical energies close

[7] W. Heitler. - *The Quantum Theory of Radiation*, Clarendon Press, 1944.
[8] PDG 2014

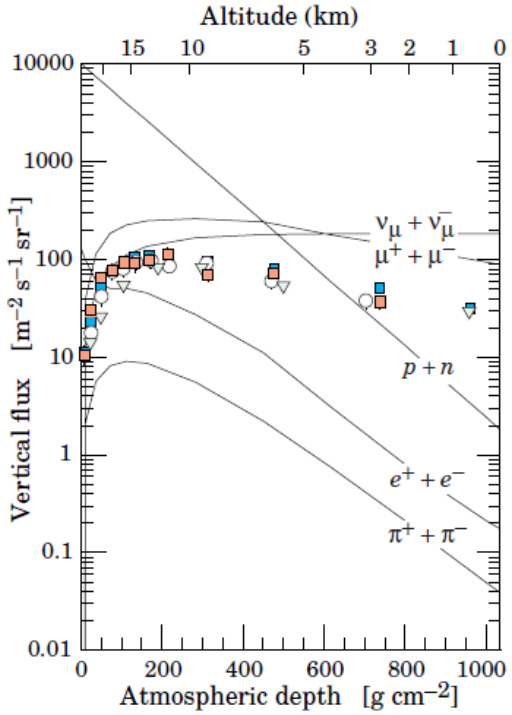

Figure 4: *Vertical flux of secondary cosmic rays, separated by particle. Points refer to negative muons with* $E_\mu > 1\ GeV$.

to the Minimum Ionization Point, so they lose their energy slowly. This is why the largest part of them reach the ground.
An analitic solution for the muon spectrum can be inferred in an intermediate energy regime, with some assumptions: first, muons are produced in the decays

$$K^\pm \rightarrow \mu^\pm \overset{(-)}{\nu_\mu}$$

$$\pi^\pm \rightarrow \mu^\pm \overset{(-)}{\nu_\mu}$$

then, one inserts the phase space factor for muons. The expression must be merged with the mesons spectrum (because of the first assumption). Last, considering muons with an energy $E_\mu \gtrsim 1\ TeV$, one obtains [9]:

$$\frac{dN_\mu}{dE_\mu\, d\Omega} \approx 0.14\, E^{-2.7} \times \left(\frac{1}{1 + \frac{1.1 \cdot E_\mu cos\theta}{115 GeV}} + \frac{0.054}{1 + \frac{1.1 \cdot E_\mu cos\theta}{850 GeV}} \right) cm^{-2} s^{-1} sr^{-1} GeV^{-1} \qquad (1)$$

where the first term in brackets refers to the pion contribution and the second term to the kaon contribution. From (1) one can see that, in the energy range mentioned above, the muon spectrum follows approximately the same power-law of primary cosmic rays.
The total flux of muons at sea level is about 100 $m^{-2}\ s^{-1}\ sr^{-1}$, integrating over all the energy spectrum.

[9] PDG 2014

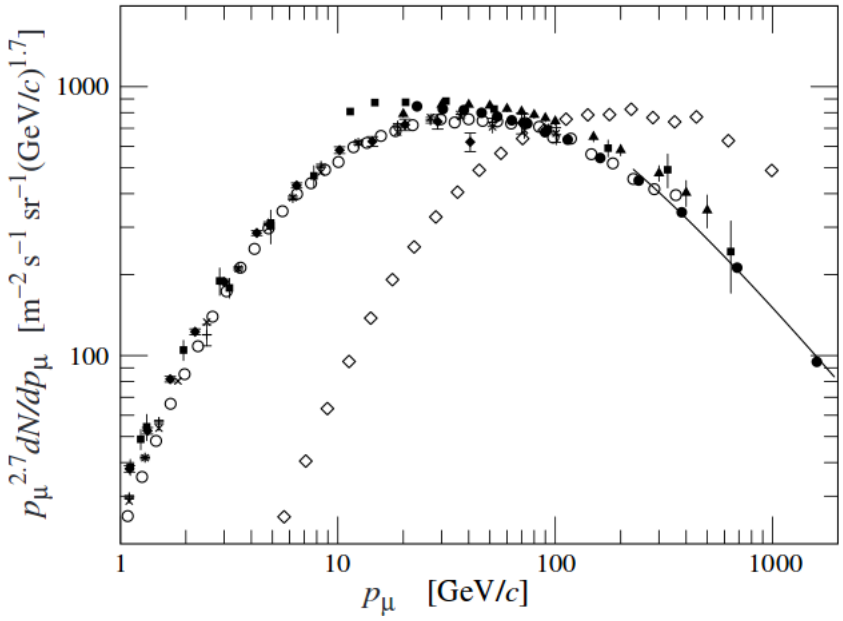

Figure 5: *Muon spectrum at zenith angle $\theta = 0$, with different experiments results; open diamonds refers to $\theta = 75°$; black line plots equation* (1).

1.1.4 Detection techniques

During the last century, since their discovery, cosmic rays have aways carried many questions with them. The continuous search for answers made technologies to improve in this sector, starting from the first measurements on balloons. Because of the spectrum shape, different techniques are necessary to investigate the cosmic radiation. For energies up to the multi-TeV the most convenient tool consists of satellites or balloons, like the one shown in figure 6, left [10]. Higher energy range can be explored by EAS arrays on a large surface (figure 6, right [11]. Particle detection relies on classical particle physics tools, such as trackers, gas detectors and calorimeters.

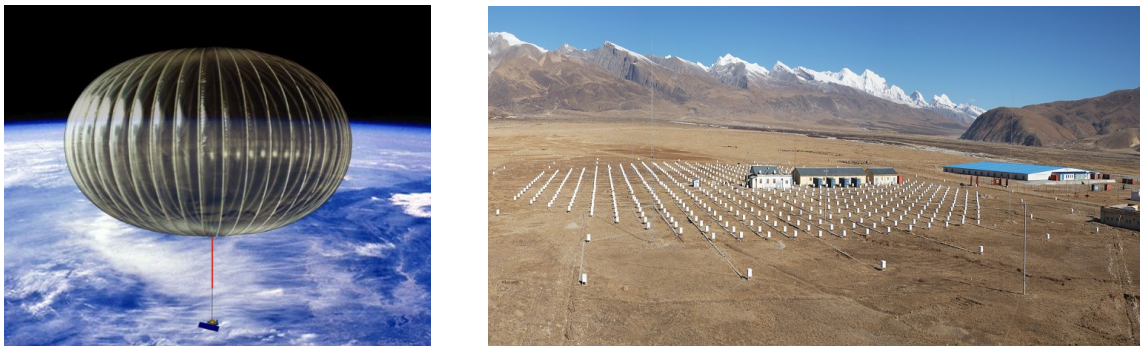

Figure 6: *Left: tipical balloon-borne experiment; right: tipical EAS experiment.*

[10] http://cosmicray.umd.edu/cream/
[11] http://www.icrr.u-tokyo.ac.jp/em/

1.2 Muon (Valentina)

The *muon* is an elementary particle, classified in the *Standard Model* as *lepton*.
Muon has been discovered by Stevenson and Street in 1936. They found that this sharply component of cosmic radiation is a fermion (spin $1/2$), with unitary charge, lifetime $\tau_\mu \approx 2.2\ \mu s$ and mass measured to be $\approx 106\ MeV/c^2$.
As predicted by Dirac theory of fermions, muon has an anti-particle of opposite charge but equal mass and spin: the *anti-muon* (μ^+).

1.2.1 Muon Decay

Muons are unstable particles which decays in function of time are represented by the following exponential law[12]:

$$N(t) = N(0)e^{-t/\tau_\mu} \tag{2}$$

It's easy to derive this expression if two hypothesis are made:

1. The probability of decay in function of time it's an intrinsic property of particle and does not depends on time;
2. The probability of decay in function of time does not depends on the number of initial particles.

It follows that the probability variation verifies $dP = \lambda dt$, where λ is the *decay constant* $[s^-1]$. If we have N particles the variation of this quantity in function of time is $-dN = \lambda N dt$. Solving this differential equation and fixing $\lambda = \frac{1}{\tau}$ we can obtain the exponential law above.
From Fermi's golden rule it's possible to calculate the decay width $\Gamma = \hbar/\tau$ where

$$\frac{1}{\tau} = \frac{2\pi}{\hbar} |\langle f| H_I |i\rangle|^2 \rho(E_f) \tag{3}$$

This quantity depends on the matrix element of the transition $|i\rangle \to |f\rangle$ and the phase space.
In vacuum muons decay in one electron and two neutrinos, as shown in Figure 7

$$\mu^- \to e^- \overline{\nu}_e \nu_\mu$$
$$\mu^+ \to e^+ \nu_e \overline{\nu}_\mu$$

with same decay fraction $\Gamma_i/\Gamma \approx 1$ and lifetime. This process is well described by a V-A interaction.
However, in matter, negative muons, when brought to rest in the close neighborhood of some nucleus (Z,A), can also disappear through the competing reaction

$$\mu^- + N_1(Z, A) \to N_2(Z - 1, A) + \nu_\mu$$

The rate of the muon-capture process depends strongly on the charge Z of the nucleus which captures the muon (probability $\propto Z^4$). For nucleus with $Z < 10$ this phenomena can be neglected.

[12]Prof. Filippo Ceradini, Appunti del corso di Istituzioni di Fisica Nucleare e Subnucleare, 2003

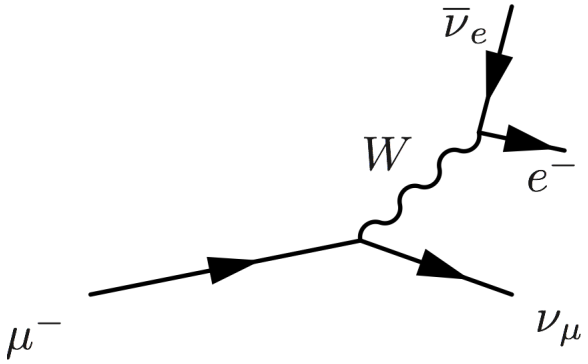

Figure 7: Feynman Diagram's muon decay

Let's focuse on the free decay: it is a three-body decay (Figure 8) where the maximum of $|p_3|$ is achieved when $m_{12} = p_1 + p_2 = m_1 + m_2$. If, in addition, $m_3 > m_1, m_2$ (in muon case it's true if $m_3 = m_e$) then $|p_3|_{max} > |p_1|_{max}, |p_2|_{max}$. The distribution of the m_{12} values possesses an end-point of maximum value at $m_{12} = M - m_3$.
This can be used to constrain the mass of muon invisible decay products, neutrinos.
In 1949, Louis Michel experimentally determined the energy spectrum of electrons coming

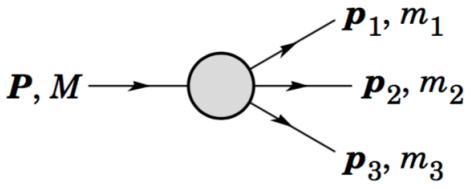

Figure 8: Definitions of variables for the three-body decays

from muon decay. As can be seen from the Michel spectrum on Figure 9, there is a half-bell distribution for the energies of electrons seen coming from muon decays, with a sharp cut-off at approximately 53 MeV.
The electron energy spectrum in muon decay offers an opportunity to test the V - A structure of the charged weak current. The electron energy spectrum in the decay of polarized muon is given by

$$\frac{d\Gamma}{dxdcos\theta_e} = \frac{G_F^2 m}{4\pi^3} E_{max}^5 \beta_e x^2 (F(x) - P_\mu cos\theta_e G(x)) \tag{4}$$

$$F(x) = x(1-x) + \frac{2}{9}\rho(4x^2 - 3x - x_0^2) + \eta x_0(1-x) \tag{5}$$

$$G(x) = \frac{1}{3}\xi\sqrt{x^2 - x_0^2}\left[1 - x + \frac{2\delta}{3}(4x - 3 + \sqrt{1 - x_0^2} - 1)\right] \tag{6}$$

where $x = E_e/E_{max}$, $E_{max} = (m^2 + m_e^2)/2m$, $x_0 = 9,67\ 10^-3$, θ_e is the electron emission angle referred to muon polarisation vector P_μ and ρ, η, ξ and δ are Michel parameters. This description of the electron energy spectrum in muon decay in terms of Michel parameters

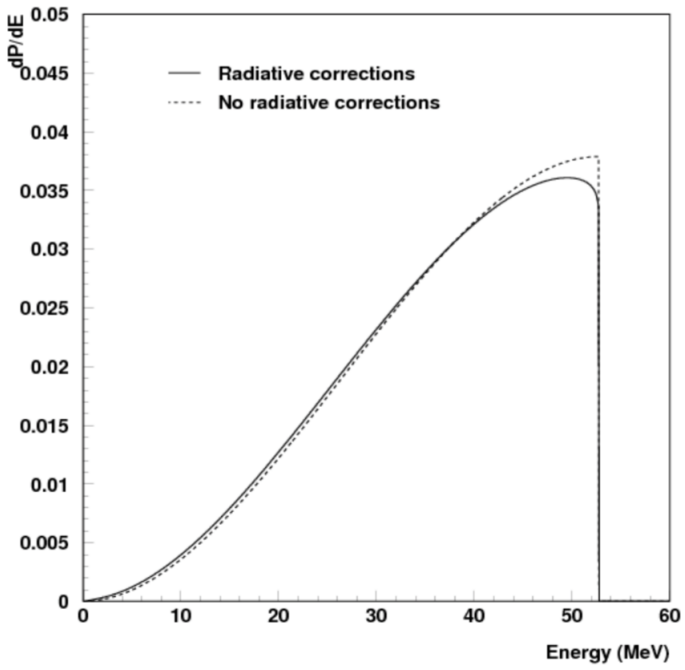

Figure 9: Michel electron energy spectrum

is, of course, oversimplified. QED radiative corrections change the functional form of $d\Gamma/dx$ and are object of more precise tests on *Standard Model*.

1.2.2 Why study muons?

Through the study of muon properties has been possible to master interesting physics arguments:

- The measurement of cosmic muon flux variation between two different altitudes [13] has been a test on **Special Relativity and its interpretation of time**.
  In fact, because muons from cosmic radiation can travel at $v \approx c$ they have a big γ factor. As result we observe a dilation of muon lifetime on earth that completely agrees with the relativistic expectation $t_{earth} = \gamma\tau_\mu$.

- As already mentioned in previous section, the decay of muon is mediated by the weak interaction exclusively. Thanks to the absence of strongly interacting particles, whose theoretical uncertainties on PDF and α_S are important systematics, this process is now the most accurate way of determining G_F, the **Fermi coupling constant**. This quantity is a input parameter for precision electroweak fits, so one can understands why muon lifetime it's an important measurement.
  We can easily calculate at first order from the Fermi's golden rule the relation between

[13] D.H. Frisch and J.H. Smith, ≪ Am. J. Phys≫, 31, 1963, p. 342

τ_μ and G_F

$$\frac{\hbar}{\tau_\mu} = \frac{G_F^2}{(\hbar c)^6}\frac{(m_\mu c^2)^5}{192\pi^3} \tag{7}$$

- From the study of the continuous energy spectrum of electrons from muon decay Pauli formulated a first hypothesis on the existence of **neutrinos**.

Farther muons will be used for future experiment that attempt to find indications of physics beyond the *Standard Model*

- Precision tests on *Standard Model* are based on the measurement of the **anomalous magnetic moment of the muon** [14] [15]. If we call g the factor predicted by Dirac to be 2, the anomaly a could give informations on new contribution not considered on our prediction, based on QED, weak and strong interaction.

$$a = \frac{g-2}{2} \tag{8}$$

- **Conservation of lepton numbers**. Present experimental evidence and the standard electroweak theory are consistent with the absolute conservation of three separate lepton numbers: L_e, L_μ and L_τ, except for the effect of the neutrino mixing associated with neutrino masses.
  If a violation of conservation of the lepton numbers exists for neutral leptons, it's reasonable to investigate on possible charged lepton violations with several searches. Two of the searches for violations involve muons:
  - the conversion of one charged-lepton type to another [16]

$$\mu \to e\gamma \tag{9}$$
$$\mu \to 3e \tag{10}$$

  - the conversion of one type of charged lepton into another type of charged anti-lepton.

$$\mu^- + N_1(Z, A) \to e^+ + N_2(Z-2, A) \tag{11}$$

[14] Muon g-2 Collaboration, ≪Phys.Rev.≫ D73:072003, 2006
[15] Muon g-2 Experiment at Fermilab (work in progress)
[16] Mu2e Experiment at Fermilab (work in progress)

2 Scintillating Detector

2.1 General Information (Eleonora)

Scintillation detector is one of the most common used devices in nuclear and particle physics.[17] It is based on the *scintillation* mechanism, that is when a particle passes through particular materials, kinetic energy is absorbed by the molecules and electrons are excited to the upper levels. Disexitations produce small flash light.
First use of scintillator detector date back to 1903 when Crookes invented the spinthariscope: a ZnS screen that produces scintillations when struck by a α particle.

Scintillation detectors consist of a scintillating material which generates photons in response to incident radiation, it is optically (directly or via a light guide) connected to a sensitive photomultiplier tube which converts the light to an electrical signal and electronics to process this signal. Scintillator elements are sketched in Figure 10.

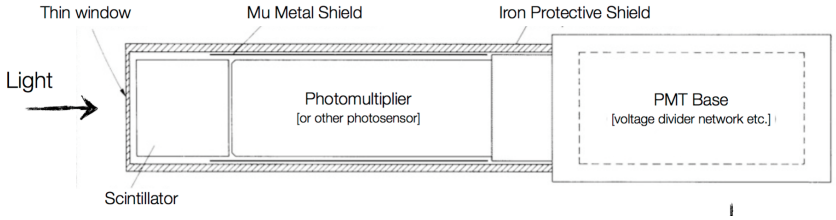

Figure 10: sketch of a scintillator

General characteristic of scintillator are:

- *high light yield*: number of photons produced per energy absorbed
- *linearity*: light output proportional to the absorbed energy
- *trasparency to the radiation emitted*: in order to collect the signal materials have to be transparent to the disexitation light
- emission spectrum has to be compatible with characteristic of available photomultipliers
- small decay constant (from a few ns to μs)

We can distinguish between two different typologies of luminescence: *fluorescence* deals with re-emission which occurs immediately after absorption (t=10^{-8}s) and *phosphorescence* concerns re-emission delayed because the excited state is metastable (μs<t<few minutes). Studying the time evolution of re-emission we can see that light output decreases exponentially:

$$\frac{dN(t)}{dt} = N_{tot}\left(\frac{A}{\tau_F}e^{-\frac{t}{\tau_f}} + \frac{B}{\tau_s}e^{-\frac{t}{\tau_S}}\right) \tag{12}$$

where A and B are factors that depends on material , τ_F and τ_S are the fast and slow decay constant; relative magnitude varies from materials to material but usually the fast components is dominant. In Figure 11 is represented the relation between the two components.

Scintillation detector provide different informations, we underline:

[17] W. Leo, Techniques for nuclear and particle Physics

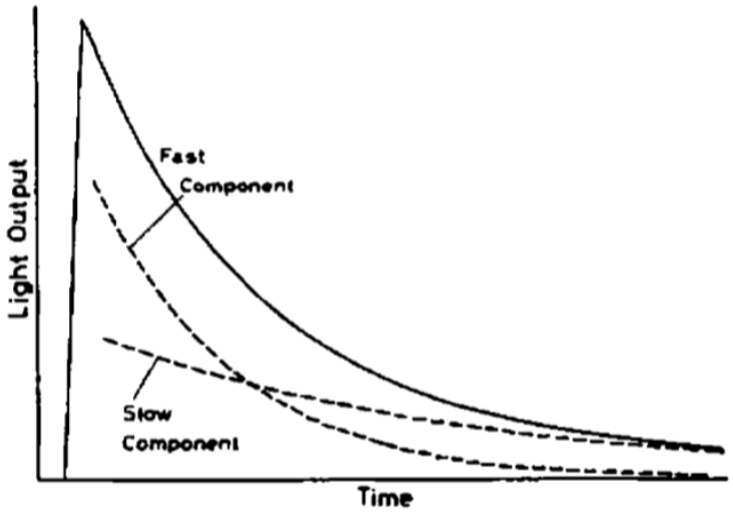

Figure 11: Fast and slow components of time evolution

- *Sensitivity to energy*: scintillator response to deposited energy results linear so that the light is direct proportional to the exiting energy; photomultipliers are linear devices too thus, since the amplitude of electrical signal results linear to this energy, scintillating devices can be used as energy spectrometer.
- *Fast time response*: scintillator response results fast with respect to other devices; it allows a collection of timing information(that is time difference between two events) with high precision.
- *Pulse shape discrimination*: it is possible to distinguish between different particles analyzing the shape of the emitted light pulse.

Different typologies of scintillating detectors are used: organic crystals, organic liquids, plastics, inorganic crystals,gases and glasses.

2.2 Scintillation mechanism (Cristina)

The organic scintillators are mainly aromatic hydrocarbon compounds containing linked or condesed benzene-ring structures. Their most distinguishng feature is a very rapid decay time on the order of a few nanoseconds or even less.
For what concern the scintillation light in these compounds, it arises from transitions made by *free valence electrons* of the molecules. These not localized electrons are not associated with any specific atom in the molecule and they occupy the π*-molecular orbitals*. We report in 12 a typical diagram for these orbitals, in which has been distiguished the spin singlet states from the spin triplet states. The ground state is a singlet state indicated with S_0. Above this level are the excited singlet states(S^*,S^{**}...) and, of course, the lowest triplet state (T_0) and its excited levels (T^*,T^{**}...). On top of that associated with each electron level is a fine structure which corrisponds to excited vibrational modes.

The energy spacing between vibrational levels is of order of a few tenths of eV. And the ionization energy from penetrating radiation excites both the electron and the vibrational levels. The singlet excitations it usually decays immediately ,in less than 10 ps,to the

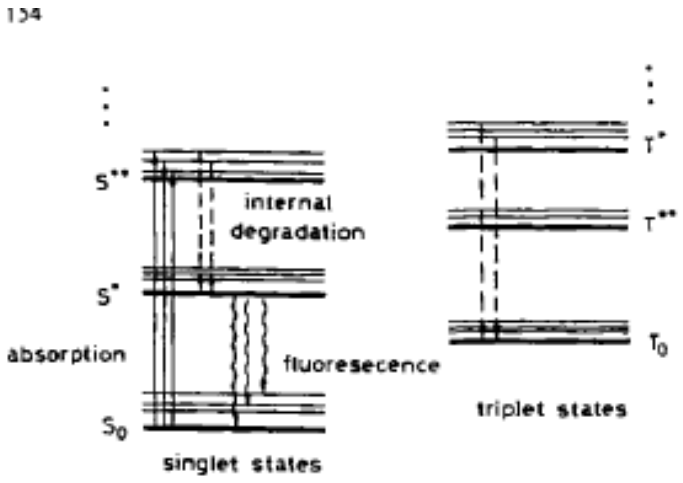

Figure 12: A scintillator viewed by multiple PM's for better light collection efficiency

S^* state without the emission of radiation,the one called *internal degradation*. From S^*, there's a high probability of making a radiative decay to one of the vibrational states of the ground state S^0 wthin a few nanoseconds. This is exactly the fluorescence process, described through an exponential law. At the same time the trasparency of the scintillators to their own radiation can be explained by the fact that S^* decays to excited vibrational states of S_0, and the emission of radiation is less than the one necessary for the $S_0 \rightarrow S^*$. On the other side, the triplet excited states get to the lowest triplet state through a degradation process. The transition process $T_0 \rightarrow S_0$ is forbidden by a multipole selection rules, but the T_0 state can definitely decay by interacting with another excited T_0 molecule:

$$T_0 + T_0 \longrightarrow S^* + S_0 + phonons \tag{13}$$

to leave one of the molecules in the S^* state. The light emitted comes after a delay time characteristic of the interaction between the excited molecule and it is the *delayed* or *slow* component of scintillator light; but this slow component to the total light output is only significant in some specific organic materials. Organics can also be used in many physical forms without loosing their scintillating properties due to the molecular nature of luminescence in these materials. As detectors, they find their use as pure crystals and as a mixtures of one or more compounds in liquid and solid solutions.

2.3 Liquid Scintillator (Eleonora)

2.3.1 General Characteristic

Liquid scintillator is typically made up of four components: a scintillating material that produces light in the UV when ionizing particles traverse it, a waveshifters that downshifts the UV photons to longer wavelength to facilitate absorption by the wavelength shifting (WLS) fibers, and a solvent which blends the components into a stable solution. Light production mechanism is shown in Figure 13.

Even if the scintillation process is equal to the one of the plastic scintillators the energy absorption is different: ionization energy is is mainly absorbed by the solvent and then

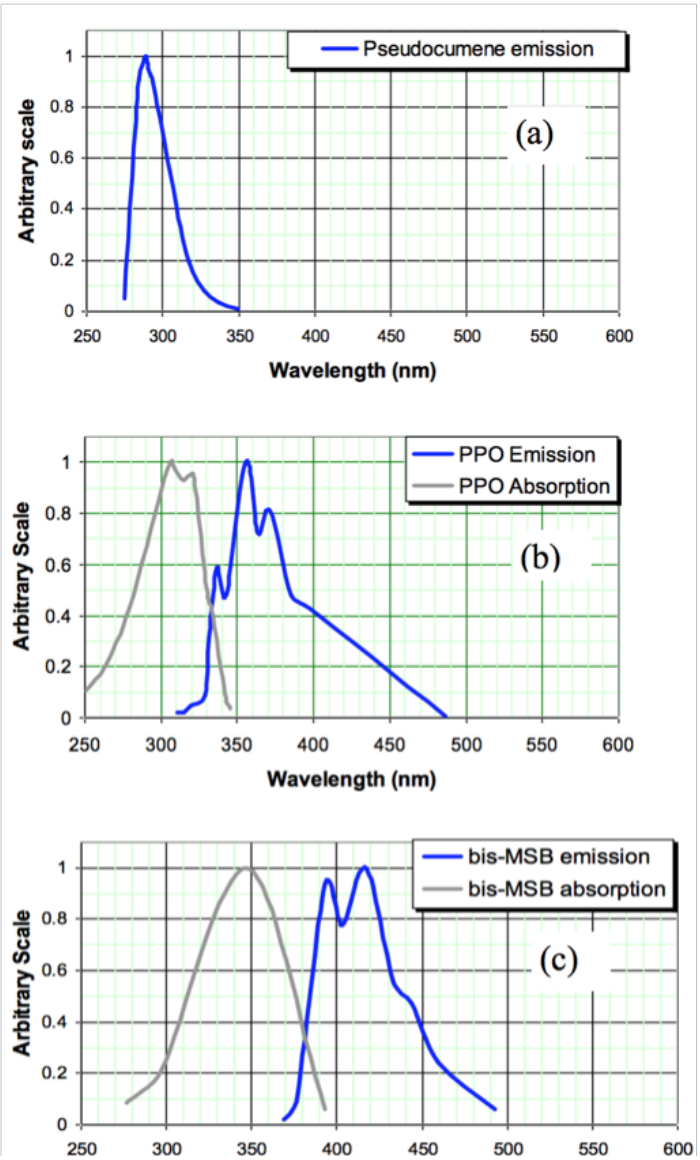

Figure 13: Spectrum of the primary scintillant psueudocumene traversed by an ionizing particle(a); the absorption and emission spectrum of the first waveshifter(b); the absorption and emission spectrum of the second waveshifter(c)

passed on the scintillation solute.
Most common solute are p-Therphenyl ($C_{18}H_{14}$), PBD ($C_{20}H_{14}N_2O$), PPO($C_{15}H_{11}NO$) and POPOP ($C_{24}H_{16}N_2O_2$); concerning solvent the most used are xylene, toluene, benzene, phenylcyclohexane, triethylbenzene and decaline.
Typical concentrations are on the order of 3 g of solute per liter. For liquid scintillators efficiency increase with the solute concentration and a wide maximum is reached just before the saturation of the solution.
Time response is quite fast, typically between 3-4 ns. They can be easily loaded with other materials in order to increase efficiency for particular aim: introducing Boron 11 can help

to neutron detection, or it is possible to add a wavelenghtshifter, which absorb light on a certain frequency and re-emit it in another frequency in order to make the spectrum more compatible with the PMT cathode.
Liquid scintillators are extremely sensitive to impurities in the solvent, it is easy to find that two samples of the same liquid scintillator have pulse height which can differ by a factor two.

2.3.2 Where are liquid scintillator used?

[18] Liquid scintillator are primarily used in neutrino experiment, in particular:

- Past and current large underground detector based on hydrocarbon scintillator(LVD, MACRO, Baksan, Borexino, KamLAND, SNO+)
- Experiment at nuclear reactors(CHOOZ, Double CHOOZ, Daya Bay, RENO)

Liquid scintillator are primarily used for detection of low-energies events.
They are chosen in these large experiment for the high light yield and attenuation,good stability, compatibility with other detector materials, high flash point, low toxicity, appropriate density for mechanical stability and low costs.
Typical energy resolution is about $7\%\sqrt{E(MeV)}$ and position reconstruction resolution at 1 MeV is about 10 cm.
They have an advantage over the Cherenkov detector because of the lack of Cherenkov threshold and the high light light yield, however scintillating light emission is isotropic; directional capabilities of liquid scintillators results weak.

2.3.3 EJ 321 H

EJ 321 H is a liquid scintillator made of aromatic hydrocarbon and organic flavor produced by Eljen Technologies; it appears as a clear, blue fluorescent liquid with aromatic odor.
It is primarily used for fast neutrons and photons, cosmic rays; it is characterized by a high light output. Because of flash point value EJ 321 H liquid scintillator are relatively safe when they are used in large volume experiments. The normalized output spectrum is shown in Figure 28. Scintillation properties and atomic composition are reported in Table 1.

2.4 Organic Crystals (Cristina)

The most common crystals are anthracene ($C_{14}H_{10}$), trans-stilbene ($C_{14}H_{12}$) and naphthalene ($C_{10}H_8$). All these crystals have a very fast time response on the order of a few nanoseconds, except for the anthracene which has a decay time of 30 ns, but at the same time their amplitude response is anisotropic, because of the channeling effects.
They are hard crystals and thus very durable, although stilbene tends too be fragile and more sensitive to thermal shock than anthracene, which makes the cutting of them to wanted forms and shapes is more complex. That's why these two fall in disuse.
Anthracene has instead the highest light output of all organic scintillators, and for other scintillators it is chosen as a reference so that the outputs are expressed as percent of anth

[18] PDG 2014

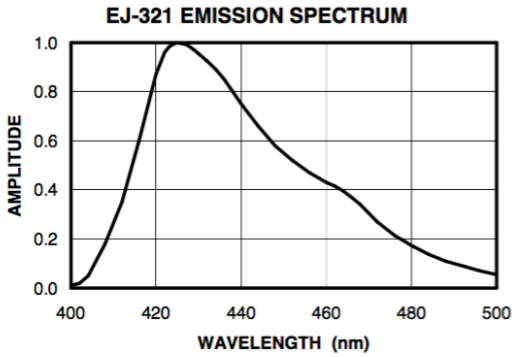

Figure 14: normalized output spectrum of a EJ 321 H

Light Output, % of Anthracene	
Saturated with Nitrogen	52 %
Saturated with Air	40 %
Mean Free Path (400-500 nm)	>5m
Specific Gravity	0.86
Wavelength of Maximum Emission	425 nm
H : C Atomic Ratio	1.89
Density	0.86
Decay Time, Short Component	2 ns
Refractive Index	1.48
Flash Point (T.O.C.)	81°
No. of H Atoms per cm^3 ($\times 10^{22}$)	7.03
No. of C Atoms per cm^3 ($\times 10^{22}$)	3.72
No. of Electrons per cm^3 ($\times 10^{22}$)	29.4

Table 1: EJ 321 H properties [a]

[a] from EJ 321 H data sheet, http://www.eljentechnology.com/index.php/products/liquid-scintillators/76-ej-321l

3 Photomultipliers (Cristina)

Photomultipliers (PM's) are electron tube devices witch convert light into a measurable electric current. They are extremely sensitive and, in nuclear and high-energy physics, are most oten associated with scintillation detectors,although their uses are quite varied.It is nevertheless in this context that we will discuss the basic design and properties of photomultipliers,their characteristics under operation and some special techniques.

3.1 Basic Construction and Operation

Figure shows a schematic diagram of a typical photomultiplier. It consists of a cathode made of photosensitive material followed by an electron collection system, an electron multiplier section (or dynode string as it is usually called) and finally an anode from which the final signal can be taken.[19] All parts are usually housed in an evacuated glass tube so that the whole photomultiplier has the appearance of an old-fashion electron tube. During operation a high voltage is applied to the cathode, dynodes and anode such that a potential "*ladder*" is set up along the length of the cathode-dynode-anode structure. When an incident photon (from a scintillator for example) impinges upon the photocathode, an electron is emitted via the photoelectric effect. Because of the applied voltage, the elctron is then directed and accelerated towards the first dynode,where upon striking, it transfers some of its energy to the electrons in the dynode. This causes secondary electrons to be emitted, which in turn,are accelerated towards the next dynode where more electrons are released and further accelerated. An electron cascade down the dynode string is thus created. At the anode,this cascade is collected to give a current which can be amplified

[19] An alternative structure rarely used with scintillation counters is the *side-on* PM.Here the photocathode is oriented so as to face the side of the tube rather than the end window.

and analyzed.

Photomultipliers may be operated in continuous mode,i.e., under a constant illumination, or in a pulsed mode as in the case in scintillation counting. In either mode, if the cathode and dynode systems are assumed to be linear, the current at the output of the PM will be directly proportional to the number of incindent photons. A radiation detector produced by coupling a scintillator to a PM (the scintillator produces photons in proportion to the energy deposited in the scintillator) would thus be capable of providing not only information on the particle's presence but also the energy it has left in the scintillator. Now we can have a closest look at the various parts of the photomultiplier in fig 15[20]

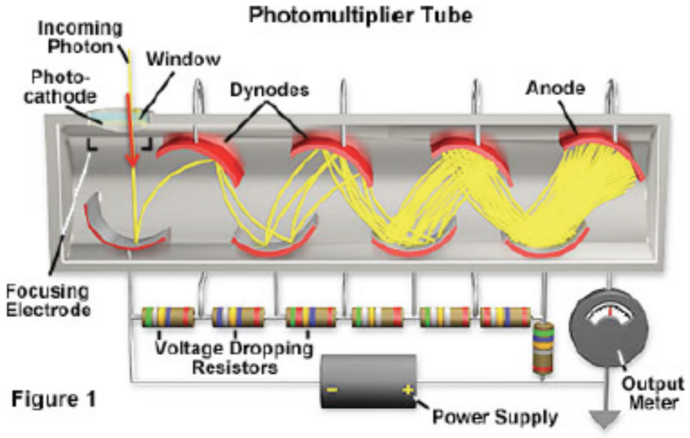

Figure 15: Diagram of a photomultiplier tube

3.2 The Photocathode

As we have seen,the photocathode converts incindent light into a current of electrons by the photoelectric effect. To facilitate the passage of this light,the photosensitive material is deposited in a thin layer on the inside of the PM window which is usually made of glass or quartz. From Einstein's well-known formula.

$$E = h\nu - \phi \tag{14}$$

where E is the kinetic energy of emitted electron, ν is frequency of incindent light and ϕ is the work function, it is clear that a certain minimum frequency is required before the photoelectric effect may take place. Above this threshold,however,the probability for this effect is far from being unity. Indeed, the efficiency for photoelectric conversion varies strongly with the frequency of the incident light and the structure of the material. This overall spectral response is expressed by the quantum efficiency, $\eta(\lambda)$,

$$\eta(\lambda) = \frac{number\ of\ photoelectrons\ released}{number\ of\ incident\ photons\ on\ cathode\ (\lambda)} \tag{15}$$

[20]http://www.roma3.infn.it/ petrucci/FabrizioPetrucci/LabFNS2014.html

where λ is the wavelength of the incident light. An equivalent quantity is the *radiant cathode sensitivity* which is defined as

$$E(\lambda) = \frac{I_k}{P(\lambda)}, \tag{16}$$

where I_k is the photoelectric emission current from the cathode and $P(\lambda)$ is the incident radiant power. The radiant cathode sensitivity is usually given in units of ampere/watts and is related to the quantum efficiency by

$$E(\lambda) = \lambda\eta(\lambda)\frac{e}{hc}. \tag{17}$$

For E in [A/W] and λ in nanometers

$$E(\lambda) = \frac{\lambda\eta(\lambda)}{1240}[A/W]. \tag{18}$$

A third unit is the *luminous cathode sensitivity* which is defined as the current per lumen of incident light flux. Since the lumen is essentially a physiological unit defined relative to the response of the human eye, the luminous sensitivity is not a unit to be recommended. The figure 16[21] below shows a graph of *quantum efficiency* vs λ for a few common materials used in photomultipliers.

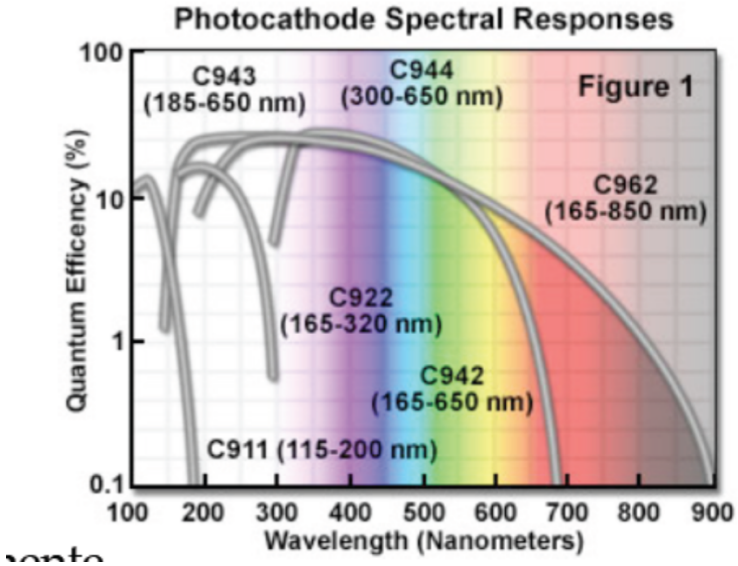

Figure 16: Quantum Efficiency

Most of the photocathodes employed today are made of semiconductor materials formed from antimony plus one or more alkali metals. The choice of semiconductors rather than metals or other photoelectric substances lies in their much greater quantum efficiency for converting a photon to a usable electron. Indeed, in most metals the quantum efficiency is not greater than 0.1% which means that an average of 1000 photons is needed to release one photoelectron. In contrast semiconductors have quantum efficiencies of the order of 10 to 30%, some two orders of magnitude higher. This difference is explained by

[21] http://www.roma3.infn.it/ petrucci/FabrizioPetrucci/LabFNS2014.html

their different intrinsic structures. Suppose, for example, an electron absorbs a photon at some depth x in the material. In traveling to the surface, this electron will suffer an energy loss, $\Delta(E) = x(dE/dx)$, due to collisions with the atomic electrons along its path. In metals, these atomic electrons are essentially free so that large energy transfers result, i.e, the dE/dx is high. The probability of it reaching the surface with enough energy to overcome the potential barrier is therefore greatly reduced. This essentially restricts the usuable volume of the material to a very thin layer near the surface. The thickness of this layer is known as the *escape depth*. In contrast, semiconductors have an energy band structure with only a few electrons, those in the conduction and valence bands, being approximately free. The rest are tightly bound to the atoms. A photoelectron ejected from the conduction or valence band thus encounters less free electrons before reaching the surface. The only other possible collisions are with electrons bound to the lattice atoms. But due to the larger mass of the latter, little energy is transferred in these collisions. The photoelectron, therefore, is much more likely to reach the surface with a sufficient amount of energy to escape. The escape depth is thus much greater and the conversion efficiency higher.

3.3 Operating Parameters

3.3.1 Gain and Voltage Supply

The gain of a PM depends on the number of dynodes in the multiplier section and the secondary emission factor δ, which is a function of the energy of the primary electron.Figure 17 shows this dependence for several materials. In the multiplier chain, the energy of the electrons incindent on each dynode is clearly a function of the potential difference between the dynodes so that we can write

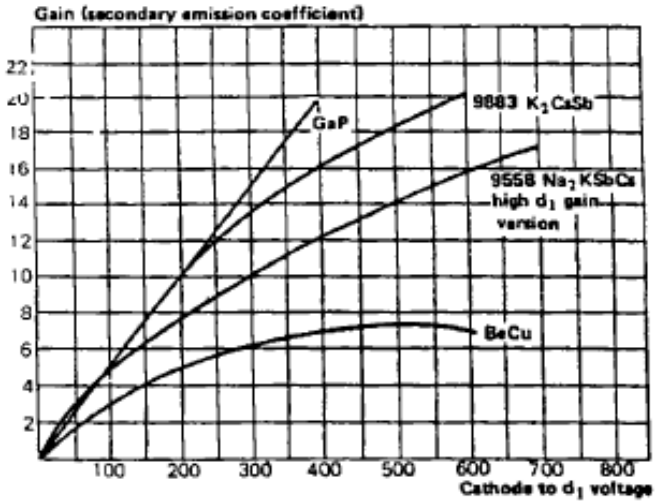

Figure 17: Secondary emission factor for several dynodes materials

$$\delta = KV_d \tag{19}$$

Assuming the applied voltage is equally divided among dynodes, the overall gain of the PM is then

$$G = \delta^n = (KV_d)^n \tag{20}$$

From which is interesting to calculate the number of stages n, requireed for a fixed gain G with a minimum supply voltage V_b. Thus

$$V_b = nV_d = \frac{n}{K} G^{\frac{1}{n}} \tag{21}$$

minimizing, we find,

$$\frac{dV_b}{dn} = \frac{1}{K} G^{1/n} - \frac{n}{K} \frac{G^{1/n}}{n^2} lnG = 0 n = lnG \tag{22}$$

for operation at a minimum V_b. Apart from practical reasons,operating at the minimum voltage is desirable rom the point of view of noise,etc. However, this comes into conflict with transit time spread and other factors (the number of pins,for example) which often results in the use of higher voltages. An important relation which should be noted is the variation in gain with respect to the supply voltage. Thus we can calculate

$$\frac{dG}{G} = n \frac{dV_d}{V_d} = n \frac{dV_b}{V_b} \tag{23}$$

which for n=10 implies a 10% variation in gain for a 1% change in V_b. Thus to maintain the gain stability of 1%,the voltage supply must be regulated to within 0.1%.

3.4 Coupling to The Scintillator

In contrast to what it is the internal reflection requirement of the scintillator, the coupling between the scintillator and the PM must be made to allow a maximum light transmission. Air can not be left, optherwise portion of the light could be trapped in the scintillator. Optical contact between the two should be made with a material whose index of refraction is as close as possible to the scintillator one and the PM window. And the most common agent is silicone grease or oil. For organic scintillators, the optical coupling with silicone is perfect except for the refractive indices of the scintillator, grease and PM window are almost identical.

3.4.1 Multiple Photomultipliers

Light collection could also have been increased by placing a second PM onto the other face of the scintillator, in the case it is possible to put another one there. Light escaping from this end would be detected by this PM and its signal could be summed with the other to give the total pulse height. This kind of configuration involves more electronics. For small detectors ,such a solution would be somewhat extravagant as the simpler reflection technique provides very good results. For larger counters where many reflections would occur and where the attenuation of light becomes a factor, the use of multiple PM's may be the only way to obtain efficient light recovery and uniform response 18

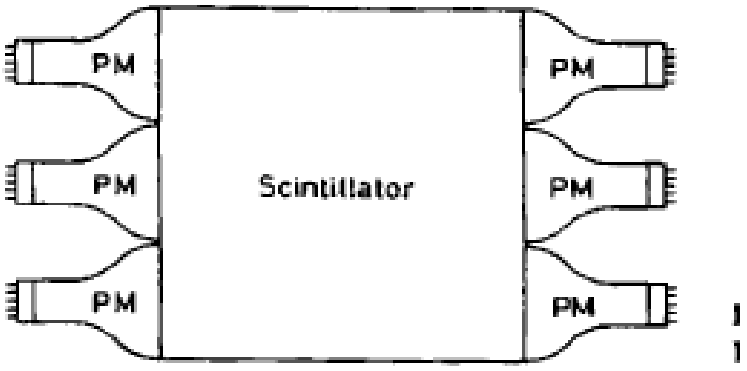

Figure 18: A scintillator viewed by multiple PM's for better light collection efficiency

4 The Trigger System:Introduction (Cristina)

The experimental set up for ths work is shown in fig. 38. It consists of three plastic scintillation detectors; two of them are placed on the top of the organic liquid scintillator, and one not just that but it will be above a 10 cm layer of lead as well;they are both provided with a PMT and will be called S1 (which is the one above the lead's layer) and S2 (the one placed underneath). Beneath the liquid scintillator, that represents the fulcrum of the muons decay detections, a bigger plastic scintillator is placed and it is coupled to two different PMT, that we can indicate with S3 and S4.

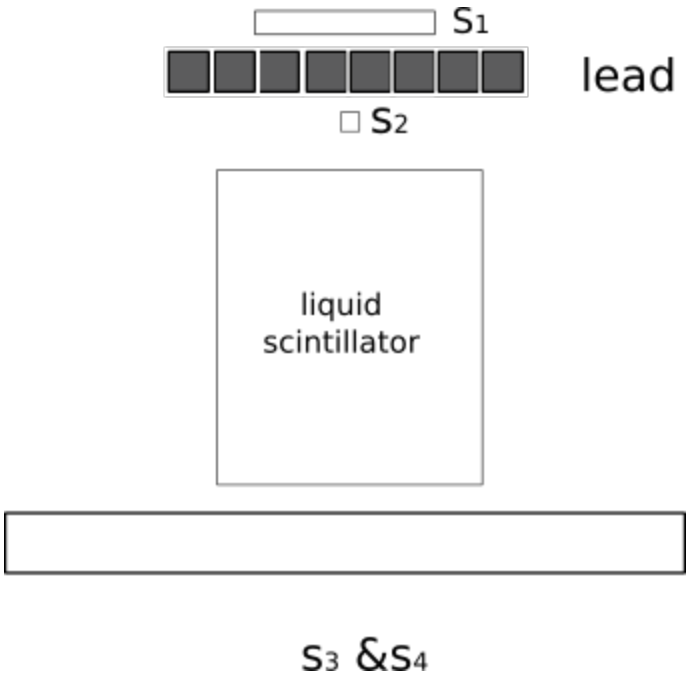

Figure 19: Set up

Thanks to this configuration and set up all the scintillators can work all together to make the *Trigger System*

4.1 Experimental Set Up and Strumentation

- **Two Plastic Scintillators (S1 and S2)**

  We worked with two plastic scintillator bars with dimension of $S1 = 17cm * 8cm$ and $S2 = 20cm * 3,3cm$ with a distance between them of $h = 36,5cm$. These two scintillators are coupled to two photomultipliers at their ends. It is important that the these two are smaller than the liquid scintillator so that if a cosmic ray hits one of these two we are still sure it will fall in the big block of scintillating liquid.

- **A Big Plastic Scintillator coupled with two PM's (S3 and S4)**

  This big scintillator has got at each end is coupled a photomultiplier.S3 is coupled to a Photomultiplier tube assembly H2431-50 (hamamatsu) at 8 stages with Linear-focused dynodes structrure. S4 is coupled with an EMI 9954KA. Not being able to find the exact data sheet for this specific photomultiplier we used the one given for the series 9954,where the letter give us a series of specfication about the tube. This one is a 12 dynodes stages tube of linear-focused design for good linearity and timing.The letter "K" in our example refers to the base and indicates that is capped and the letter "A" indicates that it follows a single order to selected specification. Characteristics for the two photomultipliers are reported in Table 2 and 20

Assembly Size	Dia.60 mm
PMT Tube Size	51 (2) mm
Built-in PMT Type No.	R2083
Photocathode Area Shape	Round
Photocathode Area Size	Dia.46 mm
Wavelength (Short)	300 nm
Wavelength (Long)	650 nm
Wavelength (Peak)	420 nm
Spectral Response Curve Code	400K
Photocathode Material	Bialkali
Window Material Borosilicate	glass
Dynode Structure	Linear-focused
Dynode Stages	8
(Max. Rating) Anode to Cathode Voltage	$-3500V$
(Max. Rating) Average Anode Current	0.61 mA
Anode to Cathode Supply Voltage	$-3000V$
(Cathode) Luminous Sensitivity Typ.	80 $\mu A/Im$
(Cathode) Blue Sensitivity Index	10
(CS 5-58) Typ.	
(Anode) Luminous Sensitivity Typ.	200 A/lm
(Anode) Gain Typ.	2.5 x 10^6
(Anode) Dark Current (after 30min.) Typ.	100 nA
(Anode) Dark Current (after 30min.) Max.	800 nA
(Time Response) Rise Time Typ.	0.7 ns
(Time Response) Transit Time Typ.	16 ns
(Time Response) Transit Time Spread Typ.	0.37 ns
(Anode) Pulse Linearity (2% deviation)	100 mA
(Anode) Pulse Linearity (5% deviation)	150 mA

Table 2: Specification $H2431-50$

So from the two tables we can extract the limit in voltage for our tubes, which are rispectivelly -3500 V for S3 and -2800 V for S4.

- **CAEN 40 Channel High Voltage System**

  The SY127 is a High Voltage System featuring modularity and high flexibility.The

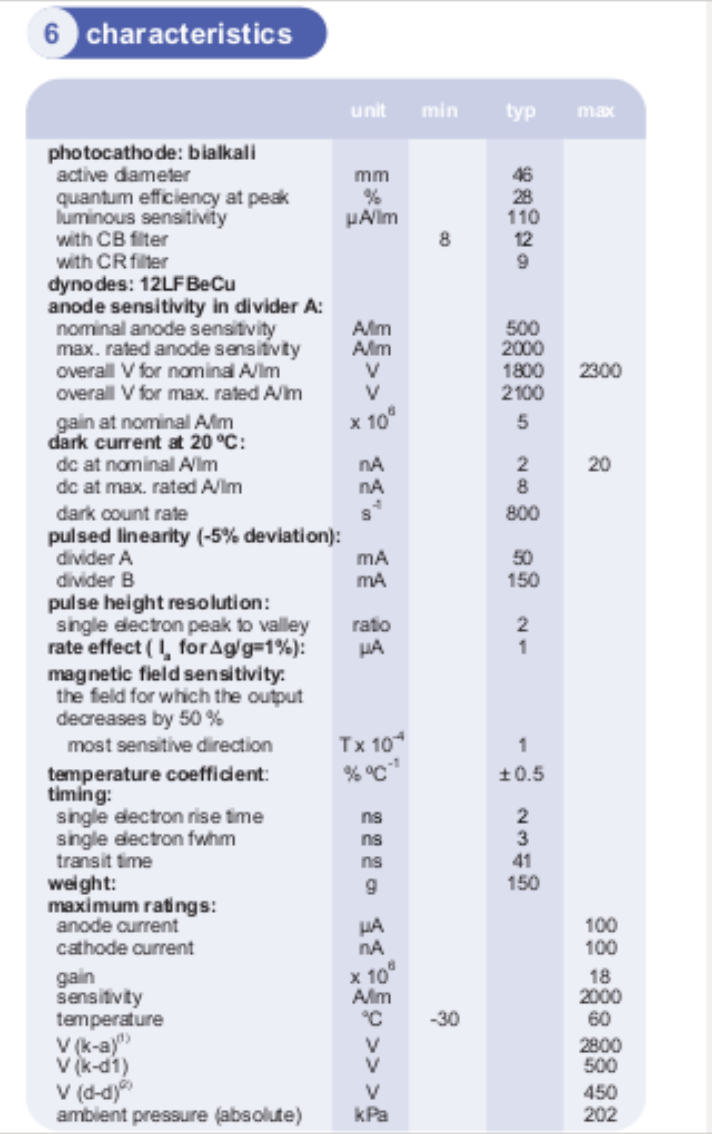

6 characteristics

	unit	min	typ	max
photocathode: bialkali				
active diameter	mm		46	
quantum efficiency at peak	%		28	
luminous sensitivity	µA/lm		110	
with CB filter		8	12	
with CR filter			9	
dynodes: 12LFBeCu				
anode sensitivity in divider A:				
nominal anode sensitivity	A/lm		500	
max. rated anode sensitivity	A/lm		2000	
overall V for nominal A/lm	V		1800	2300
overall V for max. rated A/lm	V		2100	
gain at nominal A/lm	x 10^6		5	
dark current at 20 °C:				
dc at nominal A/lm	nA		2	20
dc at max. rated A/lm	nA		8	
dark count rate	s^{-1}		800	
pulsed linearity (-5% deviation):				
divider A	mA		50	
divider B	mA		150	
pulse height resolution:				
single electron peak to valley	ratio		2	
rate effect (I_a for Δg/g=1%):	µA		1	
magnetic field sensitivity:				
the field for which the output decreases by 50 %				
most sensitive direction	T x 10^{-4}		1	
temperature coefficient:	% °C^{-1}		± 0.5	
timing:				
single electron rise time	ns		2	
single electron fwhm	ns		3	
transit time	ns		41	
weight:	g		150	
maximum ratings:				
anode current	µA			100
cathode current	nA			100
gain	x 10^6			18
sensitivity	A/lm			2000
temperature	°C	-30		60
V (k-a)(1)	V			2800
V (k-d1)	V			500
V (d-d)(2)	V			450
ambient pressure (absolute)	kPa			202

Figure 20: Specification $EMI9954kA$

System has been designed to power a wide range of detectors. Suitable for both major experiments and for the laboratory tests.It has got up to 4000 channels controlled from a single point.It's dotated with both positive and negative polarity and under and over-voltage signalling and overcurrent protection for each channel.

- **CAEN N471 2 Fold HV Power Supply**

  It's a 2 channels in a single unit power supply wih high flexibility to power a wide range of detectors, with positive or negative polarity selectable for each channel and output ranges from ±3KV/3mA or ±8KV/1mA with $1\mu A$ of resolution.

- **CAEN N417 8 Channels Low Threshold Discriminator**

  The CAEN model N 417 8-CHANNEL LOW-THRESHOLD DISCRIMINATOR is a one unit wide NIM module equipped with 8 independent non-updating discriminating channels which let us convert analogic signals into discriminated ones. Each

channel accepts both negative and positive high-impedance input signals in the range from 1.5 mV to 250 mV (absolute values). Two parallel inputs ("IN" connectors) per channel are provided: the unused connector allows the user to terminate the input signal appropriately.

- **CAEN N405 Triple 4-Fold Logic Unit/Majority with VETO**

  Equipped with three indipendent sections with 4 standard NIM inputs each, with AND, OR ,MAJORITY function selectable for each section.

- **N145 Quad Scaler and Present Counter-Timer**

  It is a double unit NIM module that includes four independent 8-digit up-counters, plus a fifth 7-digit down-counter that can be used either as a preset counter or as timer.

- **Dual Timer-100ns delay**

  We are talking about passive delay lines that introduce a delay proportional to the length of the signal. The delay lines are made up of calibrated coaxial cable stubs for high accuracy delay and do not require power supply.

4.2 Preliminary Steps

Before we could be able to make our measurament we had to make sure everything was of course set up in the right way to allow us to execute a precise measure. Of course we had to make sure all the cables were in place, which means connect all the scintillators to the High Voltage supply and as well to be able to get the output signal, the first two scintillators go directly into a discriminator to get a logic signal out, whilst S_3 and S_4 go first to a *FAN-IN FAN-OUT module*, which creates a copy of the signal to then send it to the *Discriminator module*, and to a counter, and to be able to create conicidence' signals. Done this, we studied the performance of the scintillators we were dealing with. First of all we had to understand what kind of voltage we must have gave them to make sure they were working in efficiency. So first 2 steps have been:

- Determination of the discrimination thresholds on the signal from the PM's;
- Determination of the operating points for the scintillators;
- Study the Coincidences;

4.2.1 Discrimination thresholds on the signal from the PMT's

For our experience we needed to study two kind of triggers:

- the passing event trigger
- the decay event trigger

So for the scintillators we are dealing with we needed two different graphics :

$$H \rightarrow i$$
$$H \rightarrow \nu$$

Now because the current "I" is dominated by the resistive divider, the Ohm law will dominate the process and we should expect a linear response. On the other side the response when we are analyzing the second option with the counting rate will have an esponential trend.
So having taken into consideration 3 different thresholds, we took a few measurements of the current "I" and the rate "ν". So we connected the scintillator coupled with the photomultiplier to the High Voltage supply and we took first a few measurements of the current "I" changing the input voltage "HV". We report the graphic and the relative data table. The errors on the values are linked to the "fondo-scala" and in our case is:

$$\sigma_V = \pm 1V \qquad\qquad \sigma_I = \pm 1mA$$

In our particular case we indicated with V_0 the input voltage we gave and with V_{mon} the actual signal the devide was receiving and we read it from the monitor

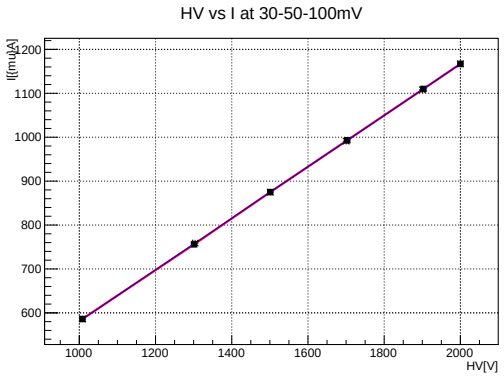

Figure 21: S1:threshold 30mV,50mV and 100mV

$V_0(V)$	V_{mon}	$I(\mu A)$
1000	1008	586
1300	1301	756
1500	1501	875
1700	1703	993
1900	1903	1110
2000	2000	1167

Table 3: S1:V_0 vs I at 30 mV threshold

We are going to make the same measurements on the other scintillator situated underneath the first one. We report the results in the table to which we associated the same uncertainties previously used.

Table 4: S2: $V_0(V)$ vs $I(\mu A)$ at 30 mV threshold

$V_0(V)$	V_{mon}	$I(\mu A)$
1500	1501	874
1550	1551	903
1600	1601	933
1650	1653	962
1700	1701	992
1765	1766	1033
1800	1800	1050

What we can notice is that first signals shown on the oscilloscope is around 1500 V. At lower voltage electromagnetic field are not strong enough to accelerate electrons properly. In both analyzed cases we find a linear trend in any of the ranges studied. We reported just the table at 30 mV threshold but we obteined very similar result for the other

two thresholds, with an expected linear trend, as we show in fig. 21 The same thing has been done with the second scintillator S2,but in the process we realize that the second scintillator had some problems at the 30 mV threshold, and the rate started to be out of control because we were out of the efficiency range, and so the same with the 60 mV threshold. We took then a set of data at 40mV of threshold which we report below with the relative graphics

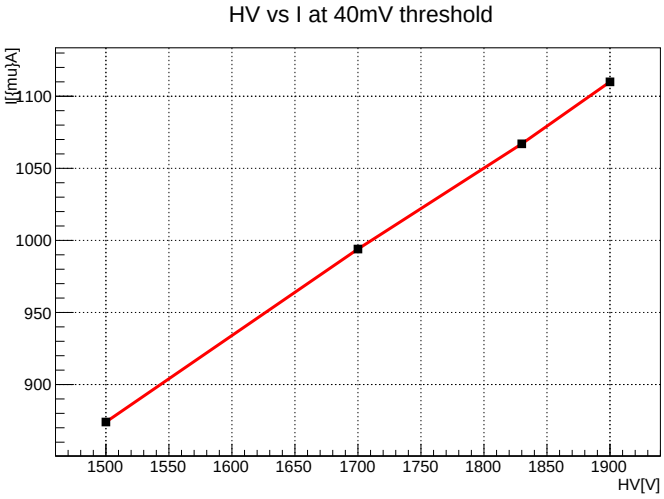

Figure 22: S2 vs I:threshold 40mV

4.2.2 Rate At The Changing Of The Voltage Supply Applied

As previously we took a few points to check the trend at the change of the voltage applied of the relative rate for each of the two scintillators, since we knew we were expecting an esponential trend of thi one. Since we know that counts follow a Poisson distribution the error associated is the square root of the number of particle we detected. We took the same measurements at the same voltage values for the same three threshold values chosen. We report the tables with the values and the relative graphics :

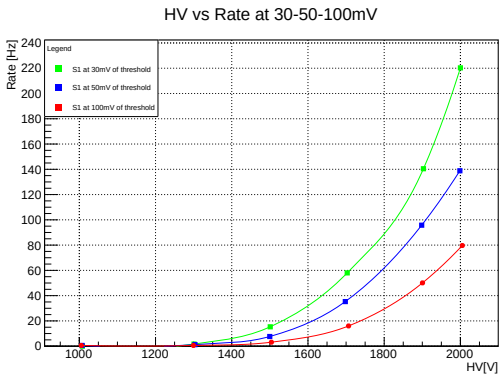

Figure 23: S1:threshold 30mV,50mV and 100mV: HV vs RATE

$V_0(V)$	V_{mon}	$\nu(Hz)$	$\sigma_\nu(Hz)$
1000	1008	0	0
1300	1301	1.68	1.29
1500	1501	15.33	3.91
1700	1703	58.01	7.61
1900	1903	140.45	11.85
2000	2000	220.28	14.84

Table 5: S1:V_0 vs Rate at 30 mV threshold

Again the same process has been followed for the second scintillator S2, but when we were doing the the rate we realized that with a threshold of 30 mV we were going to have some issues because suddenly the scintillator was going to saturate. So we reapeat the meseasument with a minimum threshold according to noise of 40 mV. Also because we realized from numbers that we could see something starting at 1300 V for this threshold we took a few significative points starting at 1500 V:

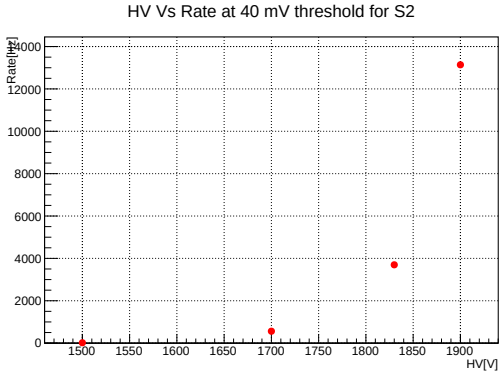

Figure 24: S2 threshold 40 mV - HV vs RATE

$V_0(V)$	V_{mon}	$\nu(Hz)$	$\sigma_\nu(Hz)$
1500	1501	17.9	4.23
1700	1703	562.6	23.71
1830	1833	3697	60.80
1900	1903	13139	114.62

Figure 25: S2: $V_0(V)$ vs $RATE(Hz)$ at 40 mV threshold

Due to the analysis done on the two devices we decided to set the discrimination thresholds at 30mV for S1 with a voltage of 1750 V and at 40 mV for S2 with a voltage of 1800 V to begin with according the the background noise. Now to determine the right working point which garanties us that the two scintillators are working in efficiency we should fix one of the scintillators' voltage supply to one middle value,make the other one change and register the rate ν.What we should obtain is a plateau,chosing a value in the middle of the plateau as a value for the high voltage and fixing the scintillator at that value and make the one that before we kept at a fixed value we should find exactly the same value we set to begin with which corrispondes at two reasonable working points for both of them. Due to technical issues we couldn't do this in details.

4.2.3 Study of S3 and S4

Once we determine how to set up S1 and S2 we have to do the same with the two other scintillators S3 and S4. Because of their configuration that sees a second PM onto the other face of the scintillator in this case we don't need to find the right working point by putting ourselves in the middle of the plateau as we meant to do for S1 and S2. Infact S3 and S4 are connected by the fact that reveal the same physics at the same time, so what we can do is make sure that both of them are set up at the same rate.
So as we did before we set the discrimination theresholds at the minimum according with the background noise which we checked sperimentally through the oscilloscope and then we can make a few measurement of the rate changing the voltage and once we did it for both we can underline the two voltage settings are going to give us the same rate for the two scintillators. Here's the results:

$V_0(V)$	$\nu(Hz)$	$\sigma_\nu(Hz)$
1500	2.8	1.67
1700	36.6	6.04
1830	105.4	10.26
1860	150.6	12.27
1880	189	13.74
1890	213.9	14.62
1900	240	15.49

Table 6: S3: $V_0(V)$ vs ν at 30mV threshold

$V_0(V)$	$\nu(Hz)$	$\sigma_\nu(Hz)$
1500	2.8	1.67
1700	36.6	6.04
1830	105.4	10.26
1860	150.6	12.27
1880	189	13.74
1890	213.9	14.62
1900	240	15.49

Table 7: S4:V_0 vs ν at 40mV threshold

4.3 Study of Coincidences' Signals

Our trigger set up goes through the "contruction" of the logic coincidence of two or more signals. To put two or more signals in coincidence of different devices we have to know the coincidence trend of the single device. So we did start with the analysis of the coincidence of the first two scintillators: $S1 \otimes S2$. In this way I can, of course,get rid of some noise as well.

Because of the kind of trigger we know we are going to need for our experiment, we studied of course the coinciedence of $S3 \otimes S4$. Once everything has been set, we put our coincidence in place with the right strumentation following the configuration below

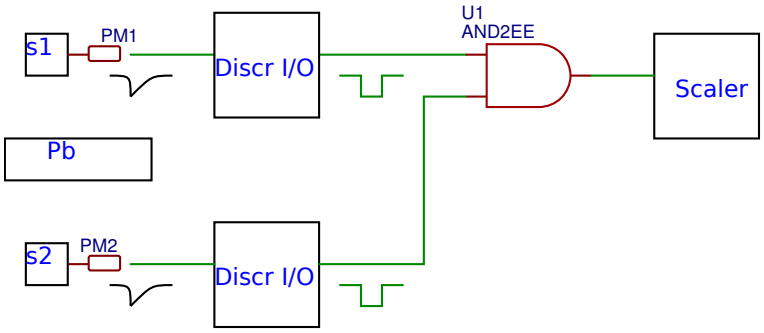

Figure 26: $S1 \otimes S2$ coincidence

What we want to know about the two coincidences S1⊗S2 and S3⊗S4 are three quantity, which are

- The High Voltage Applied HV
- The Threshold Voltage V_{thr}
- The signal width ω_t

I personally took care of all the values above concerning the S3 and S4 scintillators. Now the first quantity has been set by us previously, according to the scintillators and PM's characteristics.
The Threshold voltage that we have to choose has to be reasonably low, but in good agreement to the noise, so we have to consider a window like ($3V_{noise} \Longleftrightarrow V_{thr}^{max}$). So we determined from the oscilloscope what was the value for V_{thr}^{min}=$3V_{noise} \simeq = 50mV$ and then the maximum value, which resulted being: $V_{thr}max$= a threshold of 10 mV with a peak of

100 mV.
In regard to the width instead, the minimal one can be read from the data sheet, and the maximum one can be obtained with the casual coincidences:

$$\nu_1\nu_2\omega \rightarrow \nu_{noise} \tag{24}$$

Thus from data sheet as we said we read the minimum width,which is $\omega_{min} = 500MHz \rightarrow 2ns$ and from the relation above we found the noise's rate:

$$\omega_{max} = \nu_1\nu_2\omega \rightarrow \nu_{noise} \rightarrow \nu_{noise} \rightarrow 0.15ns \tag{25}$$

So we have the width's range as well. Another thing to consider is the time delay between S3 and S4 because we specified previously these two are coupled so they can actually detect the same particle. Then using the coincidence S3⊗S4 as an external trigger, we checked the time delay of S3 and S4, of which we report the shot taken from the oscilloscope, in which we can see a delay of S3 respect to S4.

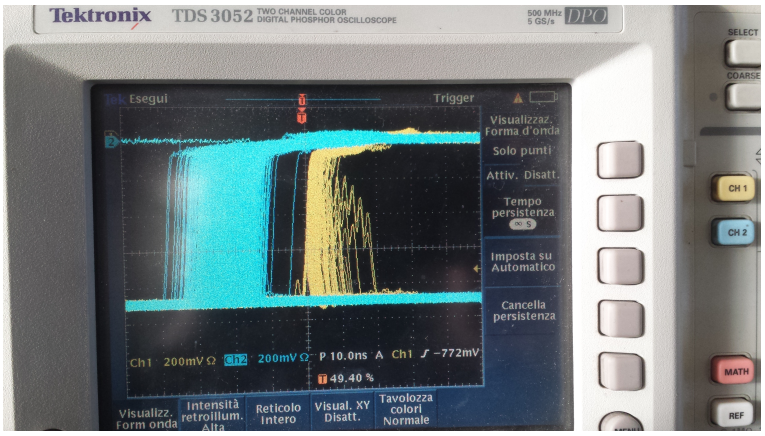

Figure 27: S3 and S4 delay

4.4 Studying Of The Trigger's Rate

The next step has been to determine the acceptance of our detector, which refers to a geometric fiducial volume of the detector, *i.e the ratio between the particle detected and the incident ones*. The geometrical acceptance depends in general on the polar and azimuthal angle of the incident particle. It may also depend on the particle momentum, since charged particles below a certain threshold might be stopped due to energy loss before reaching the detector. Starting from the following formula,which is the muons Integral Flux relation:

$$\phi_\mu = \int \frac{dn}{dEd\Omega dAdt} \tag{26}$$

We have to determine the single object that appear in it. First od all the solid angle Ω. To do so we can approximate our system with a rectangular pyramid. Once we know that, we can use the simple formula which gives us the solid angle:

$$\Omega = 4\arctan\frac{\alpha\beta}{2h\sqrt{4h^2+\alpha^2+\beta^2}} \tag{27}$$

Where α and β are respectively the base lenght and the base width of the area we chose as the relevant one for our analysis, which in our case occurs to be S1, and the "h" is the pyramid height, that for us is the distance between the 2 scintillators where the vertex of the pyramid falls exaclty on the S2 scintillator. These are all quantity we could measure with no problem at all obtaining the following:

$$\alpha_{S1} = 17cm \qquad \beta_{S1} = 8cm \qquad h = 36.5cm$$

With these value we obtain a reasonable solid angle for our system configuration

$$\Omega = 0.098sr$$

Now to complete the study of the geometric acceptance, all we have to do is multiply this value for the efficient area we've chosen, which is $A_{S1} = 136cm^2$, that will give us the *angular efficiency for the detector*. Now what's really relevant for us is to evaluate the expected rate for our configuration, so that we can compare that with the experimental one given by our trigger set up. To do so, we have to consider that in the flux' formula we have the quantity $\frac{dn}{dE}$, which is everything but an obvious value. There are a few aspects,in fact, to take into consideration; first of all the fact that between the two top scintillators S1 and S2 there is a layer of lead of 10 cm. When a particle hits the first scintillator before arriving to the S2 surface will loose energy when passing through matter. Underneath S2,as well, before arriving to the coupled S3$\oplus$S4 surface, a particle will have to go through the liquid scintillator, where again will loose energy due to the ionization process.

So finding this quantity is less easy than it can actually appear due to the integral and to all the variables that come into place. So to overcome this problem we used a table, where we could read for different material, in our case *Lead* and for what concerns the liquid scintillator, given the "different" composition and taken that there wasn't a value for Mineral Oil, we used the closest element, i.e *Water*. In the range tables that we used, the stopping-power is given for different materials in $\frac{g}{cm^2}$,which means that to obtained the actual value of the layer we are interested in, we have to divide for the density of that specific material.

First of all,because the tables are different of course for different particle due to the different masses, we looked for the one we were interested in, knowing that the muon's mass is 105 MeV. Then we looked for the right value under the column *Lead*, because we knew we had 10 cm of lead. The value we read from the tables for muons=105 MeV, for the right stopping-power is: $1.148 \cdot 10^2 \frac{g}{cm^2}$; if we divide this value for the lead density which is $\rho = 11.350g$, we get :

$$(\frac{dE}{dx})_{Pb} = \frac{1.48 \cdot 10^2}{11.350} = 10.11cm \tag{28}$$

which corrispondes to the minimum energy required of:

$$E(MeV) = 165MeV$$

This value gives us the minimum energy required for a muon to go through the 10 cm lead layer. We did the same thing with the water of the liquid scintillator, i.e. 33 cm of Water:

$$(\tfrac{dE}{dx})_{wat} = \tfrac{33.01}{1.000} = 33,01cm$$

And for this, the energy value results to be

$$E(MeV) = 105MeV$$

And If we consider the efficiency area the one made of S1, which gives us an area of $A = 136cm^2$; The most akward element we have to determine is now $\frac{dn}{dE}$,i.e the number of particle over the energy unit. To do so, we consider, first of all the differential spectrum of secondary cosmic rays, for muons. The relative plot shows the $\frac{dn}{dE}$ against *the Muons Momentum*. One thing we need to be careful of is the fact that from all the considerations made above we have the energy range of our integral, but in this plot we have to report everything based on the momentum to try to estrapolate the right value for the events' number. So we know that our energy range is :

$$105MeV < E_\mu < 270MeV$$

And knowing the relation that links energy and momentum, which is

$$E^2 = p^2 + m^2$$

we get two momentum value and therefore our momentum range which results to be:

$$127MeV < p_\mu < 248MeV$$

So from figure 28 we can see we made the two cut in corrispondence of the two momentum values, so that we can extrapolate from the figure the number of events that we are going to detect in the range of flux that we selected.

The number of events that we read is $0.16 \cdot 10^{-2}$, because taken from a differential spectrum, this gives us the value dn, which must be then multiplied by the value of the area and the solid angle and of course we have to integrate in the right value of energy/momentum we discussed previously. Said that we have :

$$dW = dn \cdot dp \cdot d\Omega \cdot dA = 0.003GeV \tag{29}$$

But with this relation we consider the momentum as we said, and we need the quantity $\frac{dn}{dE}$, so we have to divide the dW that we found for dE, which is $dE = 105MeV = 0.1GeV$; and this gives us an expected rate for our trigger of:

$$\phi_\mu \cdot \Delta\Omega \cdot A \rightarrow \nu_{TRG} = 0.03Hz \tag{30}$$

4.4.1 The Trigger

The trigger system is made thanks to the simultaneous work of all three plastic scintillators we have in our hands. We already define how scintillators work together with the PM's. Building the trigger we have to make sure all different components speak to each other in coincidence. So from the photomultiplier is usually connected with a *discriminator*, in which is set a *Threshold Voltage* that allows only analogical signals above it, to generate a NIM signal .The discriminator can be connected to a *counter* that registers the NIM digital signals in a specific *time range* we set. Because of the purpose of our work, we need to be able to analyze our data sets, reason for which the signals *time-trend* are studied

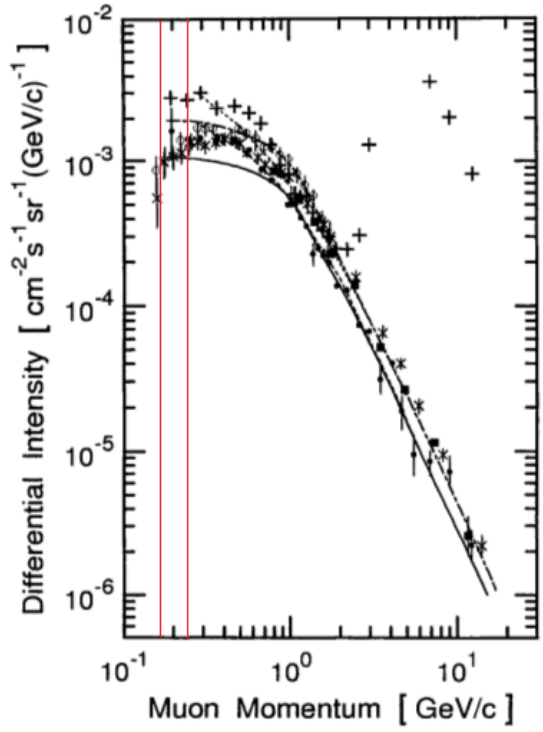

Figure 28: Differential spectrum of muons

	$Voltage(V)$	$Threshold(mV)$
S1	1750	30
S2	1800	40
S3	1895	30
S4	150.6	40

through a *Flash ADC*. Then to create our trigger needed for our experiment, we connect the discriminator to a *coincidence module*, that allows us to count at the same time signals coming from different PM's . We remind in the following table the operating points we already analysed for every scintillator+photomultiplier' system.

We had the necessity to build two different triggers:

- the passing events trigger
- the decay event trigger

The first one done to select muons that get seen to the two top scintillators, pass through SL and then get detected by the lower scintillator, and the second one, to select the events that get detected by the two upper scintillation detectors and then decay into the liquid Scintillator LS.

4.4.2 Passing Events Trigger

To build the passing events trigger, we need the follow configuration

$$(S1 \otimes S2) \otimes (LS) \otimes (S3 \otimes S4) \tag{31}$$

So we send S1 and S2 into the *disciminator module* and then each of the logic signal of the two given from the output of the discriminator, again into a *coincidence module* together with the logic signal coming from LS, together with the coincidence of the two others S3 and S4. We sent then the main passing trigger to a counter, to check the expected rate. We can check the diagram for a passing events in fig.

4.4.3 Decay Events Trigger

As for the passing events trigger, we have to build a parallel diagram to create a trigger which it is going to select just muons that go into the LS and decay, and they get not detected by the coincidence $S3 \otimes S4$. The Trigger system is made sending the LS analogical signal to the flash ADC. Then a copy of the trigger is sent to the flash ADC for the acquisition system DAQ. The ADC is triggered by a S_1, S_2, LS and $\overline{S_3 \otimes S_4}$ coincidence, where the last one represents a veto coincidence. In this way a particle that passes through S_1 and S_2, that is detected by LS and not from $S_3 or S_4$ is acquired; In this configuration we supposed to maximize the detection of muons decays. Thanks to this kind of coincidence, there are also events acquired that are not represented by muons decay; this could be due to a the inefficiency of one or both of the photomultipliers. So this is the final set up:

$$(S1 \otimes S2) \otimes (LS) \otimes (\overline{S3 \otimes S4}) \tag{32}$$

so as we can see the difference from before is in the fact that we are going to take into consideration the coincidence of the two lower photomultiplier, as a *VETO*, which means that if by any chance there is an event going through the LS scintillator without decaying and then will arrive to the lower detector, this one is not going to be counted by the trigger, leaving us with just *decay events*.

What is relevant for the decay trigger is the *transit time* that has to be within the range of $3\boldsymbol{\nabla} \cdot 4ns$. We report in the fig. 29 and fig. 30 what was the output on the oscilloscope of the coincidence signals.

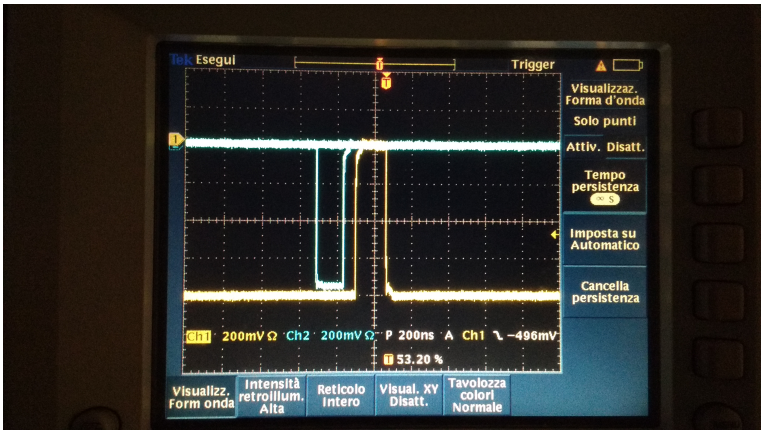

Figure 29: S_1xS_2 Vs S_3xS_4

In which the yellow signal represents the $S_1 \otimes S_2$ coincidence and the blu line represents the $S_3 \otimes S_4$ coincidence. As we can see the coincidence made by S_3 and S_4 starts before the one made with S_1 and S_2. To begin with the coincidence $S_1 \otimes S_2$ was starting before the other one, but what we want is that the big scintillator at the bottom gets the signal from all the other ones, the two top scintillators and the liquid scintillator. So this coincidence has to start before of all the others and end after all of them. Because of that, we had to put a delay on the S_2 of 100 ns through the *Dual Timer*, to reach the result we can see in the picture. On top of all of this, we have of course to make sure that the width of this coincidence is the biggest one, exactly to make sure that we include every other signal. That's why we set the time window at $1\mu s$, so we make sure that applies.

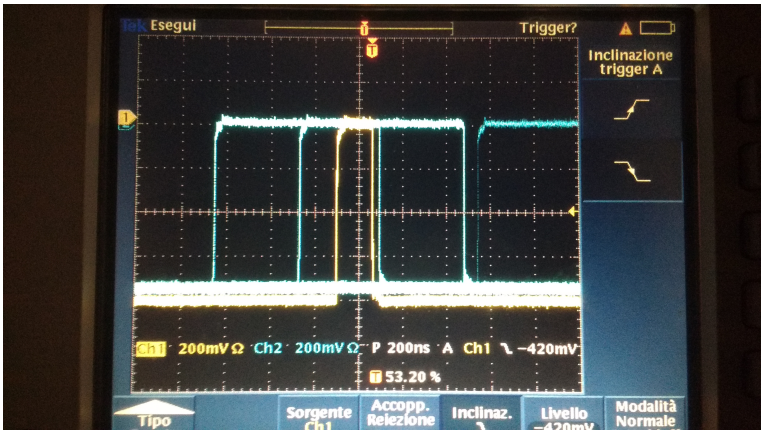

Figure 30: LSx(S_1xS_2)

5 DAQ system

The DAQ system consists of all devices and processes that are devoted to scan signals from physics measurements, acquire and convert them in a digital output. Once those observables are stored inside a computer, they can easily be analyzed.

5.1 DAQ hardware setup (Giulio)

Every acquisition system must rely on sensors to acquire an analogical signal, on cables to transport it and on analog-to-digital converters. In this work all files were stored inside the *farm*, a computer that runs a Scientific Linux distribution. It plays the role of managing with all the DAQ system.
To acquire the signals, we could use four different modules: two flash ADC boards and an Input/Output Register, all controlled by a Motorola board. A simple schematization is presented in fig. 31.

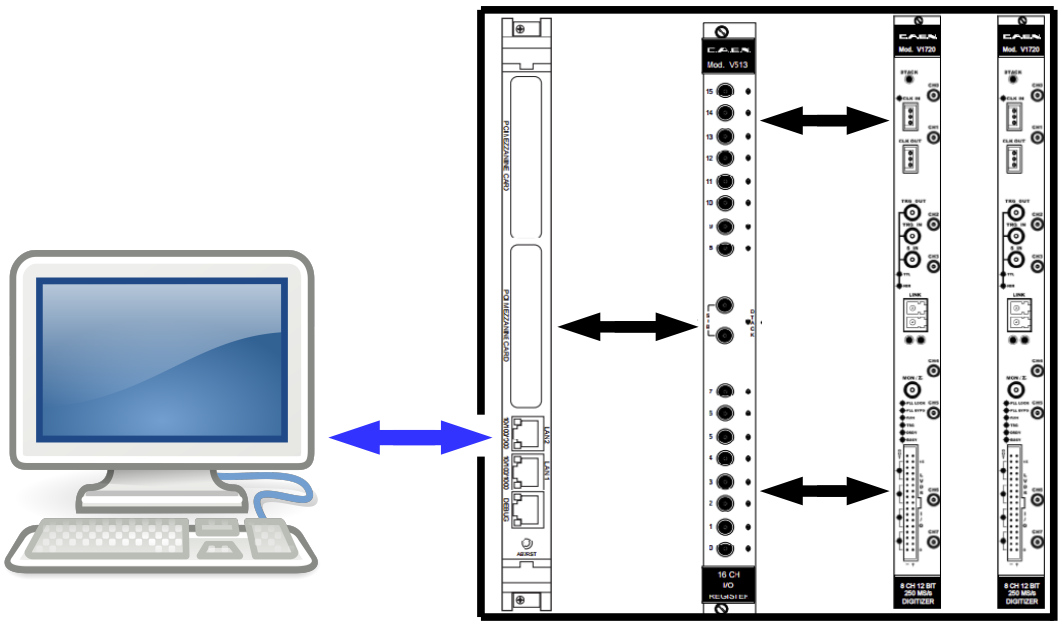

Figure 31: *DAQ system. From left to right: Farm; Motorola MVM6100; Caen V513 I/O Register; two Caen V1720E Flash ADC.*

The electronical boards can communicate via the VME crate. It is a high speed and high performance bus system connecting all the modules linked. It was created by combining VERSAbus electrical specifications (1979) with the Eurocard format, resulting in the VMEbus Revision A - 1981 specification.

Farm main processes

IP address: 192.168.38.217 [23]
Through the Farm it's possible to control the entire DAQ system. Its main functions are:

- Manage the Motorola board;
- Data production and analisys.

In order to launch the acquisition system and link the Farm and the Motorola, it is necessary to load the following packages on the Farm, directly from terminal:

packman farm : environment variable setting. The process launches all packages inside the farm for starting the Motorola jobs. Necessary to access the DAQ software;

Farmreceive : receives data from the Motorola;

Farmwrite : writes the file of the corresponding run.

Some actions inside the farm may require to log as superuser. To do this, just type:

```
su
```

PSW: `Giasone`

5.1.1 The Motorola MVM6100

The MVME6100 is a VMEbus single-board computer with a real-time operating system. It is based on the MPC7457 processor, the MV64360 system controller, the Tsi148 VME Bridge ASIC, up to 1 GB of ECC-protected DDR DRAM, up to 128MB of flash memory and a dual Gigabit Ethernet interface. The processor speed is 1.267 GHz, while the bus clock frequency is 133 MHz.
Through the VME bus it can initialize all the boards of the crate. In this work an I/O register and two fADC were used. During the acquisition it controls all the boards memories, getting data from their buffers. Then, it packs and sends those data to the Farm. This means that all boards buffers are continuously filled with new data and empty from the Motorola.

Motorola functions

IP address:192.168.159.46
This module works via two main processes: L2ATLAS and L2SEND. The former keeps data from the other boards and pack them, while the latter sends them to the farm. The Motorola is then used to:

- Initialize all the boards of the same crate;
- Manage the data acquisition of the boards and their memory;
- Collect data from the boards buffers and empty them;
- Pack and send data to the farm.

[23] If the user is currently working on the farm, just type: `ssh daq@localhost` (PSW: `work-1`).

5.1.2 The CAEN V513 I/O Register

The V513 is a 1-unit wide VME module that implements a 16 channel general purpose I/O module. Each of the channels can be programmed as **Input** or **Output** independently and can work in Positive or Negative logic. The I/O channels rely on std. NIM logic levels, with a 50 Ω impedence.
Each of the 16 channels can be configured independently via 16 Status programmable registers. The V513 is used by the Motorola to empty the two fADC.

5.1.3 The CAEN V1720E FlashADC

The V1720E is a 1-unit wide VME 6U module housing 8 channels, with a 250MS/s sampling rate, so it provides a 4 ns time resolution. A 12 bit memory for voltage is available, featuring a 2 Vpp full scale range: it corresponds to a 2V/4096 = 0.49 mV per bin sampling (12 bit $\rightarrow$ $2^{12} = 4096$).
The module features a front panel clock/reference In/Out and a PLL for clock synthesis from internal or external references. In our work, the clocks of the two fADC were synchronized. Every channel is equipped with a 1.25 Msamples SRAM memory buffer, divided in buffers of progammable size (from 1 to 1024). The data stream is continuously written in a circular memory buffer. When the trigger occurs, the FPGA writes further N samples for the post trigger and freezes the buffer, that can be read both via VME bus and via Optical Link. The acquisition can continue without dead-time in a new buffer. The readout of a frozen buffer is independent from the write operations in the active circular buffer.
When the acquisition is running, a trigger signal allows to fill the active buffer with the pre- and post-trigger samples, whose number is programmable (fig. 32). Then, the buffer is frozen for readout purposes, while acquisition continues on another buffer.
In our work the acquisition window was set at 4000 samples, resulting in a total 16 μs time window, necessary to look for a muon decay (whose lifetime is of the order of $\sim 2\ \mu s$).

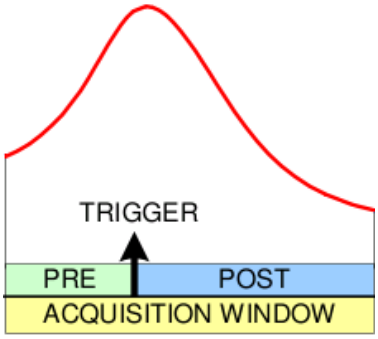

Figure 32: *pre- and post-trigger samples in the acquisition window.*

The board also implements two algorithms of "Zero Suppression" and "Data Reduction", that allow a remarkable reduction of the total processed data, through a threshold logic.
All channels in a board share the same trigger and so they store an event at the same time and in the same way. A trigger can be sent to the board externally, via front panel or software, or can be generated locally if the signal exceeds a certain threshold.

5.1.4 Work inside the Motorola

Farm and Motorola are linked via ethernet cable. In order to enter inside the Motorola type:

```
ssh daq@l2moto01
```

PSW: `ArgoDaq`

Inside the Motorola the following processes can be found:

packmanl2 : environment variable setting to access the DAQ software on the Motorola. Loads all packages from the farm, necessary to allow the board to work;

l2atlas (collector): loop process on all the boards, collects data, packs and sends them to the Motorola;

l2send : after packing, sends data to the farm.

These processes are physically located in the farm, because no files can be stored inside the Motorola. They can still be accessed from the Motorola, since they run on it.

fADC Configuration

All Flash ADC settings are contained inside `WaveDumpConfig.txt`. It consists of a list of all register options, that can be modified. The file is located in the following directory within the Motorola:

```
/home/soft/onl/maps
```

Every register is associated with a hexadecimal value, that can be read by the V1720E modules. In particular, we report:

8000 register Channel Configuration - sets the number of samples per word. In this work, we used the "Standard mode": data format is 32 bit long word, and each long word may contain 2 samples;

800C register Buffer Organization - allows to divide the available Output Buffer Memory into a certain number of blocks, i.e. sets the total number of samples for every buffer;

1n24 register Channel n ZH THRES - zero suppression mode for the n channel;

1n94 register Channel n Buffer Occupancy - sets the buffer occupancy, i.e. how many samples to save;

810C register Trigger Source Enable Mask - enables or disables the trigger source, select software or hardware mode;

8114 register Post Trigger Setting - sets the number of post-trigger samples;

8120 register Channel Enable Mask - allows to enable or disable channels [24];

[24] The value has to be hexadecimal, but refers to a binary one (1 = ch.on, 0 = ch.off). For example: 4 channels enabled = 1111 (binary) $\rightarrow$ 15 (decimal) $\rightarrow$ F (hexadecimal)

812C register Event Stored - number of events currently stored in the Output Buffer, cannot exceed the maximum number of available buffers.

In order to display the file related to the N-th board (0 or 1 in this case), just type:

```
more WaveDumpConfig_N.txt
```

or, in order to modify it, open the file using an editor (VIM or EMACS).
All values are requested to be hexadecimal. Furthermore, they do not have to be changed while the acquisition is running.

5.1.5 Acquisition strategy

For our work we can use two fADCs for the data acquisition. Each of them has a programmable time window, depending of how many buffers are used for a sampling. The first one (board 0) was programmed for a 16 μs window, wide enough to look for a muon decay. The second one was de-activated. In order to manage with the boards activation, open the settings file `geolab`, located in:

```
/home/soft/onl/maps
```

Then, comment/uncomment the line related to the board you want to de-activate/activate. The time window can be enlarged up to milliseconds. On the other side, for a wider one the total number of usable buffers decreases, not allowing a pipeline strategy. One has to find a compromise between the time window width and the data acquisition rate.
The board 0 (the only one we used) acquires:

CH0 a copy of the trigger;

CH1 the analog signal from the liquid scintillator;

Channel 2 (and eventually channel 3) were used in different ways during the work.
The number of post-trigger samples was set in order to have the first time window bin $\sim$1 μs before the trigger.
The Motorola board, once linked to the farm, can send the start pulse to the fADC (S_{in} channel), via the I/O register. This pulse commands the V1720 board start.

Trigger veto

The trigger signal from the coincidences cannot be sent directly to the fADC, because the acquisition system cannot accept an event while another event is being processed. A veto system must be implemented, in order to stop new triggers until the event is completely processed. This can be done with two Dual Timer modules (figure 33):
The "pure" trigger signal commands the first Dual Timer start, which generates a square wave signal. The fADC requires a positive signal as trigger, so the negative output is linked to the board (TRG channel). As the first trigger is received, the square signal commands the start of the second DT, whose output has the function of a veto for the first DT. The duration of the second DT signal must be set on infinite, keeping the first DT blocked from receiving new triggers, until the I/O register sends the RESET signal. Once

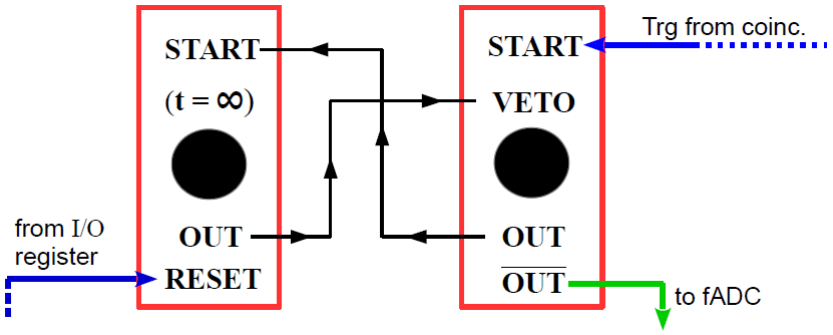

Figure 33: *Veto system for the trigger, with two Dual Timer modules.*

the second DT receives it, its output goes to zero, allowing a new event processing. While the system is processing an event, its status is called “busy” and the fADC cannot acquire any additional event.
The method described above is a software one, because it relies on the reset input sent by the I/O register. An alternative method can be applied, using the programmable pins located on the fADC, where one can read the busy signal. This is called hardware method and needs a LVDS board to be implemented.

In order to verify the correct setup of the experiment, a test was performed using fake well-known signals. They consist of a periodic square wave signal, generated by two coupled Dual Timers. Such configuration allows to determine the width of the waveform and its duty cicle. Furthermore, digital signals of known amplitude are necessary for the calibration of the Data Acquisition System.

Acknowledgements
For what concern this section, I would like to thank Antonio Budano and Paolo Branchini, for their exhaustive explanations about all electronic devices used in this work. I would say especially thanks to Antonio for his continuous help in the management of the DAQ system.

5.2 Farming, decoding and display of data (Valentina)

As described in the previous section fADC module is connected to the I/O Register and the Motorola by a VME crate. It scans input signal and saves data only if the Motorola commands it. After this step, data are stored in the Farm, connected to the Motorola by an Ethernet cable.
Thanks to this system it’s possible to acquire, save, decode and display data.

5.2.1 How to acquire data

To start acquiring data it’s necessary to log in as "daq" in the Farm, move on

/home/daq/vvecchio/NiNOS_DAQ

and then run

$./start.sh$

This command will open and external window, shown in Figure 34.
In the upper region of the window there are logo, date and time. Going down one can find seven different buttons, they are necessary to make this finite-state machine work. By definition of finite-state machine, the order in which processes run is fundamental. Following listed steps describe the correct way to make an acquisition.

1. Pressing on the red button **Configure** all processes that link the Motorola with the Farm will start. When in the Status Bar on the window will appear the word CONFIGURED the machine will be ready to go to the next state.
2. Pressing on the light blue button **Initialize** modules on the VME crate will be initialized. When this process will end the Status Bar will change in INITIALIZED.
3. Now the machine it's ready to acquire. Pressing on the orange button **Start Run** the machine will begin acquiring and saving data. When the machine will start to collect data the Status Bar will change in STARTED and a START TIME will appear.
4. Every time an event is acquired the Trigger Number will be incremented.
5. To stop the acquisition press **End Run**.
6. It's recommended to always press on **Reset All** after an acquisition.

During the acquisition *atlascollector* moves data from the fADC to the Motorola, then *l2send* sends data to the Farm and *farmreceive* collects them. At the end *farmwrite* writes data in a file named

$run\#N\_frm\_\#.000$

(where # stands for the run number indicated in the Current Run Bar on the run control window) located in the directory

/work/runs

5.2.2 Run File Structure and Decoding

To take a look at the run file [25] one can type on shell the following command, after being moved in the directory /work/runs

od -t x4 $run\#N\_frm\_\#.000$ | more

This can be very useful in preliminary settings of DAQ system, to check the goodness of acquisition before starting collecting data. Every run file contains hexadecimal words of 32 bit, divided in 5 columns. The first column in the od's output represents the byte offset in file, so it has no relevant informations and it must be ignored.
Events are organised following the structure of standard mode shown in Figure 35.
The first 14 words contained on the header plus other 4 words referred on hardware are used for the controls (to check if something went wrong during all processes, from the fADC to the farm).

[25] *od* is a program for displaying ("dumping") data in various human-readable output formats

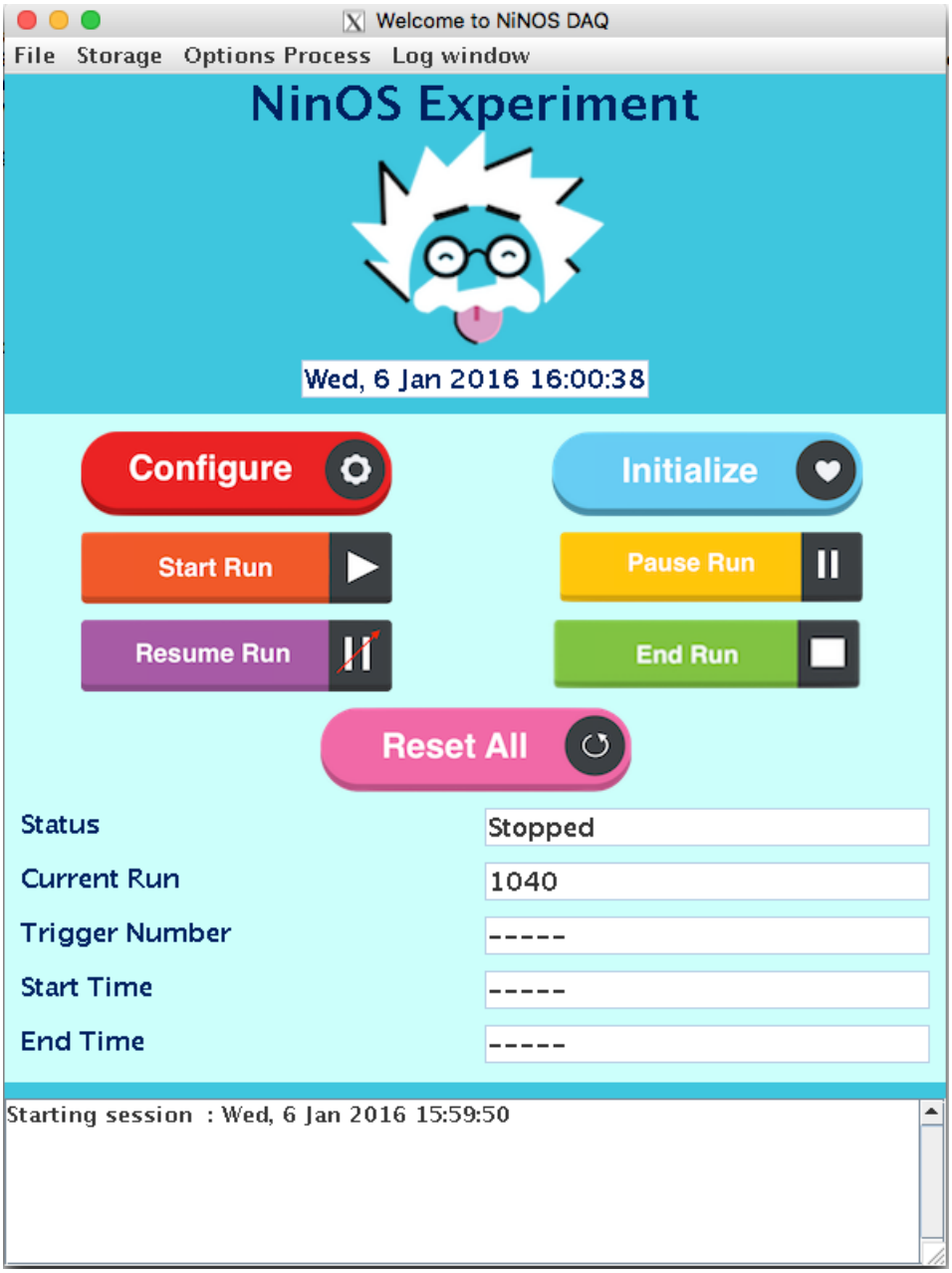

Figure 34: Graphic interface for run control and acquisition

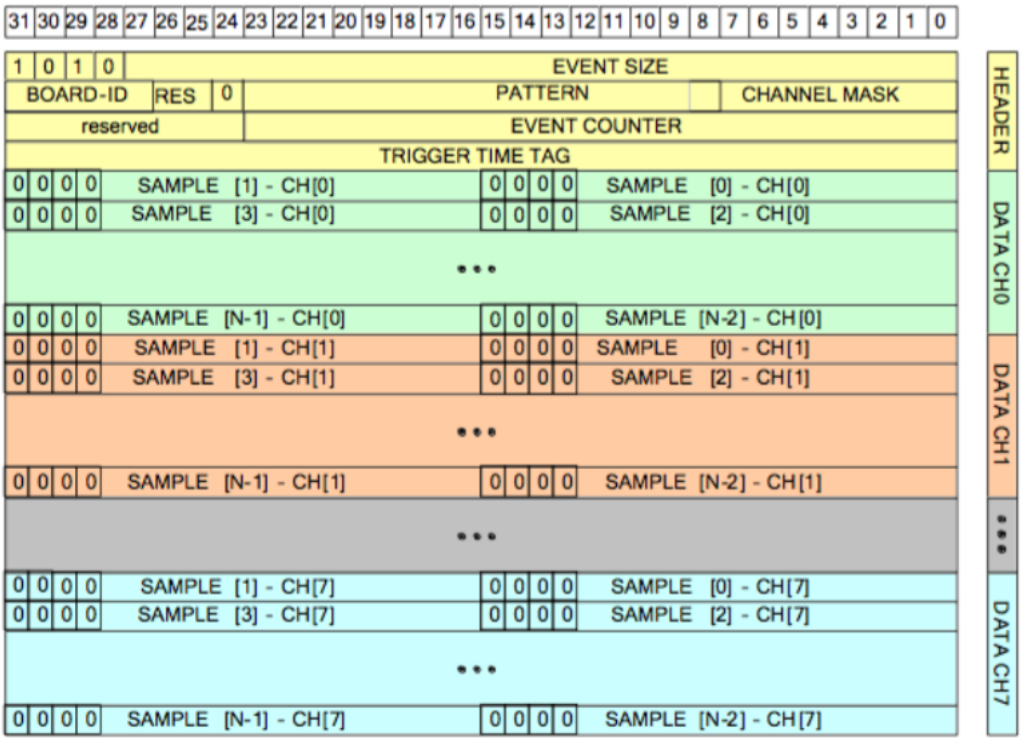

Figure 35: Standard Mode

- Word Nr 0 → event dimension
- Word Nr 1 → 1 (always)
- Word Nr 2 → magic number = 0x17081996
- Word Nr 3 → trigger number
- Word Nr 4 → 1 (always)
- Word Nr 5 → number of V1720 modules
- Word Nr 6 → 0 (always)
- Word Nr 7 → = Word Nr 0
- Word Nr 8 → not interesting
- Word Nr 9 → event number
- Word Nr 10 → 0 (always)
- Word Nr 13 → total buffer dimension (includes all modules)
- Word Nr 14 → single module buffer dimension (per event)
- Word Nr 15 → number of enabled channels
- Word Nr 16 → event counter
- Word Nr 17 → trigger time tag

The software used for decoding runs is located in the directory

/home/daq/vvecchio/Decodifica/DAQReader/src

Here there are the main code (DaqReaderMain.cpp), the class that decodes data (DaqReader.cc), the Makefile that compiles all the structure and finally some libraries (Event.o, Hit.o, HitDict.o, Event.o, EventDict.o). The most important class is that described in **DaqReader.cc** that contains two principal methods:

- int DAQReader::**ReadData**(string filename, int maxevt): it decodes data and creates a root file containing signals plots for each channel of each board.
- vector <TGraph*> DAQReader::**ReadEvent**(FILE *fp, int evtnr): it decodes data and makes the event display, so it'll be described in the next section.

As shown in the declaration of ReadData it requires as input a filename (run file's filename) and a integer, that typically is the maximum number of events in the run file. At the end ReadData method return an integer, run file's number of events decoded.
Decoding strategy is quiet simple: after local variables declaration, the method reads the input file and checks if 18 control words are that described previously. From the word nr 5 extracts the number of V1720 modules turned on, than scans data size of each modules and calculates the number of channels activated.
So the method allocates digital values of tensions looping on boards and channels and saves them in a vector named $ADC\#\_CH\#[MAX\_SAMPLES]$, where $MAX\_SAMPLES = 4096$ is the number of scans that fADC makes. Each scans lasts 4ns so the waveform's temporal window goes from the trigger time to 16.384 μs.
For every event ReadData allocates a TGraph object for each channel of each board and

saves these objects on a filename.root stored in the same run file's directory.

Data decoding code uses both standard than ROOT libraries. First of all, before compilation, one must load ROOT libraries running

. /home/root/root/bin/thisroot.sh

Now everything is ready for automatic compilation, performed by *Make* utility. Thanks to *make* command described in Makefile, it's possible to define compilers and make the implementation of ROOT classes. Starting with classes .h and .cxx the compiler makes dictionary classes, whose aim is to link our code to ROOT. To compile codes run in *src*

make clean && make all

The *make clean* command deletes all file.o, fileDict.o and file.so already compiled during previous sessions. The *make all* command turn .cxx and Dict.cxx files into .o files; then builds a shared library libEvent.so that contains standard and ROOT libraries; finally builds the executable file *Reader.bin* in the directory DAQReader.
If compilation was successful one can run the executable typing on the shell the following command from DAQReader directory:

./Reader.bin Data/run#N_frm_#.000 1000

where Data is the directory containing run files previously copied from /work/runs and 1000 is an example of maximum event number. On shell will appear the following message:

– PRESS 0 TO CREATE FILE.ROOT
– PRESS 1 TO GO TO EVENT DISPLAY

This structure it's described in the DAQReaderMain.cpp file and gives the chance to choose if use ReadData (pressing 0 and then return) or ReadEvent method (pressing 1 and the return).

5.2.3 Event Display

As mentioned in previous section the Event Display based on **ReadEvent** method it's accessible pressing 1 after running Reader.bin executable. When one choose this option a message will appear on shell:

————————WELCOME TO NiNOS EVENT DISPLAY!————————–

– PRESS 1 TO SEE ALL EVENTS
– PRESS 0 TO GO TO EVENT#

The first option allows to see event-by-event signals, the second one allows to go to a precise event number and see event's acquired signals. Both options use ReadEvent method, but they are differently managed in the main file. Most deeply, ReadEvent is ReadData's "twin": it requires as input same objects and decodes the run file as ReadData does, but returns a vector that contains TGraph objects instead of an integer value. That's the key of our Event Display. In fact, because of Reader.bin execution is performed outside

ROOT environment, it's necessary to use the TApplication class to display interactive objects, like TCanvas. TApplication class creates the ROOT Application Environment that interfaces to the windowing system eventloop, so every time we call from main code our decoding method it remembers its previous position on run file reading and allows us to see event-by-event display. Practically, a TApplication object it's declared in the main file, inside a loop that runs on events. Here main code allocates a vector of TGraph that will be defined as the output of ReadEvent method. Every vector's argument it's drown in a TCanvas (an example in Figure 36) that shows what's been scanned from fADC in each channel.

When the first TCanvas it's opened a new guide message appears on the shell. One can

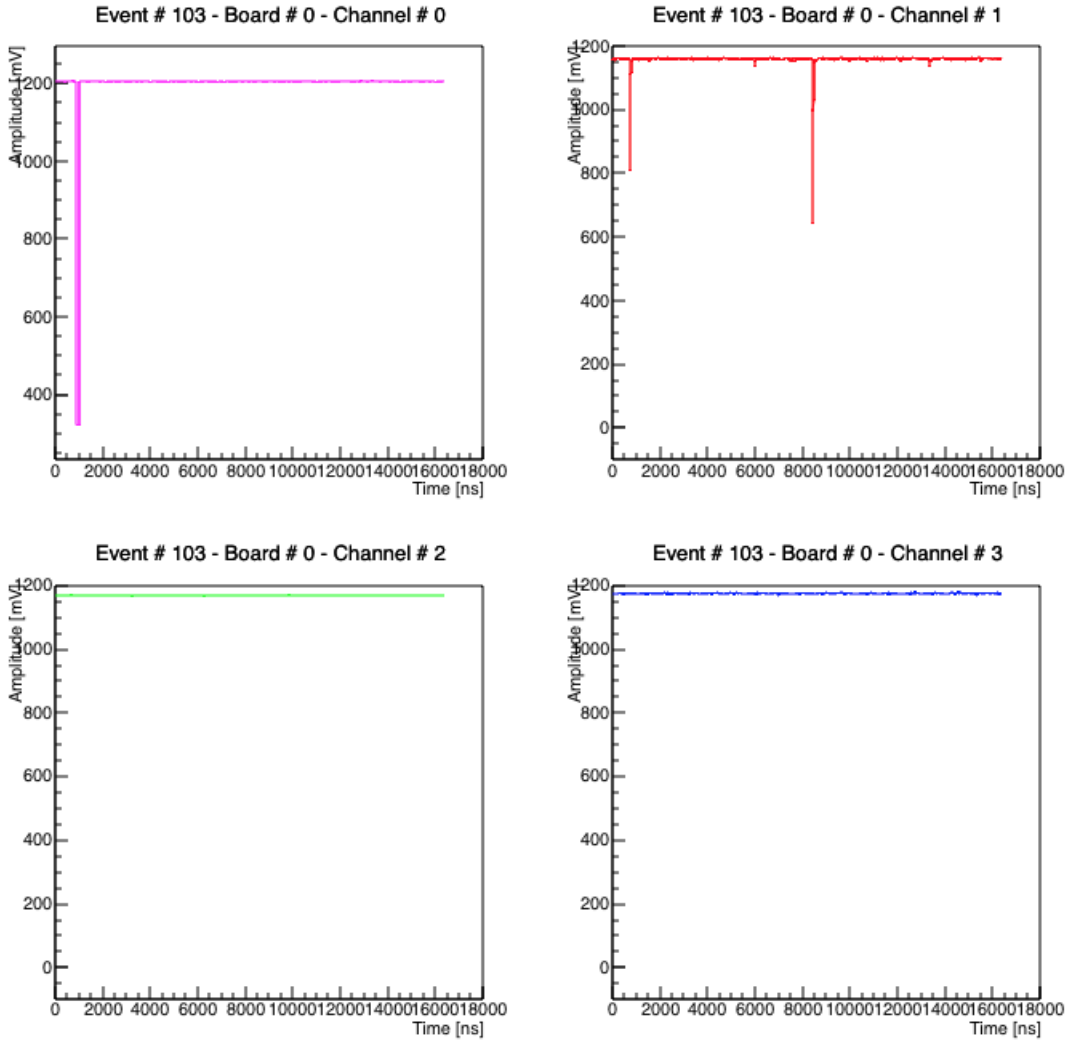

Figure 36: Example of Event Display window for a decay event: In Board # 0 - Channel # 0 trigger signal, in Board # 0 - Channel # 1 LiquidScintillator signal, in Board # 0 - Channel # 2 and 3 signals from S3 and S4, they are always zero for a decay as expected

now see the next events pressing any key, in this case TCanvas will be updated with a new TGraph's vector, or simply terminate the process typing "exit" and then return.

6 Liquid Scintillator Energy Calibration (Eleonora)

In this section we describe the detectors we use in our measurements, in particular the organic liquid scintillator EJ 321-H and the photomultipliers R 5912 ASSY and R 5912 from Hamamatsu, and the calibration process we did in order to optimize them.
Modules used are now listed and represented in Figure 37:

- Linear Fan-in Fan-out CAEN 401
- Logic Fan-in Fan-out CAEN 454
- Discriminator CAEN 417

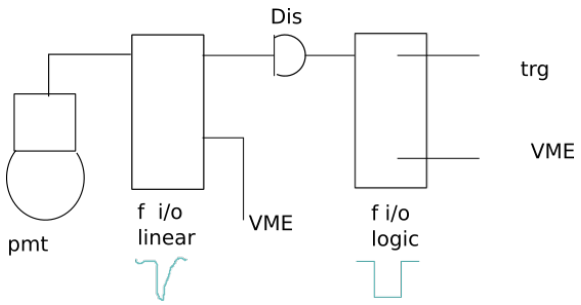

Figure 37: list of devices used

Signal from liquid scintillator enters inside of a linear fan-in fan out so that we obtain its copies, we send one inside the VME and the other to the discriminator. The logic signal coming from the discriminator enters in a logic fan in - fan out and then goes to VME and trigger.
In Figure 38 it is shown the experimental setup used: at the top we find two plastic organic scintillators S_1 and S_2 separated by a layer of lead, the liquid scintillator (LS) contained inside a barrel and the bottom two other organic scintillators named s_3 and s_4.

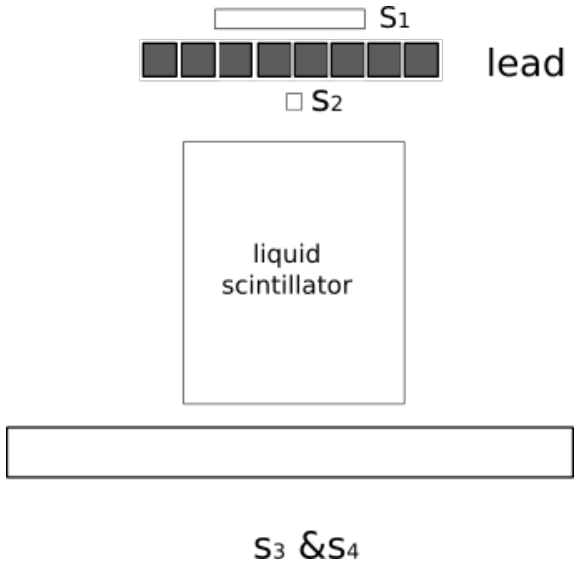

Figure 38: Experimental setup

6.1 Measurements using the photomultiplier R 5912 assy

First of all we are interested in knowing the right supply voltage and the value of the threshold we put in the discriminator. So we study the current varying the supply voltage; the results are shown in Table 8 and Fig. 39.

V_0 $[V]$	I $[\mu A]$
500	0,03
1000	0,055
1200	0,065
1300	0,07
1400	0,081
1500	0,079
1550	0,081
1600	0,084

Table 8

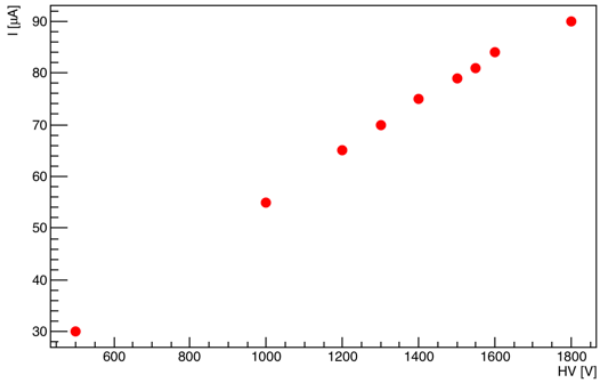

Figure 39

Current absorbed varying alimentation HV

We fix HV= 1800 V because from the data sheet we know that at this voltage we can obtain the best gain (10^7). Now we change the value of the threshold and we measure the counts and the mean value of the charge collected per event, where we define "charge" as $Q = I\Delta t/n = q/n$. We considered $\Delta t = 60s$, $I = 93\mu A$ and n is the counts. Results are shown in Figure 40 and 41 and in Table 9.

Threshold [mV]	Counts	σ_{counts}	q/n $[\mu C]$
15	43526	209	0,13
30	7973	89	0,7
40	2323	48	2,4
50	1860	43	3
100	1512	39	3,7
150	1305	36	4
170	1203	33	4,63
180	1120	33	5,1
190	1125	34	3,36
200	1104	33	5
220	584	24	6,64
250	223	15	25
266	18	4	320

Table 9

Studying the plot concerning the variation of the counts we will fix the value of the threshold in a range between [-100,-200] mV, in fact in this region we can say that the

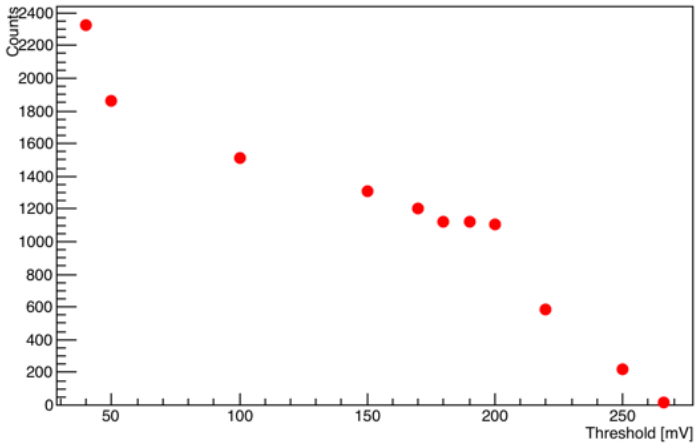

Figure 40: Counts varying the threshold

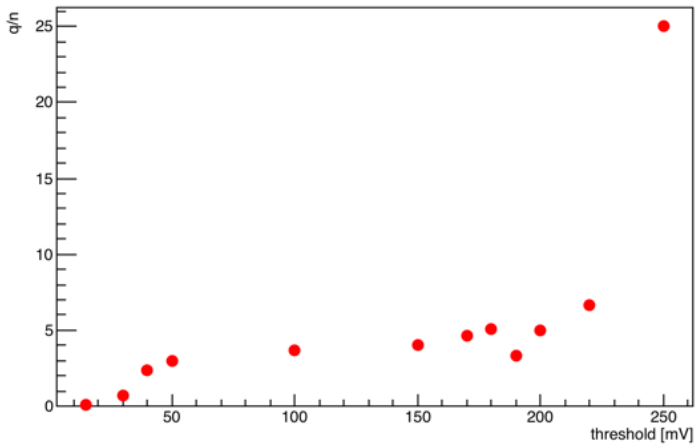

Figure 41: Charge varying the threshold

counts are unchanged if we vary the value of the threshold.
We can compare our results about charge with a theoretical prediction: we know that the number of photoelectrons produced can be calculated as:

$$n_e = \frac{dE}{dx} \times \frac{photon}{Mev} \times \eta \times Q.E. \times G \sim 100nC \tag{33}$$

Where $\eta \times Q.E. = 0.4 \times 0.5$ represents the product between the light collection efficiency and the Quantum Efficiency, G the gain, fixed at 10^7, $\frac{photon}{MeV} = 12000$ from data sheet.
An example of our signal is shown in Fig 42 .

Since we observed that the signal amplitude was lower then the expected one and the "charge" we measured was greater then the theoretical one, we try to measure, using the same strategy as before, the value of the integrated charge varying the alimentation voltage considering the coincidence between LS and S_3 and S_4. Results are shown in Table 10

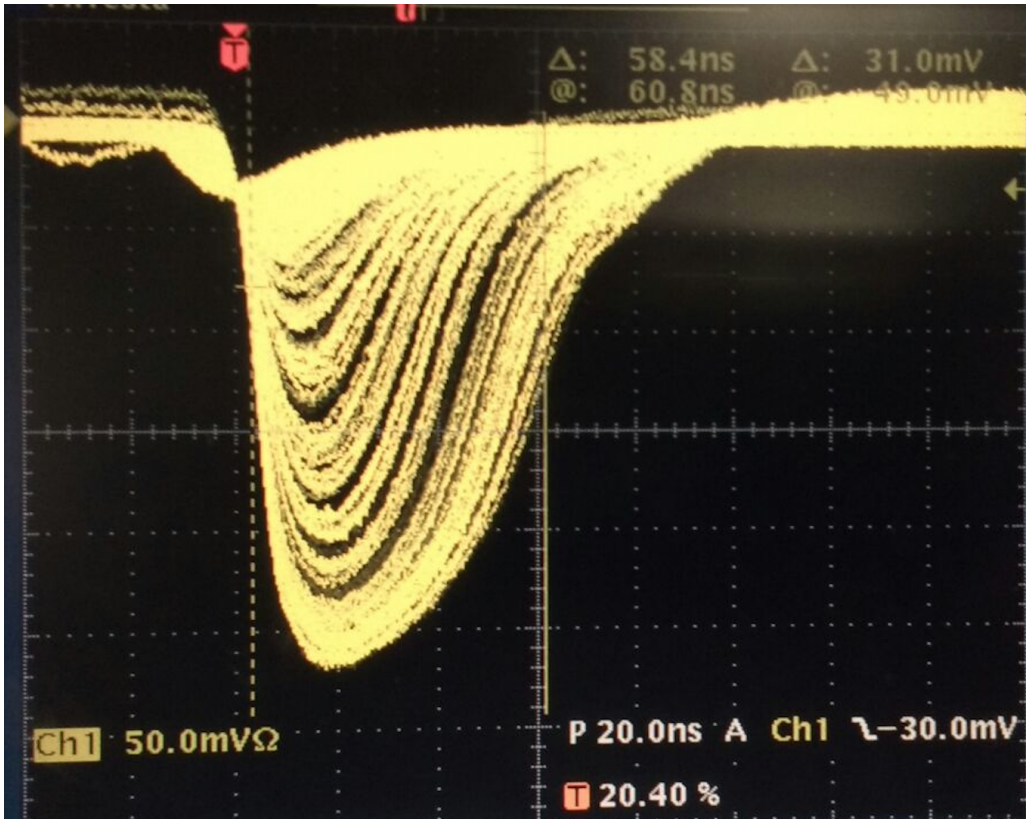

Figure 42: Signal visualized from a scope. $V_{alim} = 1800$V

HV[V]	Q[μC]	$S_3 + S_4 + LS$	$\sigma_{S_3+S_4+LS}$	$S_3 + S_4$	$\sigma_{S_3+S_4}$
1600	8	22	4	80	8
1700	7,25	26	5	73	9
1750	7,75	29	5	79	9
1800	10	18	5	63	9

Table 10

In order to decouple signal and alimentation voltage of photomultipliers used inside the liquid scintillator circuit shown in Figure 43 is used.

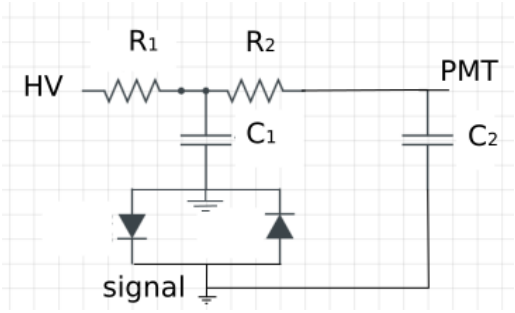

Figure 43: Sketch of the circuit which decouple PMT signal and alimentation voltage

We realized that effective alimentation voltage was lower than the provided one. It is possible to calculate the effective alimentation voltage using the following relation:

$$HV_{eff} = HV - I(R_1 + R_2) \tag{34}$$

We repeat several measurement previously taken in particular we study the variation of the counts, Q,and the current changing the alimentation voltage. All measurements are taken in 10 sec with $V_{threshold} = -150$ mv.
Results are presented in Table 11 and Figure 44, 45 and 46

HV [V]	$I_{alim}[\mu A]$	q/n $[\mu C]$	correction	HV_{eff} [V]	counts	σ_{counts}
1600	83	6	913	687	107	10
1700	88	8	968	732	186	14
1800	93	12,50	1023	777	216	15
1880	97	16,50	1067	813	237	15
1950	100	18,00	1100	850	233	15
2000	103	18,00	1133	867	258	16
2100	107	18,75	1177	923	289	17
2200	113	20,00	1243	957	1178	34
2300	117	24,00	1287	1013	2685	52
2400	122	35,55	1342	1058	5929	77
2500	127	37,50	1397	1103	9452	97

Table 11

Where correction= $I(R_1 + R_2)$ and we calulate the integrated charge as $Q = \frac{HV_{eff} \times \Delta t}{2}$.

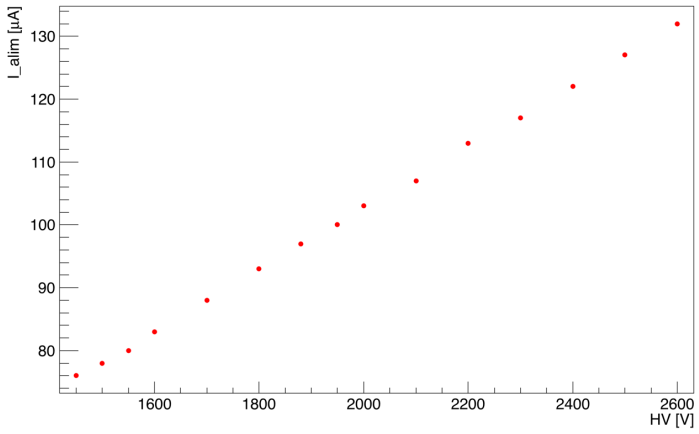

Figure 44: Variation of current with alimentation voltage

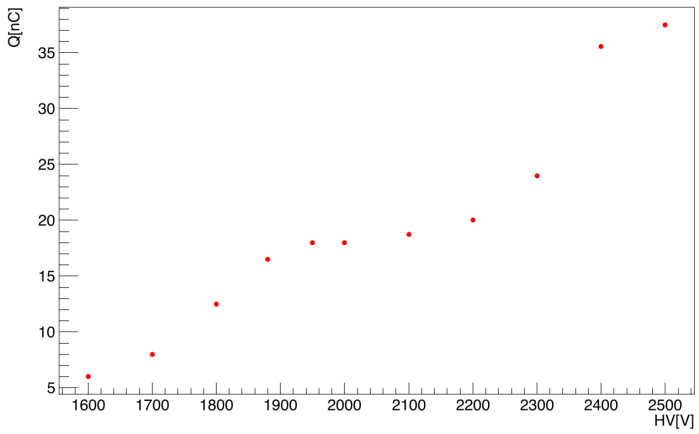

Figure 45: Variation of integrated charge with the alimentation voltage

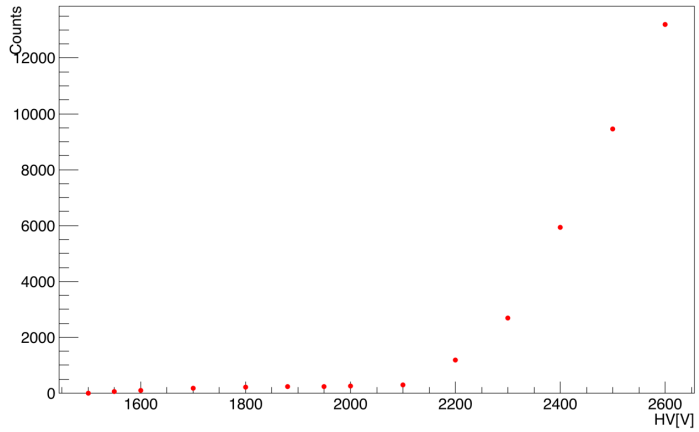

Figure 46: Variation of counts with alimentation voltage

Observing the signals we can distinguish two family as shown in Figure 47. We cannot however understand the source of these two components.

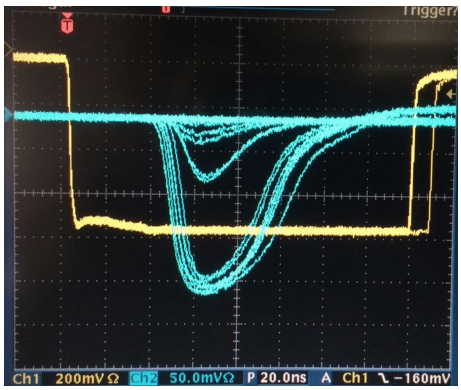

Figure 47: Two different components of the signal. $V_{alim} = 1750$ V

Since we cannot reach alimentation voltage near to the the voltage suggested in the data sheet (1600 V - 1800 V) we modify the circuit which decouple signal and alimentation voltage as shown in Figure 48

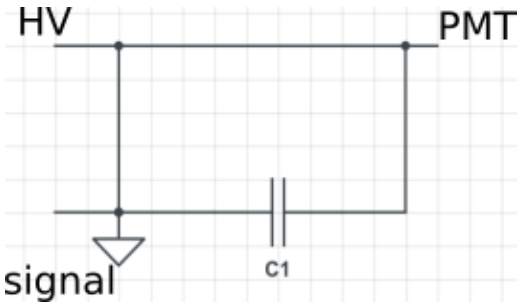

Figure 48: sketch of the circuit used to decouple signal and alimentation voltage

We fix the threshold at $V_{threshold} = -25$ mv and we measure V_{alim}, Δt and $\epsilon = \frac{counts(LS+TRG)}{counts(TRG)}$. the results of these measurements are shown in Table 12.

We can observe that signal decreases when alimentation voltage increases, moreover

HV [V]	$I_{alim}[\mu A]$	$peak[mV]$	Δt [ns]	ϵ
1250	124,5	381	58,1	0,947
1350	136,6	367	61,63	0,83
1450	145,8	259	60	0,8
1550	157,8	258	61	0,85
1650	170,2	135	60,57	1

Table 12

signal peaks are lower than 100 mV when $V_alim = 1650$ V.
Before going on with the analysis we show the signal we see on the scope in Figure 49.

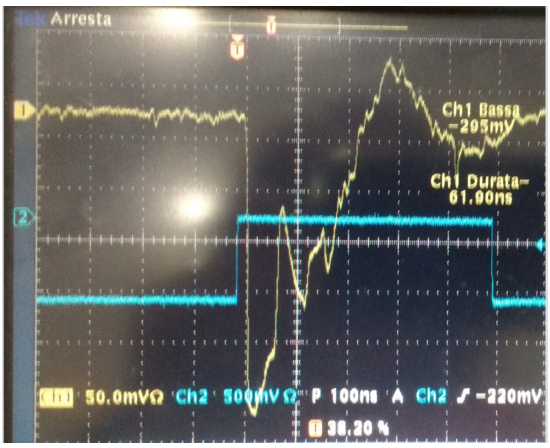

Figure 49: New configuration of PMT signal from the scope

We repeat measurements per each given value of alimentation voltage in order studying the parameters we are interested in: we consider 10 events acquired per alimentation

voltages (see Figure 50) but we also observe in the scope events which are not acquired because they are lower than the threshold we fix (see Figure 51).

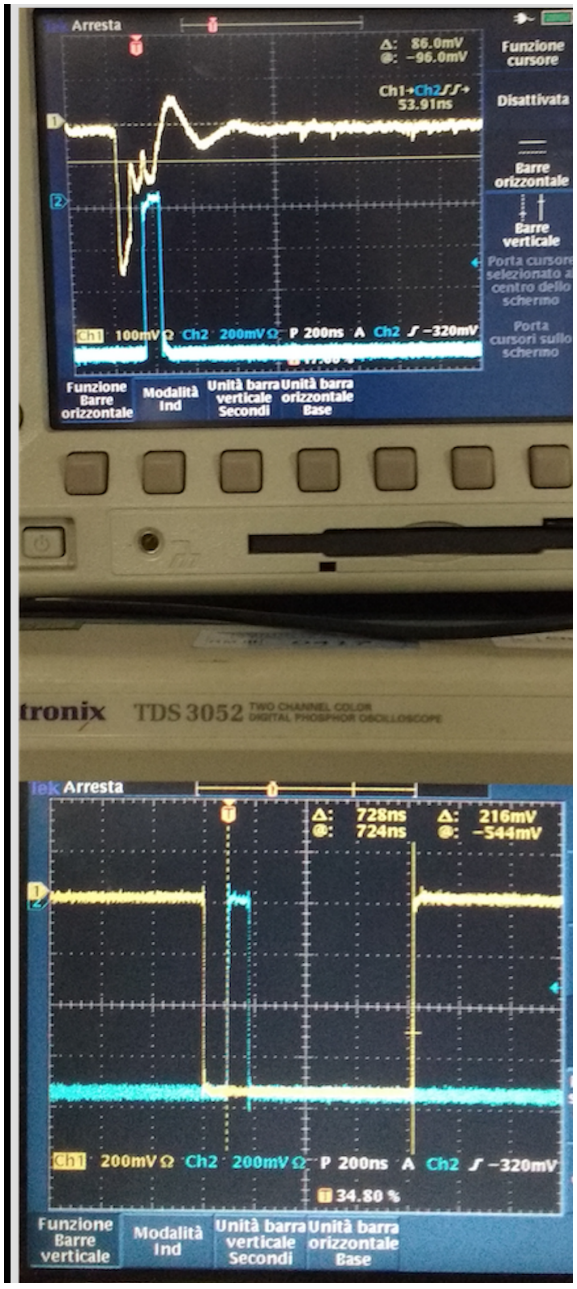

Figure 50: Example of acquired event. $V - alim = 1550$ V and $V_{threshold} = 100$ mV

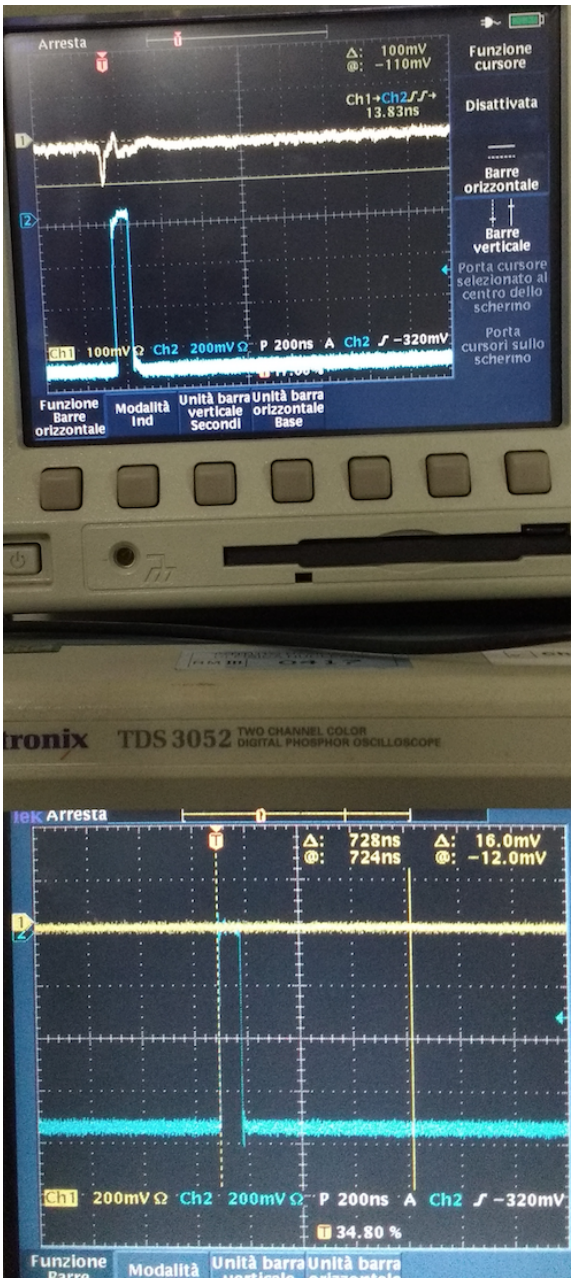

Figure 51: Example of not acquired event. $V - alim = 1550$ V and $V_{threshold} = 100$ mV

We can observe in Figure 50 that discriminator signal rise again728 ns after the signals, in fact it is present a small peak of V= 72 mV. It is possible that this phenomenon could affect the counts of LS+ TRG.

V_{peak} $[mV]$	Δt [ns]	Q[nC]
438	59,22	25,94
344	45,81	15,76
430	58,8	25,28
460	61,14	28,12
432	59,45	25,68
448	61,26	27,44
475	60,91	28,93
390	54,3	21,18
441	61,08	26,94

Table 13: $V_{alim} = 1350$ V

V_{peak} $[mV]$	Δt [ns]	Q[nC]
332	57,56	19,11
380	59,49	22,61
380	59,92	22,77
380	60,15	22,86
377	61,9	23,34
345	53,36	18,41
380	59,91	22,77
380	60,44	22,97
380	60,79	23,10
380	61,63	23,42

Table 14: $V_{alim} = 1450$ V

V_{peak} $[mV]$	Δt [ns]	Q[nC]
254	61,63	15,65
258	61,63	15,9
328	61,64	20,218
85,1	32,32	2,75
254	61,14	15,53
302	61,77	18,65
268	61,84	16,57
339	61	20,68
295	61,9	18,26

Table 15: $V_{alim} = 1550$ V

V_{peak} $[mV]$	Δt [ns]	Q[nC]
130	59,57	7,74
111	60	6,66
129	57	7,35
137	60,3	8,26
105	60,28	6,33
166	60,85	10,10
119	61,08	7,27
131	60,3	7,90
125	60,85	7,61
126	60,66	7,64
159	60,63	9,64
132	60,54	7,99

Table 16: $V_{alim} = 1650$ V

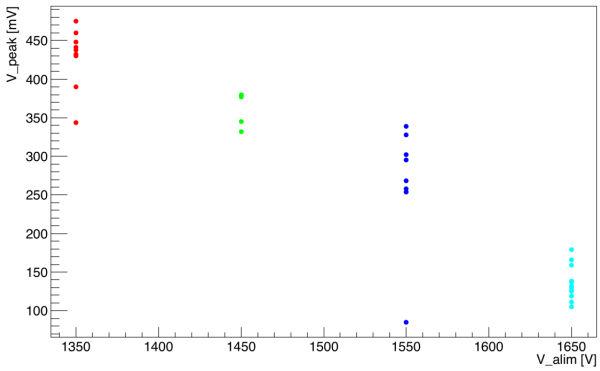

Figure 52: Variation of current with alimentation voltage

We observe in Table 13, 14, 15, 16 and in Figure 52, 53 and 54 that Δt results unchanged per different value of alimentation voltages because of internal reflections of the signal

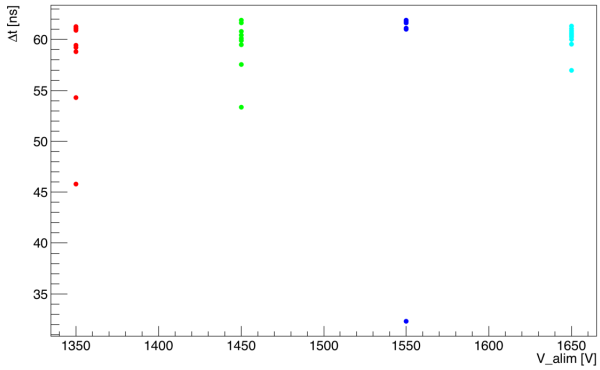

Figure 53: Variation of integrated charge with the alimentation voltage

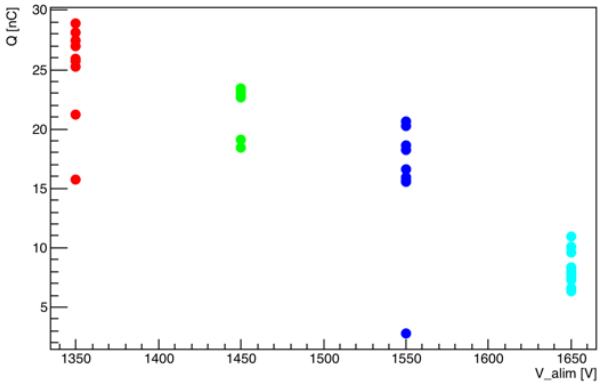

Figure 54: Variation of counts with alimentation voltage

in the cable, in fact reflections reverse the signal and what is actually shown in Figure 49 is the sum of signal and reflections. We chose $V_{alim} = 1750$ V and $V_{threshold} = 100$ mV in order to studying the value of efficiency, however we were forced to change the PMT because signals were too small and their amplitude changed considerably with the time.

6.2 Measurements with R 5912 photo multiplier

Because of the change of PMT we repeat measurements taken before in order to determine the V_{alim} and $V_{threshold}$. Results are shown in Table 17 and Figure 55, 56, 57 and 58.

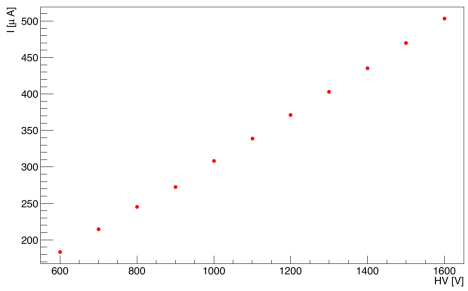

Figure 55: Variation of current with respect to the alimentation voltage

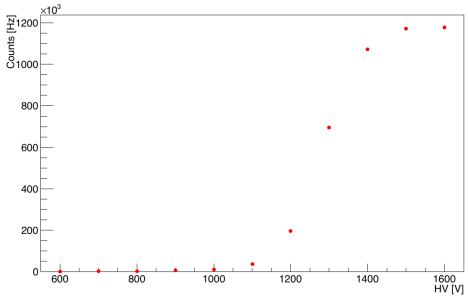

Figure 56: Variation of Counts with the alimentation voltage

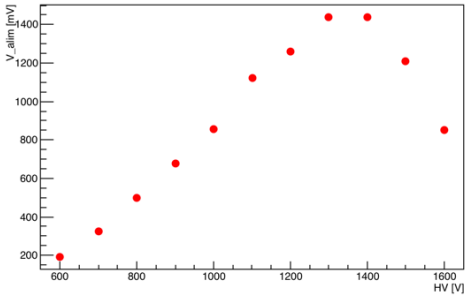

Figure 57: Variation of peak amplitude with respect to the alimentation voltage

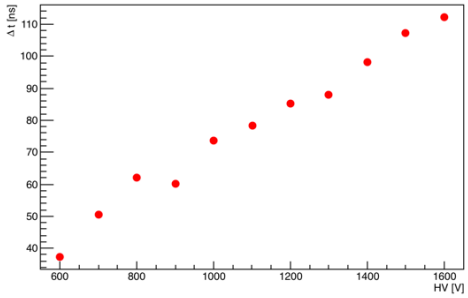

Figure 58: Variation of time width of the peak with the alimentation voltage

HV [V]	$I_{alim}[\mu A]$	Counts [Hz]	$V_{peak}[mV]$	Δt [ns]
600	183,5	36,1	190	37,2
700	214,5	1052,7	325	50,60
800	245,5	2883,5	497	61,97
900	272,2	5372,0	676	60,18
1000	308,1	9497,7	857	73,62
1100	338,7	35319,5	1120	78,23
1200	371,2	194874,5	1260	85,26
1300	402,7	694948,9	1440	87,84
1400	435,2	1072310,1	1440	98,09
1500	469,7	1171537,5	1210	107,3
1600	503,3	794338	853	112,3

Table 17

All the plot reported are almost consistent with theoretical prediction. Concering Figure 57 and 58 we can see that the value of V_{peak} decreases when V= 1400, we expected indeed that it rise linearly with the alimentation voltage, this effect is probably due to the particular way in which the PMT in built, however the product of V_{peak} and Δt increase.

As we did for the previous PMT we focus in a small range of alimentation voltage and we take some repeated measurements in order to choose the best value of alimentation

voltage. Results are shown in Table 18, 19, 20, 21 and Figure 59, 60, 61

V_{peak} $[V]$	Δt [ns]	Q[nC]
0,957	76	36,4
0,940	72	33,8
0,960	77	37,0
0,908	60	27,2
0,933	88	41,1
0,930	68	31,6
0,928	61	28,3
0,768	48	18,4

Table 18: $V_{alim} = 1000$ V

V_{peak} $[V]$	Δt [ns]	Q[nC]
1,04	68,8	35,8
1,08	79	42,7
1,1	77	42,4
1,04	66	34,3
1,07	78	41,7
1,02	60	30,6
0,560	30,5	8,5
1,09	77,6	42,3

Table 19: $V_{alim} = 1050$ V

V_{peak} $[V]$	Δt [ns]	Q[nC]
1,1	63,15	35,7
1,1	57,4	32,1
1,1	54,4	30,7
1,0	43	21,5
1,2	79,7	47,8
1,2	78,8	47,3
1,2	79,6	47,8
1,2	78,5	47,1
1,2	81	48,6

Table 20: $V_{alim} = 1100$ V

V_{peak} $[V]$	Δt [ns]	Q[nC]
1,42	83	58,9
1,43	83,6	59,8
1,38	74,5	51,4
1,2	47,8	28,7
1,28	55	35,2
1,42	77,8	55,2
1,44	84,2	60,6
1,44	84,5	60,8
1,48	84,8	62,8
1,18	43	25,4

Table 21: $V_{alim} = 1200$ V

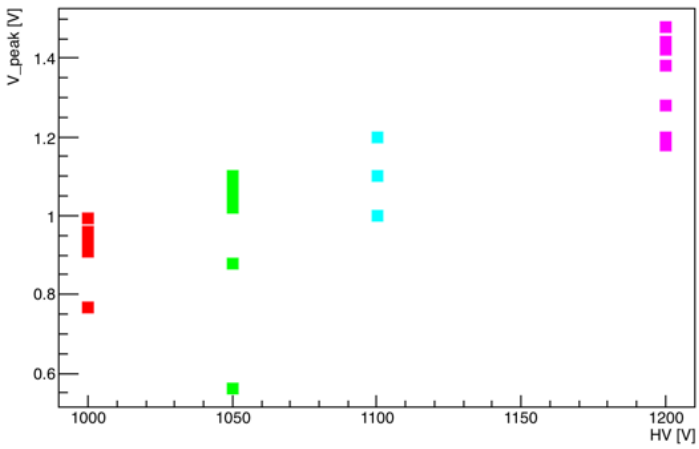

Figure 59: Variation of $V_{peak}$with the alimentation voltage

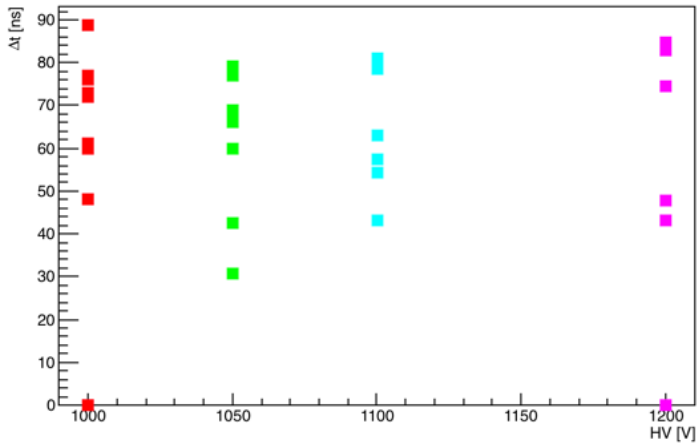

Figure 60: Variation of Δt with the alimentation voltage

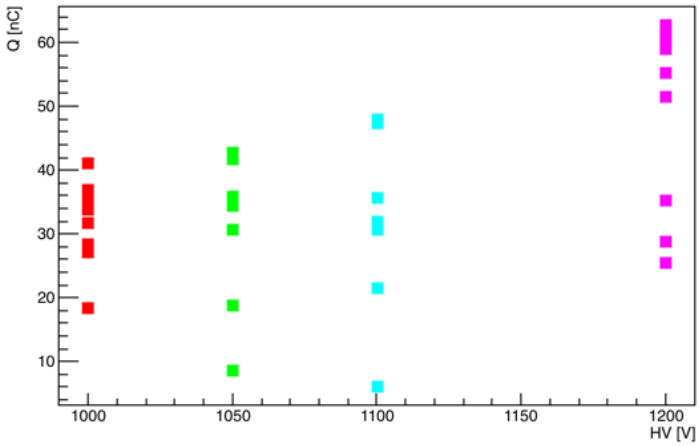

Figure 61: Variation of integrated charge with the alimentation voltage

The aim of our experiment is to measure the Michel spectrum end point in order to determine the value of neutrino mass, we choose a value of alimentation voltage equal to $V_{alim} = 1100$ V, which is in a intermediate range between low alimentation voltages and high alimentation voltages, characterized by high gain, and we fix the threshold to be small $V_{threshold} = 15$ mV, this value is estimated to be a little bit more than two times the background amplitude.

7 Data Analysis

7.1 C → eV conversion using a ^{60}Co source (Eleonora)

For this analysis we will use the run 1026, it is acquired in particular condition: in fact we introduce a γ source, in particular ^{60}Co in order to calculate the conversion factor between Coulomb and electronvolt. As shown in Figure 62 we insert inside our tank a support in alluminum for our ^{60} Co source.
In our experiment we will detect electrons; the best way to calculate the conversion factor would be used an electrons source; however we could not use it because the one we have results too old. So, even if the radiation process for photons and electrons are quite different, we were obliged to use a γ source. Obviously we expect that our conversion factor will be just an approximation and does not represent the exact value. The γ we

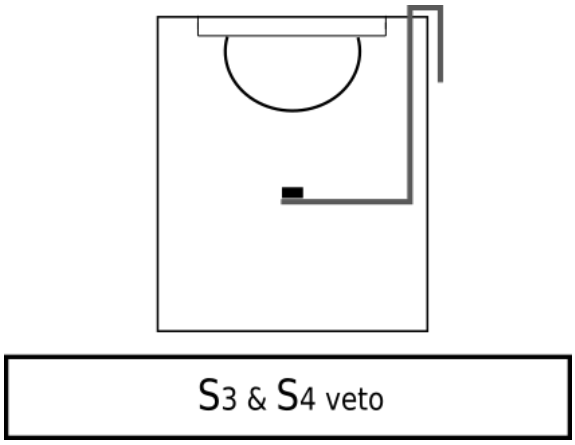

Figure 62: experimental setup of ^{60} Co acquisition

are interested in acquiring are produced via a β decay: the excited states of the daughter nuclide ^{60}Ni release their energy through γ emission to the daughter ground state. The decay process can be understood more clearly from the decay scheme in Figure 63. It can be seen that gamma emission at 1.1732 MeV is due to transitions from the excited level at 2.506 MeV to the level at 1.332 MeV following the most probable β^- emission of 0.318 MeV. Another gamma emission can be seen at 1.3325 MeV due to transitions from the excited level at 1.3325 MeV to the ground state of ^{60}Ni; in Table 22 are reported characteristics of our source.

γ decay energy	1.1732 keV 1.3325 keV
Nominal activity	4.21 kBq (01/05/03)
$T_{1/2}$	5.27 y

Table 22: ^{60} Co properties

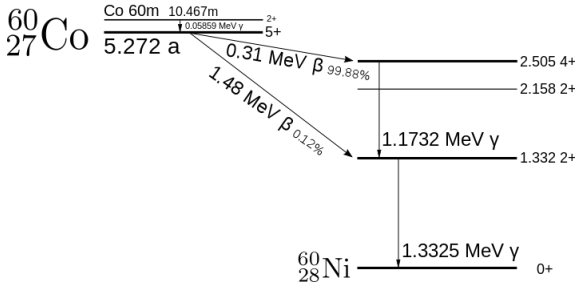

Figure 63: ^{60}Co decay scheme

In Table 23 we report some measurements which help us to decide the best supply

and threshold voltage.
In this case we define the efficiency as $\epsilon = \frac{LSrate}{(LS+\overline{S_3S_4})rate}$ in order to measure the difference

$LSrate[Hz]$	$LS + S_3S_4$ rate [Hz]	ϵ	σ_ϵ
HV=1200 V			
51004,3	50026,0	1	0,0012
51939,0	49577,4	1	0,0012
44691,9	48458,3	1	0,0011
50211,8	46799,2	1	0,0013
51236,6	46639,8	1	0,0013
HV=1100 V			
42044,4	42074,0	0,99930	0,0013
42007,2	42036,5	0,99930	0,0013
42588,4	42617,8	0,99931	0,0013
41001,0	41029,4	0,99931	0,0013
42120,7	42150,7	0,99929	0,0013
HV=1000 V			
8579,5	8593,3	0,99839	0,00278
8634,9	8648,9	0,99837	0,00277
8613,4	8627,1	0,99841	0,00278
8302,6	8317,1	0,99826	0,00283
8637,0	8651,9	0,99828	0,00277
HV=700 V			
861,2	927,7	0,928	0,008
905,8	921,5	0,983	0,008
901,6	918,0	0,982	0,008
HV=600 V			
17,8	32,3	0,55	0,03
17,3	32,3	0,54	0,03
16,8	30,9	0,54	0,03
HV=600 V, $V_{threshold}$ =5 mV			
459,1	475,0	0,967	0,012
454,8	469,5	0,969	0,012
460,6	477,0	0,965	0,012
HV=500 V, $V_{threshold}$ =3,5 mV			
15,3	30,0	0,509	0,029
15,3	29,9	0,511	0,029
14,9	29,1	0,513	0,029

Table 23: LS, LS+$\overline{S_3 \& S_4}$ rate

between LS rate and the rate of LS in coincidence with $\overline{S_3S_4}$; we are interested to study possible inefficiency of LS and which are the best supply voltage for an energy calibration. In order to consider only events produced by ^{60}Co we trigger our system with LS + $(S_3S_4)_{veto}$, that is we consider event "produced" in LS which are missed in S_3S_4. From

properties of our source we can obtain the activity of our ^{60} Co source from the relation:

$$A(t) = A_0 e^{(-\frac{t}{\tau})} \tag{35}$$

where A_0 is the activity measured in 2003, t is the time passed from the last activity measurements and $\tau = 1/\lambda = \frac{t_{1/2}}{ln2}$. From this relation we obtain that the activity should be A= 757.8 Hz. We fix LS supply voltage $V_{alim} = 600$ V and the value of threshold is $V_{threshold} = 5$mV, so that we can acquire even the smallest signal. Signals we acquired are shown inFigure 64.

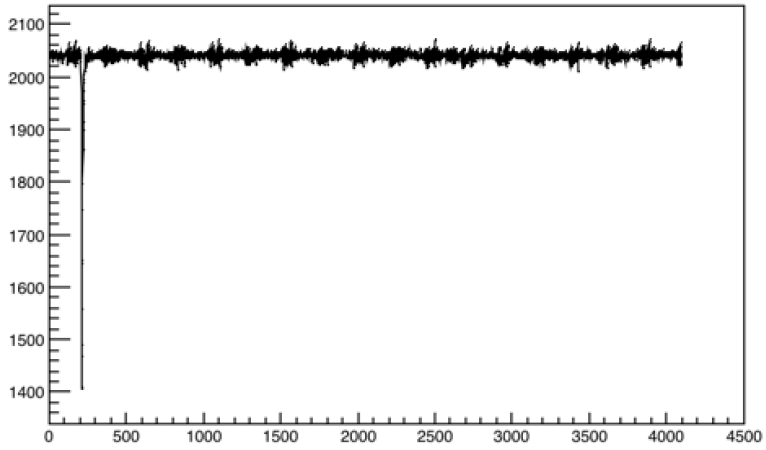

Figure 64: example of signal acquired with $\times$8.5 amplification

With a polynomial fit of 0 order we fix the value of the baseline and we obtain $p0 = 2041.85 \pm 0.070031$. Now we are ready to begin to calculate signal area in order to determine the charge collected by the PMT following the relation:

$$Q = \frac{\sum_i (\Delta V_i \times \Delta t)}{R} = \frac{\Delta t \times \sum_i \Delta V_i}{R} \tag{36}$$

where $\Delta V = \frac{(baseline - min)}{8.7}$, we are dividing by ten because we are studying signals amplified by a factor 8.7[26] in order to better analyze signal parameters we are interested in, Δt=4 ns, that is the time value of each bin and the value of the impedance is R=50 Ω. We report some distributions obtained from the data; in particular in Figure 65 we show the plot of the signal amplitude distribution and in Figure 66 we present the distribution of the time amplitude that is $\Delta t = 4 \times \Delta t_{DAQ}$ is defined as the sum of the time taken by the signal to change from 10 % of the signal height to the minimum and the time to rise from the minimum from 10% of the signal.
In Figure 65 we can see a small peak around 400 mV, it represents events coming from γ emission of our source.

[26]The value we fix in the amplification module was 10

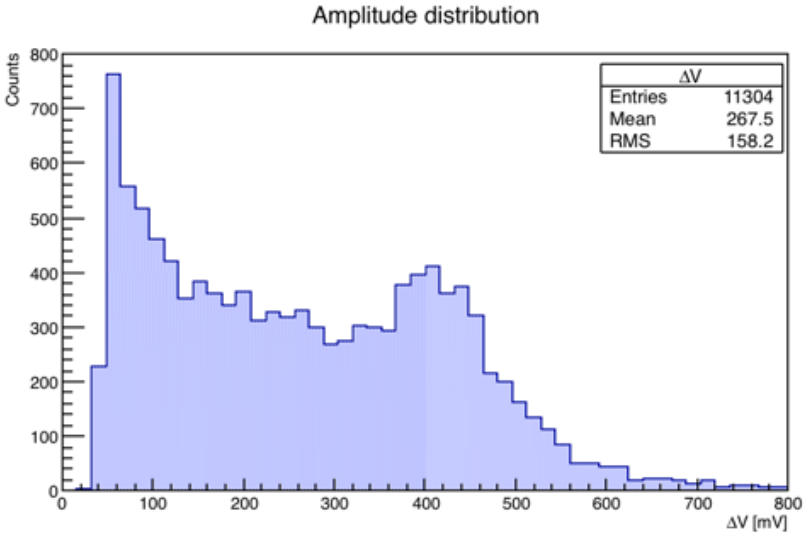

Figure 65: ΔV distribution

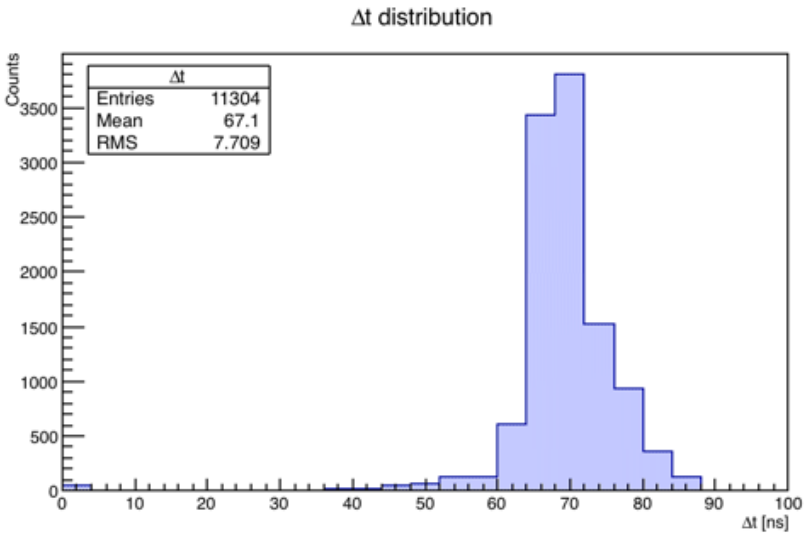

Figure 66: Δt distribution

We report now in Figure 67 the charge distribution per event. What we obtain reflexes our expectations; our signals can be represented as the sum of different functions,that is a first gaussian peaked in Q= 0.011 nC, a decreasing exponential, which describes the continuous of the electrons produced by the ^{60}Co source, and another gaussian with a peak in Q= 0.052 nC represent the two γ emission of the source, because of our energy resolution we cannot resolve the two γ emission peaks. We are interested in estimate the value of charge which correspond to the energies of γ emission, so we fit the difference between the exponential function and our gaussian, in order to consider only events containing γ and determine all the three parameter of the gaussian we are studying. Results are reported in Figure 68 and Tabular 24

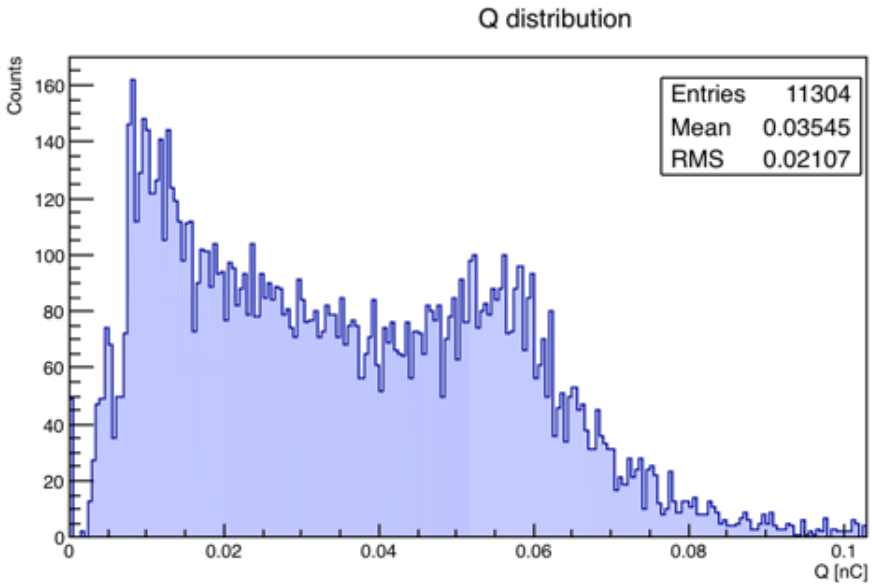

Figure 67: Charge distribution

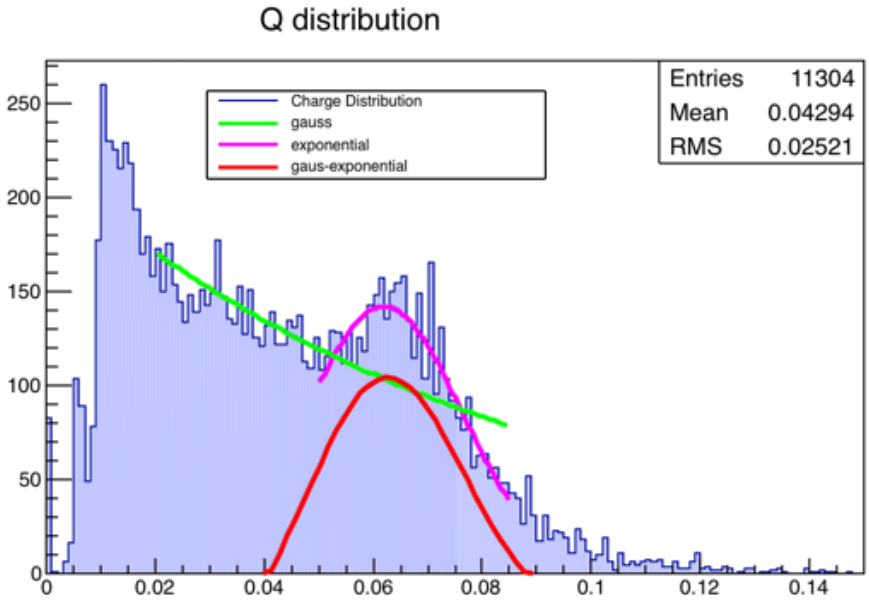

Figure 68: γ gaussian distribution

Amplitude	50.50 ± 0.012
Mean	0.0618 ± 0.0001
σ	0.017 ± 0.002

Table 24: Parameters of theγ signal gaussian

In Figure 68 we see plotted the charge distribution (blue area), the fit of the exponential

component (green line), the fit of the γ emission gaussian (pink line) and the fit of the difference of gaussian and the exponential components (red line).
We can now calculate the conversion factor C; considering that we cannot distinguish the two peaks we consider the mean valuethat is $E_{mean} = 1.25MeV$; we obtain our result from the expression:

$$0.062nC = 1.25MeV \rightarrow C_{^{60}Co} = (20.22 \pm 5.89)\, MeV/nC \tag{37}$$

Considering the σ of the gaussian to be the uncertainty on charge we calculate the uncertainty on the conversion factor from the propagation of uncertainty rule.

7.2 LS Calibration With Passing Muons(Cristina)

The cosmic rays that arrive at Earth's surface are mainly muons; At the see level we know them with a mean momentum of $\approx 3GeV/c$. In our case, a charged particle going through the scintillating block will loose part of its kinetic energy by ionization and atomic excitation of the solvent molecules.

7.2.1 Liquid Scintillator Calibration: Introduction

Ls calibration is done using runs of *passing events*. The RUNs' we use to do the analysis are summarised in the following table 25

RUN #	Acquisition Period	V_{LS}(V)	starting time ending time
1019	$07/12/15 - 09/12/15$	1100	13 : 54 : 47 9 : 49 : 12
1045	$09/01/16 - 08/01/16$	1100	18 : 17 : 07 11 : 28 : 52

Table 25: run list

7.2.2 Muons Energy Loss

The detection of nuclear particles depends on the fact that, directly or indirectly, they transfer energy to the medium they are going through via ionisation or excitation of the costituent atoms. The process of ionisation loss, which is dominant when the energy involved is not ultrahigh, is very well described by the *Bethe-Bloch* formula, plus two correction terms: the density effect and the shell effect. This formula can be used for muons as well as for electrons because $m_\mu >> m_e$ and because of the fact that muons energy loss is supposed to be less than the total energy.

$$^{27}\frac{dE}{dx} = 2\pi N_A r_e^2 m_e c^2 \rho \frac{Z}{A}\frac{z^2}{\beta^2}[\ln \frac{2m_e c^2 \gamma^2 \beta^2 W_{max}}{I^2} - 2\beta^2 - \delta - 2\frac{C}{Z}] \tag{38}$$

with
$2\pi N_A r_e^2 m_e c^2 = 0.1535 MeV cm^2/g$
which is a scale factor.

- $r_e = 2.817x10^{-13}cm$ is the classical electron radius;
- $m_e^2 c^2 = 0.51099MeV$ is the electron $mass \cdot c^2$;
- $N_A = 6.022x10^{23}mol^{-1}$ is the Avogadro's number;
- $I^2 = I_0 Z$ is the mean excitation potential (where I_0 refers to Hidrogen $\approx 12Mev$;
- Z atomic number of absorbing material;
- A atomic weight of absorbing material;
- ρ density of absorbing material;

[27] William R.Leo Techniques for Nuclear and Particle Physics Experiments

- z charge of incident particle in units of e;
- $\beta = \frac{v}{c}$;
- $\gamma = \frac{1}{\sqrt{(1-\beta^2)}}$ is the Lorentz factor;
- δ is a density correction;
- C is a shell correction;
- $W_{max} \simeq 2m_e c^2 \beta\gamma^2$ is the maximum energy transfer in a single collision;

The behaviour of the stoppig power $-\frac{dE}{dx}$ over muons kinetic energy is shown in fig. 69

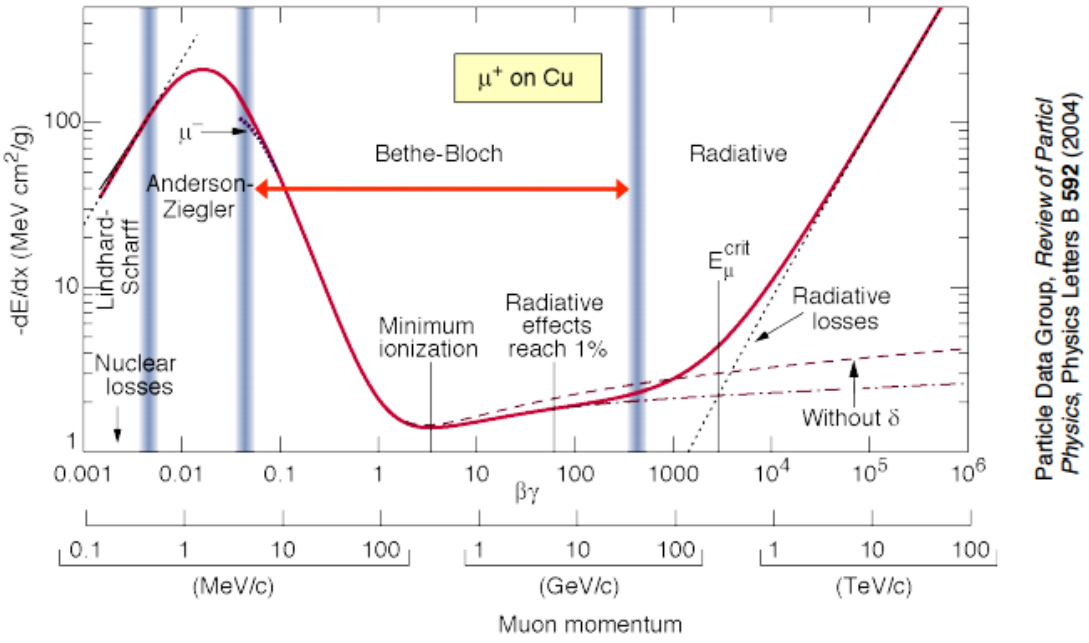

Figure 69: Stopping power for muons as a function of the momentum p. Solid curves indicate the total stopping power

So we cleared that a charged particle arrives into the liquid scintillator and loses part of its energy and this process is described by the formula above 38. Its energy, though is not perfectly known and it can be considered to be a MIP particle. Since the attention is focused on muons, for our analysis we have to calculate the energy loss of a MIP muon inside LS. From fig. 69[28] we can assume that the minimum of ionisation peak for muons in the $\frac{dE}{dx}$ distribution is close to

$$\frac{dE}{dx} = E^{\mu}_{MIP} = 2\frac{MeVcm^2}{g} \tag{39}$$

Consequently to the fact we have to do with muons, their energy loss insiede LS is

$$\Delta E = \rho \cdot \Delta l \cdot \frac{dE}{dx} \tag{40}$$

[28]PDG 2014

where :

Δl= 33 cm; $\rho = 0.86 \frac{g}{cm^3}$ $\frac{dE}{dx} = E_{MIP} = 2MeV \frac{cm^2}{g}$

where we can consider ΔE without statistical error because of the MIP assumption. The choice of $\frac{dE}{dx}$ has been taken from fig. 69 looking at the minimum ionisation point. The density of the material has been taken from the data sheet of LS's organic liquid which belongs to EJ-321 series which can see from table 1 in Section 2. Therefore the energy loss inside LS is given by the equation 40 and it results to be $\Delta E \approx 56.76 MeV$. These are the elements we used for the *calibration of LS* and in addition to those, the ΔQ that is the mean value of the charge distribution computed through the analysis of the RUNs' we mentioned above and calculating the area through a C++ program. In fact in order to get the PM readout and to convert this into the energy we have to find the gain factor G_{LS} of LS, and this will give us the conversion factor from Q(nC) to E(MeV). G_{LS} is defined by the equation below:

$$G_{LS} = \frac{\Delta E}{\Delta Q} = \frac{\frac{dE}{dx} \cdot \rho \cdot l}{\Delta Q} \tag{41}$$

Now let's see how to determine ΔQ.

7.2.3 Charge Distribution

The program of analysis deals with the analysis of a single event, and then the main program takes care of running what we set for all the other events of the RUN.
We report the signal received from which we start our analysis from:

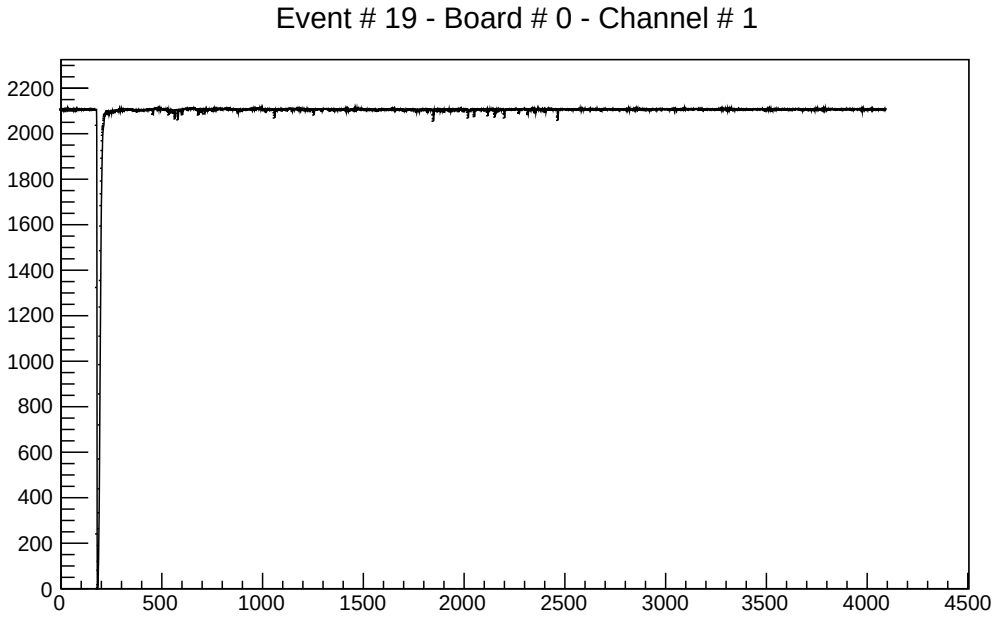

Figure 70: Ls signal received from the DAQ from RUN 1019

where Channel 1 is exactly the flash ADC's channel in which the liquid scintillator' signal went in. Watching at the signal, our first step was to determine the *baseline*, i.e the

starting point line, and we did that, as an avarage of the first 100 bins.
Then we found the *peak* value, which is the minimum of the signal, $ADC00\_CH1[uu]$. To calculate the area of the signal we have to understand in which range we need to integrate and to do so, we found the inizial time t_{in}, which means the first value of the $ADC00\_CH1[uu]$ different from the baseline, so that we make sure we are inside the signal's area to evaluate, and at the same time we find the final time,t_{fin}, in which the signal during the face lift, has still not reach the baseline value back yet. Then we integrated in that range and considering that the output impedance of the PM's is 50Ω, if we divide our equation for it, we find the charge distribution in *nC* function of time:

$$\Delta Q = \frac{4ns \cdot 0.5 \frac{mV}{DAQ} \cdot (baseline - ADC00\_CH1[min])}{50\Omega} \tag{42}$$

Where the $\Delta t = 4ns$ is the amplitude of a single bin, and $(baseline - ADC00\_CH1[min]) * 0.5$ is the value of the minimum which has to be multiplied for 0.5, which is the *ADC conversion factor*. Once we have done this we can fill the histogram, regarding the *Charge Distribution*.
We have to add a note, saying that once we complete our program and we filled the histogram we could clearly see confirmed a few suspects we had in looking at the 1019 RUN. The Data in fact were mainly saturated,as we can see in fig. 70, which stopped us from doing a complete and right analysis. Once we ascertain this, we had to acquire few other data in order to be able to complete our work; to make sure that the following data taken were not going to be saturated we have attenuated the LS'signal. We show a signal result of the latest RUN 1045 below

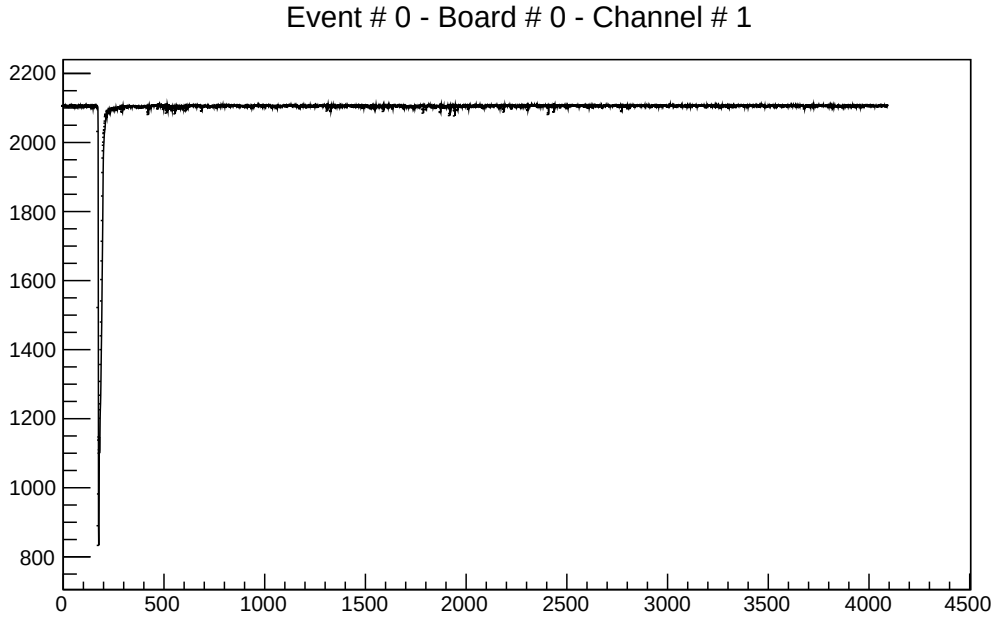

Figure 71: Ls signal received from the DAQ from RUN 1045

And we plot the result of the Charge Distribution Histogram , followed with the same one fitted :

As we easily see the new acquisition RUN was more successful, and starting from this, all our analysis has been done on this RUN. We'll plot below the histogram of the

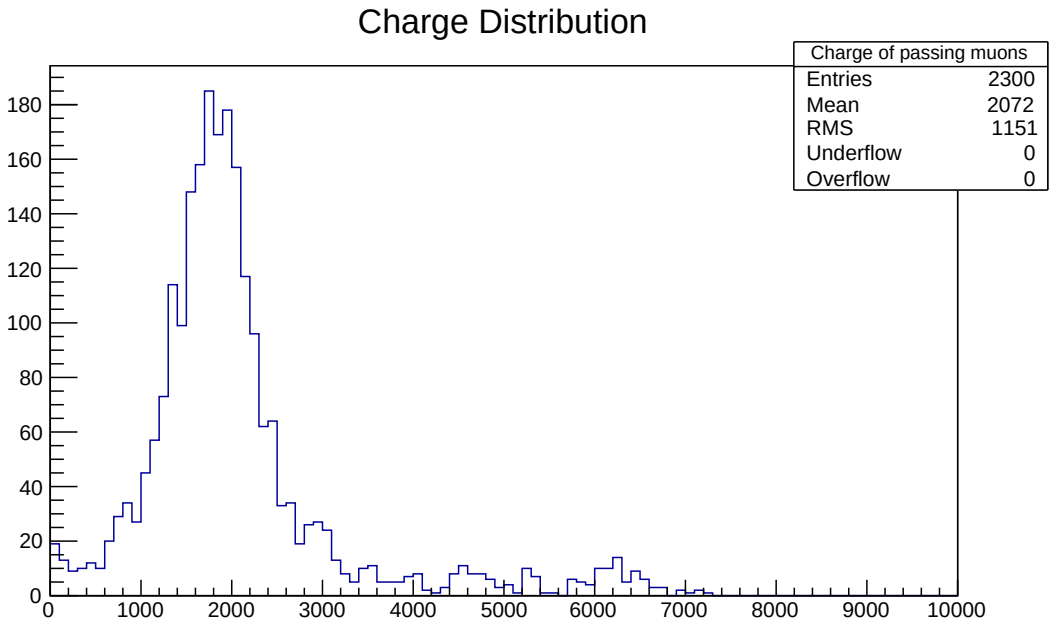

Figure 72: Ls signal received from the DAQ from RUN 1045

Charge Distribution we have obtained, with the relative FIT executed on it, applying as a fit function the sum of three gaussians.

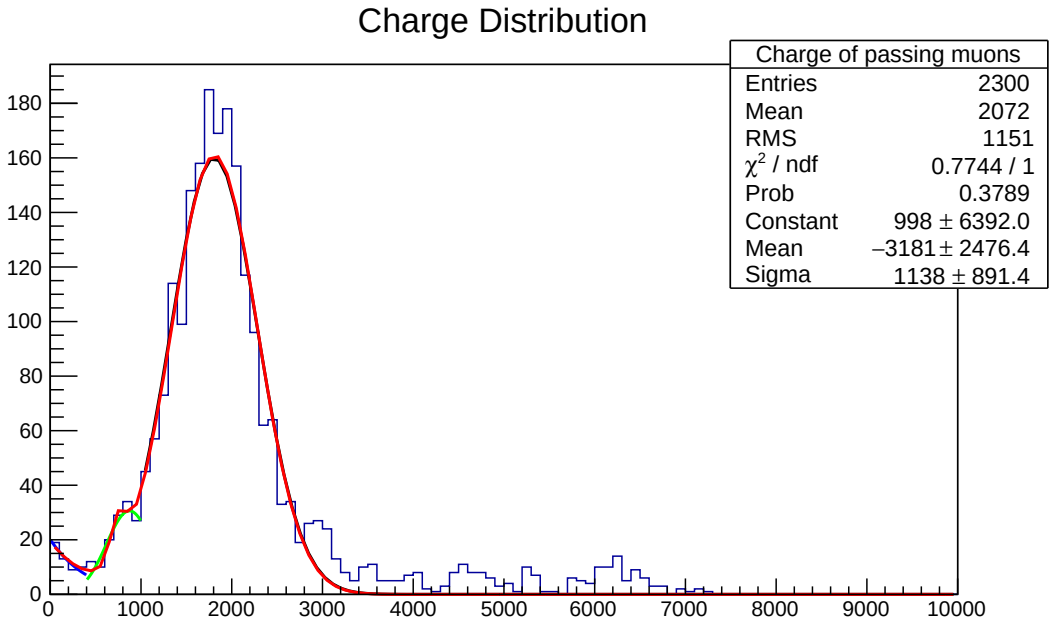

Figure 73: Histogram of the Charge Distribution inside LS

Now what we have to consider is that we don't know precisely how many photoelectrons are produced inside the photomultiplier by a MIP muon, so we picked the third

gaussian fit mean value and its error, graph is reported in fig 73

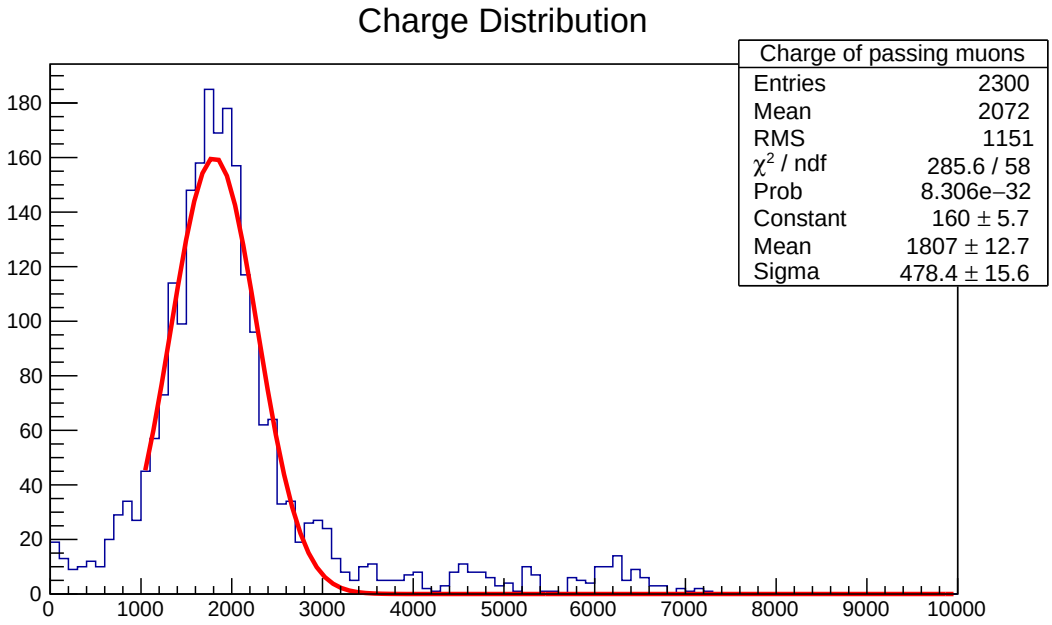

Figure 74: Histogram of the Charge Distribution inside LS

As we can see from the FIT's results the mean value of this distribution is $(1.81 \cdot 10^3 \pm 12) pC$ and $\sigma = 478.4$. Now this value needs to be compared with the theoretical value of ΔE. So we did

$$1.80nC = 56.76MeV \Longrightarrow 1nC = (31.5 \pm 3.8)MeV \tag{43}$$

where $\sigma_{G_{LS}}$ is obtained thanks to the propagation of uncertainty considering the unknowing uncertainty on the ΔE

7.3 Mean Lifetime Measurement (Valentina)

As introduced in the theoretical section about muon physics, muon mean lifetime is the most precise way to estimate G_F.
Thanks to temporal informations given by our experimental setup, we are able to perform this measure. Muon mean lifetime has been extracted from a set of data acquired in trigger decay mode. Details of data set are described in the following list:

- 18728 events
- acquired in $\approx$ 370 hours
- divided in 16 different run files

When muons pass *trigger decay requirements* they release energy on the LS and make the DAQ starts the acquisition.
Because of lead layers, it's reasonable to assume stopped muons that, in DAQ 16.384μs time window, have a 99.94% of probability to decay. So what we see in a decay event are two different peaks which separation in time is $\Delta t = t_1 - t_0$. We define t_0 the time relative to the half-height of first peak signal (*muon candidate*) and t_1 the time in which the second peak (*electron candidate*) has its minimum value (Figure 75).
The first step to select a good decay event it's to require almost two peaks on the LS

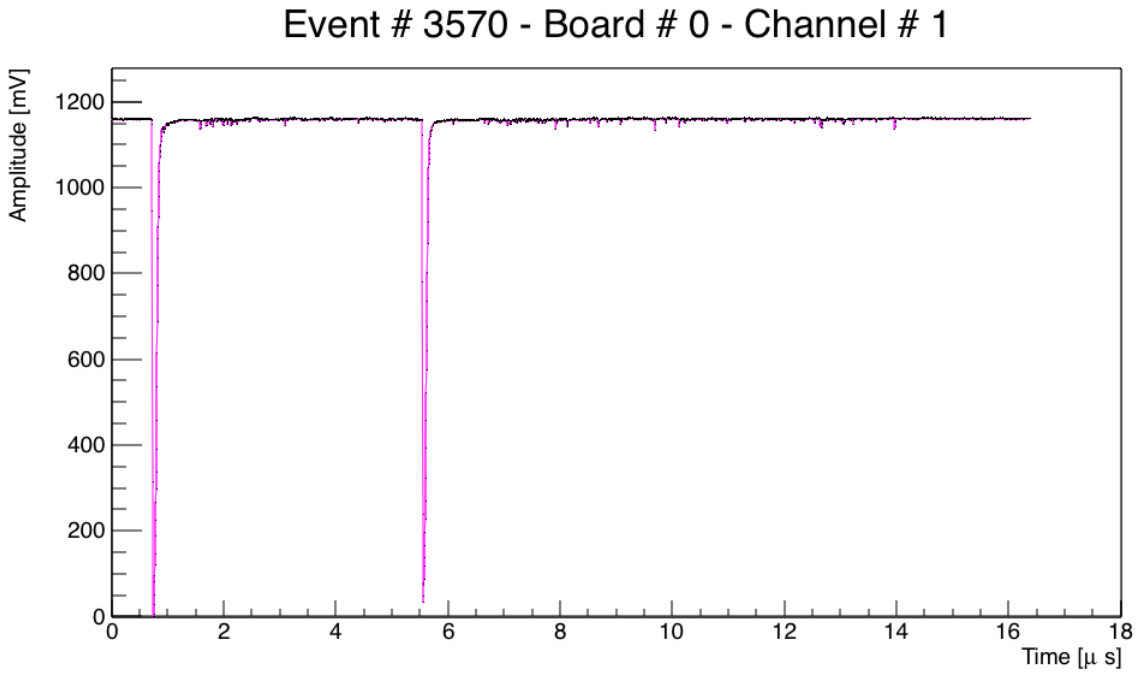

Figure 75: Decay Event: muon candidate has $t_0 \approx 0.7\mu s$, electron candidate $t_1 \approx 5.5\mu s$

output. Indeed, for several reasons, most of events have only one peaks on signal from LS. These could be due to:

- Geometric acceptance: electron from the muon decay can be emitted the from edge of LS tank, so they go outside the detector.

- Detector's inefficiency

In addition, there are a few events with a number of peak greater than 2. They could be related to little showers due to interactions in lead layers.
To find the first peak we scan the signal in the region $(0 - 0.9)\mu s$ and check for the minimum value in voltage. The second peak is the smallest voltage value in the remaining time window. Signal amplitude is calculated as the difference between the baseline and the minimum signal value. The baseline is evaluated as the mean voltage value of first $0.32\mu s$.
As first attempt to define different peaks we require that the first peak amplitude must be greater than 40mV and the second one greater than 20mV: only the 65.25% of total data set pass these selections. In Figure 76 Δt histogram is shown.
What we expected is an exponential decrease in function of time, as explained in theo-

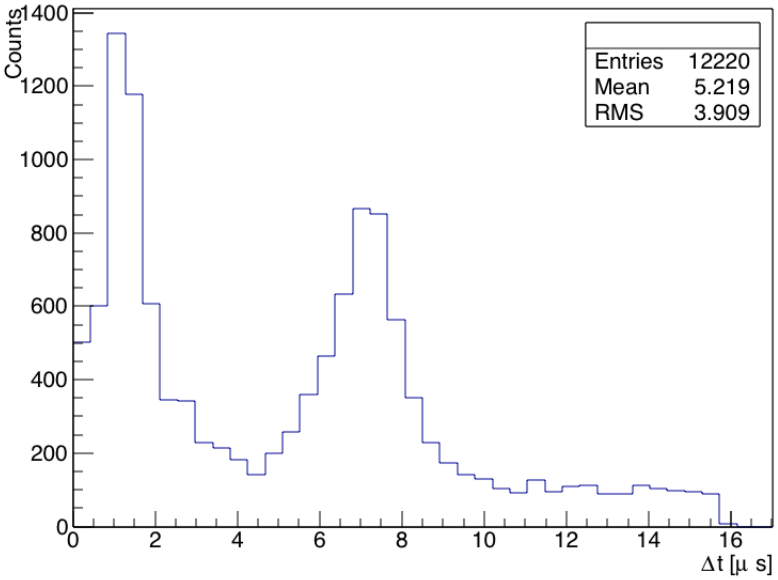

Figure 76: Number of decay in function on time

retical section about muon decay. These effects around $8\mu s$ and $2\mu s$ have a dependence from second peak amplitude shown in Figure 77. They are probably due to the decay of radioactive impurities that may be present in the photocathode and have an energy around 1200-1400 KeV Figure 78. We can easily remove these backgrounds setting higher threshold on electron candidate signal amplitude, for example above 60mV.
The final thresholds (40 mV first peak and 75 mV second peak) has been found checking for the highest χ^2/NDF probability from fitting. Selected events are the 10.13% of total dataset. Fitting function sums exponential decay expression to a uniform contribute coming from background effects. It's reasonable to assume $\tau_{\mu^+} = \tau_{\mu^-}$ because of the low Z value of LS nucleus.

$$N(t) = p_0 e^{-\Delta t/p_1} + p_2 \tag{44}$$

Fit results are shown in Figure 79.

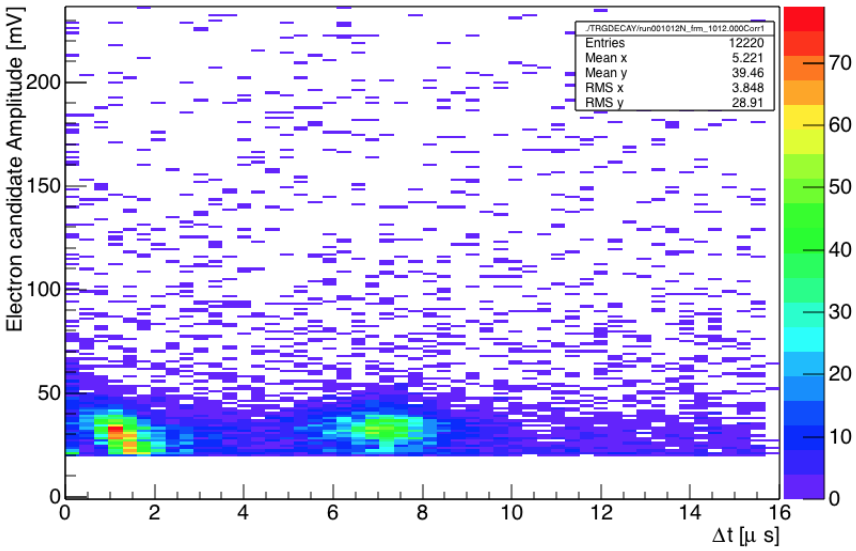

Figure 77: Correlation electron candidate peak vs decay time

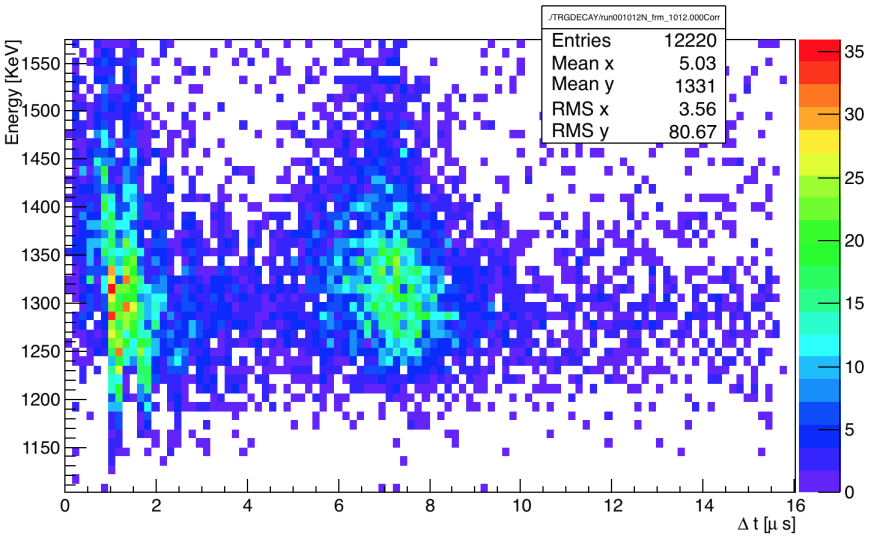

Figure 78: Correlation electron candidate energy vs decay time

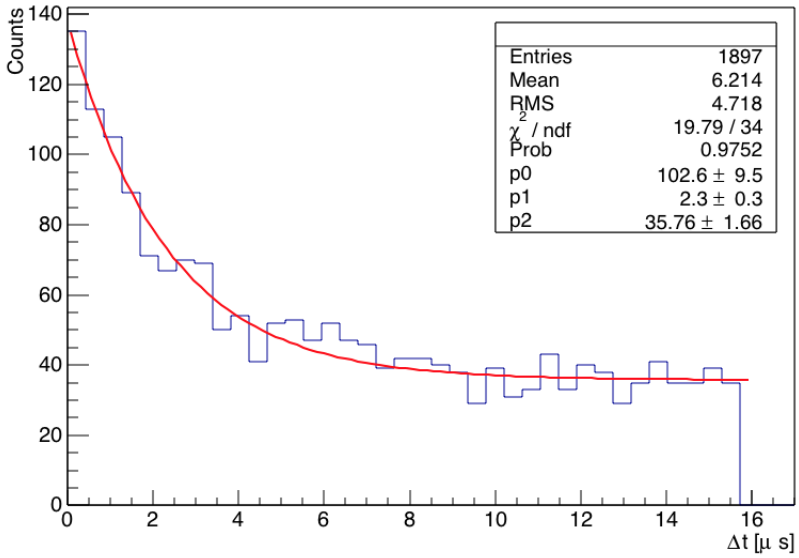

Figure 79: Decay distribution: full data set

Mean lifetime resulting value (Table 26) is compatible with the most precise measurement reported in PDG 2014 volume. This measurement has a $\chi^2/NDF = 19.7889/34$ that corresponds to a p-value of 0.9752. As result, measured mean lifetime of muon has a confidence level of 2.5σ.
From our measurement we estimated the G_F constant (Table 26) using the following expression, explained in theoretical section about muon:

$$G_F/(\hbar c)^3 = \sqrt{\frac{\hbar}{\tau_\mu}\frac{192\pi^3}{(m_\mu c^2)^5}} \tag{45}$$

Using tabled value from PDG [29] for m_μ, $\hbar c$ and $\hbar$ we found a value compatible with expectation, whose uncertainty has been evaluated with error propagation formula, considering only the biggest contribute due to our mean lifetime measurement (≈ 13 %).

Table 26: Results: full data set

	Expected	Measured
$\tau_\mu =$	$2.1969811 \pm 0.0000022\ \mu s$	$2.29985 \pm 0.312931\ \mu s$
$G_F/(\hbar c)^3 =$	$1.1663787(6)x10^{-5} GeV^{-2}$	$(1.13749 \pm 0.594601)x10^{-5} GeV^{-2}$

At the end we selected a set of events to make a more precise measure of muon mean

[29] $m_\mu = 105.6583715 \pm 0.0000035 MeV/c^2$, $\hbar c = 197.3269718(44) MeV\ fm$, $\hbar = 6.58211928(15)x10^{-22}\ MeV\ s$

lifetime. In facts, during the last two acquisitions a blackout occurred, so events in these run files are probably not so good as we expected. Alimentation and coincidence unit thresholds could change because of sudden blackouts; as result background events in this condition could be greater than signal ones.
This hypothesis is confirmed looking at the following results. Using a threshold of 32mV on the first peak and 65.5 mV on the second one, we selected the 10.15% of 14952 events. Decay distribution is shown in Figure 80 and results are shown in Table 27. Fit χ^2/NDF probability is 0.9825, corresponding to 2.58σ, and signal/background ratio is 2.64 instead of 2.87 value of the entire data set.
Both mean lifetime and G_F are closer to expected values and the χ^2/NDF probability is bigger, so we conclude that this last measurement is the best value obtained from our experimental setup.

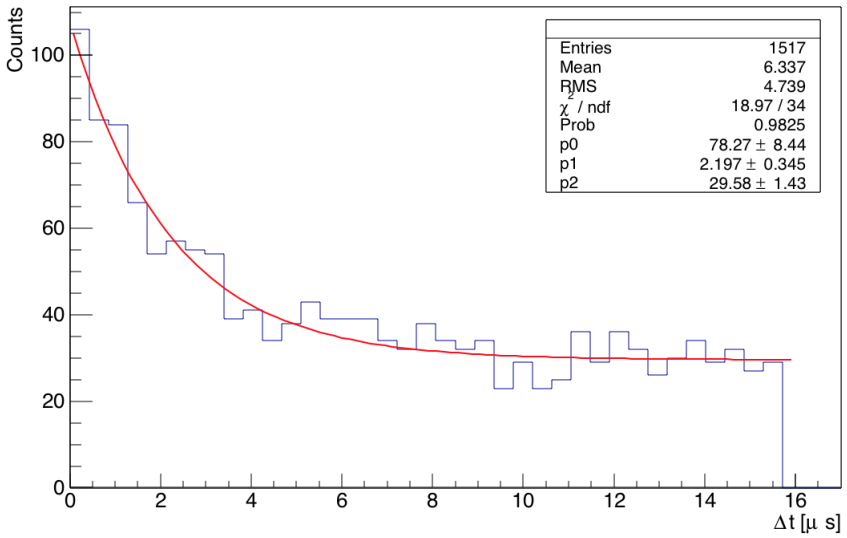

Figure 80: Decay distribution: partial data set

Table 27: Results: partial data set

	Expected	Measured
$\tau_\mu =$	$2.1969811 \pm 0.0000022\ \mu s$	$2.19747 \pm 0.344609\ \mu s$
$G_F/(\hbar c)^3 =$	$1.1663787(6)x10^{-5}GeV^{-2}$	$(1.16369 \pm 0.701086)x10^{-5}GeV^{-2}$

7.4 Estimation of the Neutrino mass (Giulio)

As explained in section 1.2 a Muon can decay in an electron plus two neutrinos, with a branching ratio close to 1. The kinematics of the process

$$\mu^{\pm} \rightarrow e^{\pm} \overset{(-)}{\nu_{\mu}} \overset{(-)}{\nu_{e}}$$

is described by the Michel spectrum (4), which represents the electron energy. If we consider massless neutrinos, the enpoint of the Michel spectrum will be precisely at $E = m_{\mu}/2$. Since we know that neutrinos have mass, we could estimate it by observing a deviation in the electron spectrum from such maximum energy value.

In order to obtain a sample made of decay events, some selections were applied to data. Following the indications in figure 75 we look for a muon signal in the first 0.9 μs of the time window, requiring a signal greater than 100mV. The signal amplitude was evaluated as the difference between the signal peak and the baseline, which consists of the mean value of the signal in the first 640 ns. The electron signature was searched in the remaining time window, requiring a signal greater than 100mV. The amplitude distribution of the muon and electron candidates is shown in figure 81, with the applied cuts.
The reported cuts selected about the 7.3% of the total number of events. Electrons generally exhibit a bad penetrating power, so we can assume that they lose all their energy inside the scintillator, after their production. At energies up to $\sim 50\ MeV$, the dominant energy loss mechanism for electrons is the ionization. We can thus estimate the electron energy by integrating all the charge collected by the PMT. Once the electron signal is identified, we can calculate the total charge by summing over all bins where the signal develops:

$$Q = \sum_{i=\xi_1}^{\xi_2} \Delta V_i \cdot \Delta t_i \tag{46}$$

where the edges ξ_1 and ξ_2 are defined as the bin where the amplitude goes under the 10% of the peak amplitude. In figure 82 and in figure 83 are reported, respectively, an example of an electron signal from data and the total charge distribution for selected events.
The tipical Michel profile can be observed in figure 83 for $Q \gtrsim 0.7nC$, while background events dominate the lower charge part of the distribution. Figure 83 represents the electron spectrum, in terms of the total charge collected inside the liquid scintillator. In order to fit the distribution, a modified expression of the Michel spectrum was used. Assuming unpolarized muons ($P_{\mu} = 0$) and integrating over all the zenital angles, equation (4) can be written as

$$\frac{d\Gamma}{dE} = \frac{1}{E_{max}} \times \left(\frac{G_F^2\ m_{\mu}^3}{96\pi^3} \right) \times \left(3 - 2\ \frac{E}{E_{max}} \right) \times \frac{E^2}{E_{max}^2} \tag{47}$$

where E_{max} represents the enpoint of the spectrum. To obtain a fit function for the charge distribution, we assume a linear correlation $E = const \times Q$ between the electron energy and the total collected charge; the spectrum expressed in terms of the charge thus becomes:

$$\frac{dN}{dQ} = k_1 \times \left(\frac{G_F^2\ m_{\mu}^3}{96\pi^3} \right) \times \left(3 - 2\ \frac{Q}{Q_{max}} \right) \times \frac{Q^2}{Q_{max}^3} \equiv\ f_M(Q) \tag{48}$$

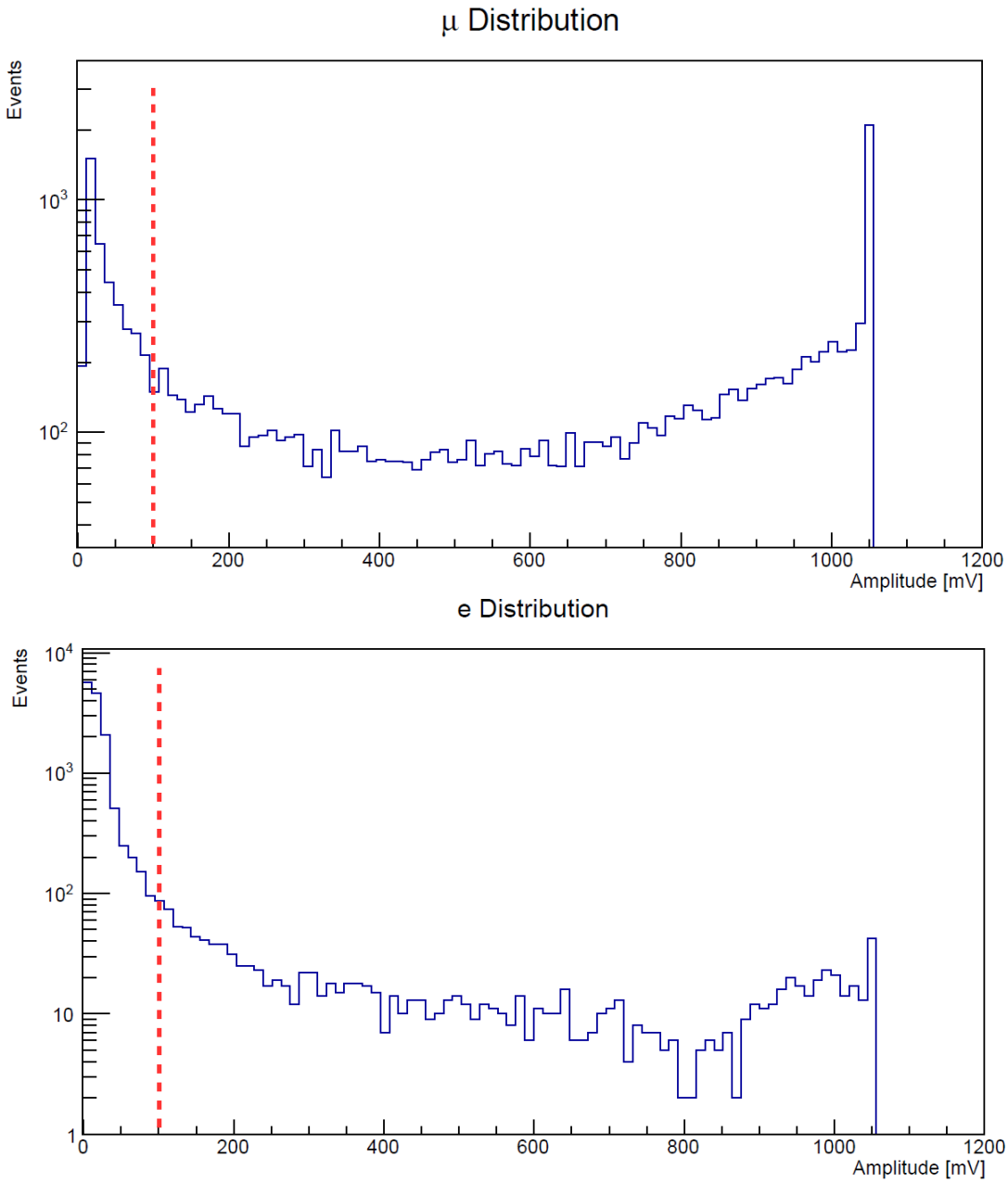

Figure 81: *Signal amplitude distribution for muon and electron candidates, with the corresponding cut.*

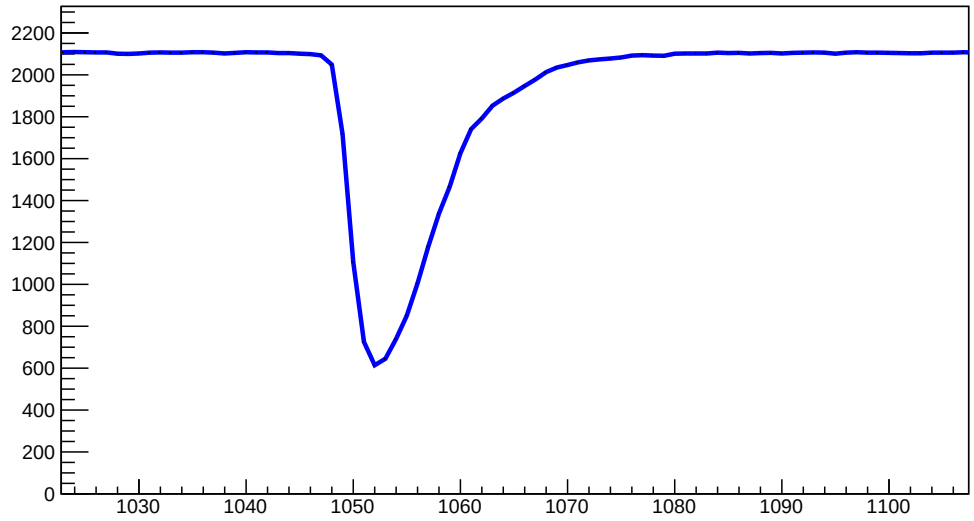

Figure 82: *Example of an electron signal, with DAQ bins on the X and Y axis; each bin on the X axis corresponds to 4 ns, while each bin on the Y axis corresponds to 0.5 mV.*

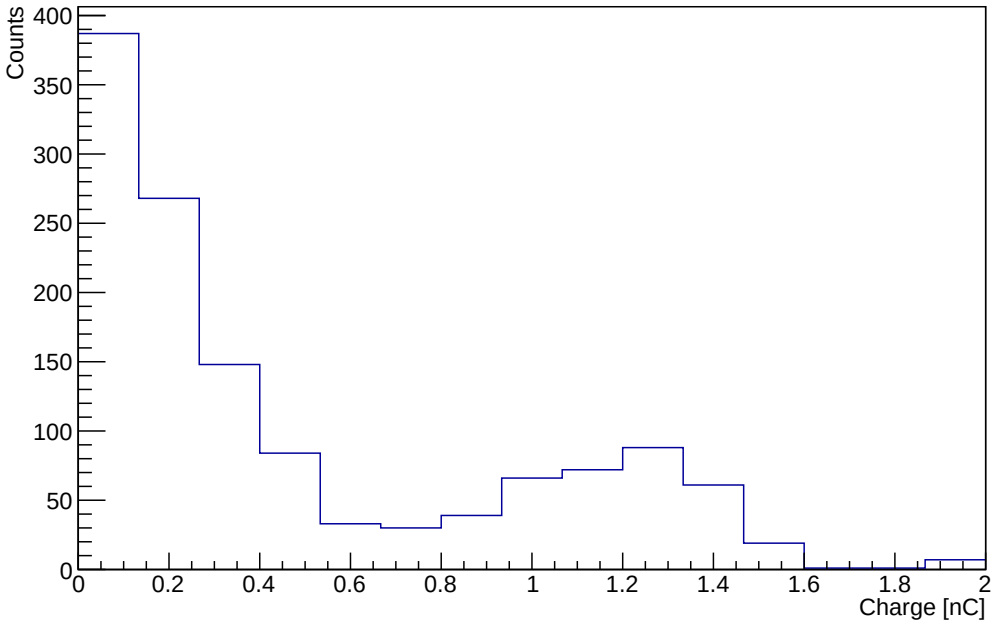

Figure 83: *Total charge distribution for selected events.*

As explained above, to fit the charge distribution we must consider background events, for which we can assume an exponential distribution, with its maximum at $Q = 0$:

$$f_{bkg}(Q) \equiv k_2 \, e^{-k_3 \cdot Q}$$

The final fit function is thus the sum of the two contributes:

$$F_{fit}(Q) = f_M(Q) + f_{bkg}(Q) \tag{49}$$

The fit is reported in figure 84:

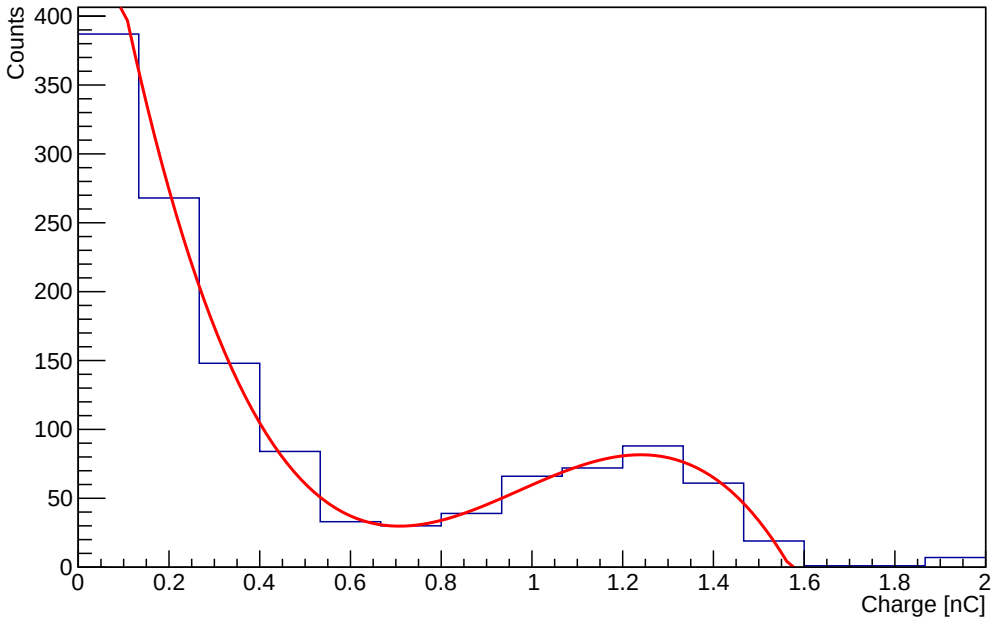

Figure 84: *Total charge distribution with the final fit function.*

The value of Q_{max} was set as a parameter of the fit. The result is $Q_{max} = (1.487 \pm 0.031)\ nC$, with a χ^2/ndf value of 0.65 and a p-value of 0.69, corresponding to a confidence level of 2.95σ.

Using the conversion factor evaluated in (43), we obtain the maximum energy:

$$E_{max} = (46.8 \pm 5.7)\ MeV^{30} \tag{50}$$

The maximum energy in the Michel spectrum assuming massless neutrinos corresponds to (section 1.2):

[30] errors evaluated as $\frac{\sigma_{Emax}}{E_{max}} = \sqrt{\left(\frac{\sigma_{Qmax}}{Q_{max}}\right)^2 + \left(\frac{\sigma_{c.factor}}{c.factor}\right)^2}$

$$E_{max}^{exp} = \frac{m_\mu^2 + m_e^2}{2m_\mu^2} = 52.828\ MeV^{31} \tag{51}$$

The difference between these two energies can be interpreted as the rest mass of a neutrino:

$$\Delta E = E_{max}^{exp} - E_{max} = (5.99 \pm 0.73)\ MeV \tag{52}$$

Current experiments set the upper limit of the neutrino mass at $\mathcal{O}(eV)$, unconsistent with our result. A neutrino of a few MeV mass found in this work can be explained in terms of a lack of events near the enpoint of the spectrum, because of the low statistics. Our result can be declared as an upper limit on the neutrino mass, since it is given by our experimental enpoint. The final measurement can be expressed as

$$m_\nu < (5.99 \pm 0.73)\ MeV \tag{53}$$

[31] PDG 2014 - the result is presented without error because it is many orders of magnitude smaller than in our measurement

Conclusions

- Concerning the calibration of the liquid scintillator at first we used a R 5912 ASSY photomultipliers from Hamamatsu. In order to decouple signal and alimentation voltage we introduced a circuit which attenuated excessively our signals. We understood that the problem concerned the value of the resistors we used, so we tried to modify this circuit but our signal appeared distorted because of internal reflections. We decided to change the phomultiplier and we used an R5912 from Hamamatsu . As a result of the calibration we fix the supply voltage to be $V_{alim} = 1100V$ with a threshold $V_{threshold} = -15mV$.
  With a dedicate run we try to calculate the conversion factor from nC to MeV: for this kind of experiment it is appropriate to use an electron source, however we were obliged to use a γ source and we used ^{60}Co. We studied the charge distribution in order to discriminate the two γ emission peak but considering that our experimental set-up was not suitable to this this kind of measure we could not distinguish them. We expected that such a result represent just an approximation, even because the physical processes concerning the interaction between photons and scintillating material are different from the ones between electrons and scintillator.
  Conversion factor we measure is $C = 20.22 \pm 5.89$.
- Thanks to the trigger system the coincidence between all the scintillation detectors has been made and the charge collected inside the PMT is estimated to be (1.81 ± 0.12)nC at 1100V. The conversion factor from Q to E has been determined and is $(31.5 \pm 3.8) Mev/nC$.
- We can estimate the compatibility between the two different conversion factors from the relation:
$$\frac{|C_\mu - C_{^{60}Co}|}{\sqrt{\sigma^2_{C_\mu} + \sigma^2_{C_{^{60}Co}}}} = 1.6\sigma$$
- The DAQ System, made of four electronic boards, has been confirmed to work properly. The time window of the first fADC was set to $16\mu s$, in order to look for a muon decay, then the second fADC was de-activated. To avoid signal overlaps, a veto system was implemented, by means of two Dual Timer modules.
  Run Control interface has been modified and some new routines have been developed in the class that decode run files. In addition we implemented an Event Display to see offline event-by-event acquired signals. Thanks to this algorithm, it's also possible to see signals referred to a specific run file event number. An interesting plan for the future could be the development of online Event Display.
- From trigger decay acquisitions we extrapolated muon mean lifetime; our measurement $\tau_{mu} = 2.19 \pm 0.34\ \mu s$ completely agrees with the expected value, with a confidence level of 2.58σ.
  This result has been evaluated from a partial data set; in fact, we had some problems on last acquisitions, due to a sudden energy blackout. As results, these runs have a greater number of background events, so the lifetime value $\tau_\mu = 2.30 \pm 0.31\ \mu s$ has an higher distance from expected value. From muon mean lifetime we calculated Fermi coupling constant; considering the partial data set, our preciser measurement is $G_F/(\hbar c)^3 = (1.16 \pm 0.70) x 10^{-5}\ GeV^{-2}$. This measure agree with expected value.

During data analysis we found an interesting background, really different from the uniform one that we expected: events belonging to this group always decay $\approx 2\mu s$ o $\approx 8\mu s$ after first signal, with an energy around $1200 - 1400\ KeV$. Radioactivity of unstable nucleus on LS's PMT evacuated glass housing could be the source of this background. It's reasonable to think that photons coming from first particle detection on LS excite these nucleus that decay in our temporal window. More studies are needed to confirm this hypothesis and identify the specific nature of the background.

- From a decay sample the electron spectrum was inferred in terms of the total charge collected by the PMT for each decay event, applying some cuts. The study of the spectrum endpoint gives an upper value for the charge, that is converted into energy using a factor evaluated in the previous sections. The difference between such value and the expectation from the Michel spectrum can be interpreted as the mass of a neutrino involved in the muon decay. The final result consists of an upper limit: $m_\nu < (5.99 \pm 0.73)\ MeV/c^2$.